Antal Kerpely Doctoral School of Materials Science and Technology

Synthesis of Metal Oxides Nanoparticles by Precipitation-Calcination Method and their Application for CO_2 Capture from Air

A PhD Dissertation Submitted in Fulfillment of the Requirements for the Degree of Doctor of Philosophy in Material Science and Engineering as a Part of Stipendium Hungaricum Scholarship Programme

By

EI EI KHINE

Master of Science (Physics), Taunggyi University, Myanmar

Supervisors:

Prof. Dr. George Kaptay, Professor

Prof. Dr. Peter Baumli, Professor

Head of the Doctoral School

Prof. Dr. Valéria Mertinger

Institute of Physical Metallurgy, Metal Forming and Nanotechnology
Faculty of Materials and Chemical Engineering
University of Miskolc
Miskolc, Hungary
2022

TABLE OF CONTENTS

TABLE OF CONTENTS i

LIST OF ABBREVIATIONS iii

LIST OF FIGURES iv

LIST OF TABLES ix

1 INTRODUCTION 1

2 LITERATURE REVIEW 3

2.1 The synthesis of the metal oxides nanoparticles 3

2.2 Metal oxides nanoparticles for CO_2 capturing 6

2.3 The synthesis of CaO nanoparticles and the characterizations 7

2.4 Enhancing the properties of CaO by doping different metal oxides 10

2.5 Adsorption of CO_2 by CaO nanoparticles 11

2.6 Scientific Goals 14

3 THEORETICAL CALCULATION OF THE METAL OXIDE SYNTHESIS THROUGH PRECIPITATION-CALCINATION METHOD 15

3.1 Condition 1. Existence and solubility of a stable chloride for a given metal 16

3.2 Condition 2. Spontaneous reaction between metal chloride and NaOH 18

3.3 Condition 3. Fast precipitation of metal hydroxide 21

3.4 Condition 4. Ability of metal hydroxide to convert into metal oxide upon heating 22

3.5 Additional Condition: CO_2 capturing efficiency of the metal oxide produced by precipitation-calcination method 24

4 MATERIALS AND METHODS 27

4.1 Materials 27

4.2 Synthesis of metal oxides nanoparticles by using precipitation-calcination method 27

4.3 Synthesis of metal oxides doped CaO Nanoparticles 29

4.4 The adsorption capacity for pure CaO and metal oxides doped CaO nanoparticles 32

4.5 Characterization techniques 33

5 RESULTS AND DISCUSSION 37

5.1 Synthesis of metal oxides nanoparticles by precipitation - calcination method 37
5.2 Characterization methods of CaO nanoparticles produced by precipitation-calcination method 41
5.3 Characterization of metal oxides doped CaO nanoparticles 45
5.4 Absorption capacity and specific surface areas of pure CaO and metal oxides doped CaO. 61
5.5 Conclusions 76
6 CLAIMS 77
6.1 Theoretical results 77
6.2 Effect of calcination environment (vacuum or air) on CaO nano-particles 78
6.3 Synthesis of metal oxides nanoparticles by calcination in air 80
6.4 Carbonation capacity of metal oxide nanoparticles kept in air 83
FUTURE PERSPECTIVES 88
ACKNOWLEDGEMENT 88
REFERENCES 90
PUBLICATIONS RELATED TO THIS RESEARCH WORK 104

LIST OF ABBREVIATIONS

The symbols are listed according to the order of the letter.

Symbol	Symbol name	Units
K	Kelvin	K
K	Equilibrium constant	-
M	Metal	-
M	Molar mass	g/mol
MCl_x	Metal Chloride	-
p	Partial pressure	Pa
R	Ideal gas constant	-
S	Solubility	mg/L
S_a	Actual solubility	mg/L
S_r	Required solubility	mg/L
T	Temperature	K or °C
T_D	Decomposition temperature	K or °C
T_m	Melting point temperature	K or °C
V	Volume	cm^3
x	Positive integer	-
$\Delta_r G$	Gibbs free energy value of reaction	kJ/mol
$\Delta_r G^0$	The standard Gibbs energy change of reaction	kJ/mol
$\Delta_f G^0$	Standard molar Gibbs energy of formation	kJ/mol
BET	Brunauer, Emmett and Teller (method; specific surface area)	-
BJH	Barrett-Joyner-Halenda (method; Pore Size and Volume Analysis for desorption capacity)	-
EDS	Energy Dispersive Spectroscopy	-
SEM	Scanning Electron Microscope	-
TEM	Transmission Electron Microscope	-
XRD	X-Ray Diffraction	-

LIST OF FIGURES

Figure 2.3-1	The XRD diffractograms of CaO produced by the precipitation-calcination method	8
Figure 2.3-2	(a) TEM and (b) SEM micrographs of CaO powder produced by the precipitation-calcination method	8
Figure 4.2-1	The precursors of metal oxides $Ca(OH)_2$, $Co(OH)_2$ and $Ni(OH)_2$	28
Figure 4.3	The precursor of metal oxides doped to CaO prepared from 0.1:1 and 0.5:1 metal chlorides to $CaCl_2$ (a) $zCo(OH)_2$:$Ca(OH)_2$ to zCoO:CaO (b) $zNi(OH)_2$:$Ca(OH)_2$ to zNiO:CaO (c) $zFe(OH)_3$:$Ca(OH)_2$ to zFe_2O_3:CaO	31
Figure 4.5-1	XRD instrument 2 with chamber to analysis sample during the calcination process under vacuum and in air	33
Figure 4.5-2	Furnaces (a) calcined samples in air (b) low-temperature furnace used as an oven for long period to measure the CO_2 capturing efficiency	34
Figure 4.5-3	SEM and EDS instruments to investigate the morphology and the particles sizes	35
Figure 4.5-4	TEM instrument to investigate the crystallite size	35
Figure 4.5-5	BET instrument to investigate the specific surface areas and pores diameter	36
Figure 5.1-1	XRD diffractogram of CaO from dry precipitate $Ca(OH)_2$ calcined at 650 °C for one hour in air	37
Figure 5.1-2	XRD diffractogram of Co_3O_4 from dry precipitate $Co(OH)_2$ calcined at 170 °C for one hour in air	38
Figure 5.1-3	XRD diffractogram of Fe_2O_3 from dry precipitate $Fe(OH)_3$ calcined at 450 °C for one hour in air	38
Figure 5.1-4	XRD diffractogram of NiO from dry precipitate $Ni(OH)_2$ calcined at 600 °C for one hour in air	38
Figure 5.1-5	TEM micrographs of (a) CaO (b) CoO/Co_3O_4 (c) Fe_2O_3 and (d) NiO	39
Figure 5.1-6	SEM micrographs and EDS spectra of (a) CaO (b) CoO/Co_3O_4 and (c) NiO (d) Fe_2O_3	40
Figure 5.2-1	The XRD diffractograms of sample 1 CaO during its calcination steps under vacuum in the temperature interval of 25 - 650 ºC	42

Figure 5.2-2	The XRD diffractograms of sample 2 CaO during its calcination steps under air in the temperature interval of 25 - 650 ºC	42
Figure 5.2-3	The crystallite sizes of CaO (a) Sample 1 calcination under vacuum (b) Sample 2 calcination in air as function of temperature	43
Figure 5.2-4	TEM micrographs of CaO produced from dry precipitate $Ca(OH)_2$ calcined in air (a) single crystallite (b) agglomerated crystallite (particle)	44
Figure 5.2-5	(a) SEM micrographs and (b) EDS spectra of CaO nanoparticles. The peak for gold in the Figure corresponds to the coating added during sample preparation.	44
Figure 5.3-1	The XRD diffractogram of 0.1CoO:CaO prepared from 0.1:1 mole ratio of $CoCl_2$ to $CaCl_2$ by wet precipitate $Co(OH)_2$:$Ca(OH)_2$ calcined in air between 25-650 ºC measured at each 50 ºC	46
Figure 5.3-2	The XRD diffractogram of 0.1NiO:CaO prepared from 0.1:1 mole ratio of $NiCl_2$ to $CaCl_2$ by wet precipitate $Ni(OH)_2$:$Ca(OH)_2$ calcination in air between 25-650 ºC measured at each 50 ºC	46
Figure 5.3-3	The XRD diffractogram of 0.05Fe_2O_3:CaO prepared from 0.1:1 mole ratio of $FeCl_3$ to $CaCl_2$ by wet precipitate $Fe(OH)_3$:$Ca(OH)_2$ calcination in air between 25-650 ºC measured at each 50 ºC	47
Figure 5.3-4	The crystallite sizes of (a) 0.1CoO:CaO (b) 0.1NiO:CaO and (c) 0.05Fe_2O_3:CaO prepared from 0.1:1 mole ratio of MCl_x to $CaCl_2$ by wet precipitate calcination in air between 25-650 ºC measured at each 50 ºC	48
Figure 5.3-5	SEM micrographs (left) showed the morphology of the agglomerated particles and (right) showed chemical composition of the samples (a) 0.1CoO:CaO (b) 0.1NiO:CaO (c) 0.05Fe_2O_3:CaO	51
Figure 5.3-6	TEM micrographs(left) showing the single crystallite and (right) showing the agglomerated crystallite (particle) of the samples (a) 0.1CoO:CaO (b) 0.1NiO:CaO (c) 0.05Fe_2O_3:CaO	52
Figure 5.3-7	The XRD diffractogram of 0.5CoO:CaO prepared from 0.5:1 mole ratio of $CoCl_2$ to $CaCl_2$ by wet precipitate $Co(OH)_2$:$Ca(OH)_2$ calcination in air between 25-650 ºC measured at each 50 ºC	53

Figure 5.3-8	The XRD diffractogram of 0.5NiO:CaO prepared from 0.5:1 mole ratio $NiCl_2$ to $CaCl_2$ by wet precipitate $Ni(OH)_2$:$Ca(OH)_2$ calcination in air between 25-650 ºC measured at each 50 ºC	54
Figure 5.3-9	The XRD diffractogram of 0.25Fe_2O_3:CaO prepared from 0.5:1 mole ratio of $FeCl_3$ to $CaCl_2$ by wet precipitate $Fe(OH)_3$:$Ca(OH)_2$ calcination in air between 25 - 650 ºC measured at each 50 ºC	55
Figure 5.3-10	The crystallite sizes of (a) 0.5CoO:CaO (b) 0.5NiO:CaO and (c) 0.25Fe_2O_3:CaO prepared from 0.5:1 mole ratio of MCl_x to $CaCl_2$ by wet precipitate calcined calcination in air between 25-650 ºC measured at each 50 ºC	56
Figure 5.3-11	SEM micrographs (left) showed the morphology of the agglomerated particles and (right) showed chemical composition of the samples (a) 0.5CoO:CaO (b) 0.5NiO:CaO (c) 0.25Fe_2O_3:CaO	59
Figure 5.3-12	TEM micrographs(left) showing the single crystallite and (right) showing the agglomerated crystallite (particle) of the samples (a) 0.5CoO:CaO (b) 0.5NiO:CaO (c) 0.25Fe_2O_3:CaO	60
Figure 5.4-1	The time dependence of the relative mass change of pure CaO samples exposed to air at different temperatures	61
Figure 5.4-2	The XRD diffractograms of pure CaO, fresh sample and after the measurements of the sample exposed to air at different temperatures	62
Figure 5.4-3	The time dependence of the relative mass change of 0.1CoO:CaO samples exposed to air at different temperatures	63
Figure 5.4-4	The XRD diffractogram of 0.1CoO:CaO, fresh sample and after the measurements of the sample exposed to air at different temperatures	63
Figure 5.4-5	The time dependence of the relative mass change of 0.1NiO:CaO samples exposed to air at different temperatures	64
Figure 5.4-6	The XRD diffractogram of 0.1NiO:CaO fresh sample and after the measurements of the sample exposed to air at different temperatures	64
Figure 5.4-7	The time dependence of the relative mass change of 0.05Fe_2O_3:CaO samples exposed to air at different temperatures	65
Figure 5.4-8	The XRD diffractogram of 0.05Fe_2O_3:CaO, fresh sample and after the measurements of the sample exposed to air at different temperatures	66

Figure 5.4-9	The time dependence of the relative mass change of 0.5CoO:CaO samples exposed to air at different temperatures	68
Figure 5.4-10	The XRD diffractogram of 0.5CoO:CaO, fresh sample and after the measurements of the sample exposed to air at different temperatures	69
Figure 5.4-11	The time dependence of the relative mass change of 0.5NiO:CaO samples exposed to air at different temperatures	70
Figure 5.4-12	The XRD diffractogram of 0.5NiO:CaO, fresh sample and after the measurements of the sample exposed to air at different temperatures	70
Figure 5.4-13	The time dependence of the relative mass change of 0.25Fe_2O_3:CaO samples exposed to air at different temperatures	71
Figure 5.4-14	The XRD diffractogram of 0.25Fe_2O_3:CaO, fresh sample and after the measurements of the sample exposed to air at different temperatures	71
Figure 5.4-15	The maximum capturing capacity % of pure CaO and 0.1CoO:CaO, 0.1NiO:CaO and 0.05Fe_2O_3:CaO at different measured temperatures	75
Figure 5.4-16	The maximum capturing capacity (%) of pure CaO and 0.5CoO:CaO, 0.5NiO:CaO and 0.25Fe_2O_3:CaO at different measured temperatures	75
Figure C1	XRD diffractograms of CaO during its calcination steps in the temperature range of 25 - 650 ºC(a) calcination under vacuum (b) calcination in air	79
Figure C2	The crystallite sizes of CaO as a function of temperatures in the range of 50 - 650 °C (a) calcination under vacuum (b) calcination in air	80
Figure C3	The XRD diffractograms and TEM micrographs of the pure metal oxides (a) Co_3O_4 (b) Fe_2O_3 (c) NiO	81
Figure C4	The crystallite sizes of low-doped CaO as a function of temperatures in the range of 50 - 650 °C (a) 0.1NiO:CaO (b) 0.1CoO:CaO (c) 0.05Fe_2O_3:CaO	82
Figure C5	The crystallite sizes of low-doped CaO as a function of temperatures in the range of 50 - 650 °C (a) 0.5NiO:CaO (b) 0.5CoO:CaO (c) 0.25Fe_2O_3:CaO	83
Figure C6	The time dependence of the relative mass change of pure CaO samples exposed to air at different temperatures	84

Figure C7 The XRD diffractograms of pure CaO, fresh sample and after the measurements of the sample exposed to air at different temperatures 84

Figure C8 The The XRD diffractograms of low-doped CaO fresh sample and after the measurements of the samples exposed to air at different temperatures (a) 0.1CoO:CaO (b) 0.1NiO:CaO and (c) 0.05Fe_2O_3:CaO 86

Figure C9 The XRD diffractograms of low-doped CaO fresh sample and after the measurements of the samples exposed to air at different temperatures (a) 0.5CoO:CaO (b) 0.5NiO:CaO and (c) 0.25Fe_2O_3:CaO 87

LIST OF TABLES

Table 2.1	Synthesis methods of metal oxide nanoparticles from different metal chloride and NaOH	5
Table 2.2	The characterizations and syntheses of CaO nanoparticles using different precursor	9
Table 3.1.1	Metals chlorides with high enough solubilities obey condition I	17
Table 3.1.2	Metals chlorides with not sufficient solubilities which do not obey condition I	18
Table 3.2.1	$\Delta_r G$ (kJ/mol) for the required and the actual value of the reactions at T = 300K from reactions 3.2-5, which obey condition 2 (passed condition 1 from Table 3.1.1)	20
Table 3.2.2	$\Delta_r G$ kJ/mol for the required and the actual value of the reactions at T = 300K from reactions 3.2.3, which do not obey condition 2 (passed condition 1 from Table 3.1.1)	20
Table 3.3.1	The metal hydroxides that have low enough solubility in water at T = 300K which obey condition 3 (passed condition 2 from Table 3.2.1)	22
Table 3.3.2	The metal hydroxides that have low enough solubility in water at T = 300K which do not obey condition 3 (passed condition 2 from Table 3.2.1)	22
Table 3.4.1	Ability of metal hydroxide to convert into metal oxide upon heating which obey condition 4 (passed condition 3 from Table 3.3.1)	24
Table 3.4.2	Ability of metal hydroxide to convert into metal oxide upon heating which do not obey condition 4 (passed condition 3 from Table 3.3.1)	24
Table 3.5.1	CO_2 capturing efficiency of the metal oxide at T= 300K which obey additional condition (passed condition 4 from Table 3.4.1)	26
Table 3.5.2	CO_2 capturing efficiency of the metal oxide at T= 300K which do not obey additional condition (passed condition 4 from Table 3.4.1)	26
Table 4.2.1	The molarity and volume of the reactants using in the synthesis	28
Table 4.2.2	The list of the samples upon the calcination temperatures and environments during the calcination process	29
Table 4.3	Compositions, concentrations, and volume of the solution prepared at 1300rpm stirring speeds to produce CoO doped CaO, NiO doped CaO and Fe_2O_3 doped CaO	29

Table 4.4	The samples kept at different temperatures for the absorption process	32
Table 5.2.1	Phases formed from wet precipitate $Ca(OH)_2$ during its calcination at different temperatures to CaO	43
Table 5.2.2	The specific surface area of CaO sample calcined in air at 650 ºC for 1 hour	45
Table 5.3.1	Phases formed from wet precipitate $Co(OH)_2$:$Ca(OH)_2$ during its calcination at different temperatures to to 0.1CoO:CaO	48
Table 5.3.2	Phases formed from wet precipitate $Ni(OH)_2$:$Ca(OH)_2$ during its calcination at different temperatures to to 0.1NiO:CaO	49
Table 5.3.3	Phases formed from wet precipitate $Fe(OH)_3$:$Ca(OH)_2$ during its calcination at different temperatures to 0.05Fe_2O_3:CaO	49
Table 5.3.4	The volume percentages of the different phases (%) found by XRD in the 0.1CoO:CaO sample prepared by heating in air as a function of temperature from Figure 5.3-1	49
Table 5.3.5	The volume percentages of the different phases (%) found by XRD in the 0.1NiO:CaO sample prepared by heating in air as a function of temperature from Figure 5.3-2	50
Table 5.3.6	The volume percentages of the different phases (%) found by XRD in the 0.05Fe_2O_3:CaO sample prepared by heating in air as a function of temperature from Figure 5.3-3	50
Table 5.3.7	Phases formed from wet precipitate $Co(OH)_2$:$Ca(OH)_2$ during its calcination at different temperatures to 0.5CoO:CaO	57
Table 5.3.8	Phases formed from wet precipitate $Ni(OH)_2$:$Ca(OH)_2$ during its calcination at different temperatures to 0.5NiO:CaO	57
Table 5.3.9	Phases formed from wet precipitate $Fe(OH)_3$:$Ca(OH)_2$ during its calcination at different temperatures to 0.25Fe_2O_3:CaO	57
Table 5.3.10	The volume percentages of the different phases (%) found by XRD in the 0.5CoO:CaO sample prepared by heating in air as a function of temperature from Figure 5.3-7	58
Table 5.3.11	The volume percentages of the different phases (%) found by XRD in the 0.5NiO:CaO sample prepared by heating in air as a function of temperature from Figure 5.3-8	58

Table 5.4.1	The average value of maximum mass ratio of saturated mass and initial mass for pure CaO samples	62
Table 5.4.2	The average value of maximum mass ratio of saturated mass and initial mass for 0.1CoO:CaO samples	63
Table 5.4.3	The average value of maximum mass ratio of saturated mass and initial mass for 0.1NiO:CaO samples	65
Table 5.4.4	The average value of maximum mass ratio of saturated mass and initial mass for $0.05Fe_2O_3$:CaO samples	66
Table 5.4.5	The specific surface area of pure CaO and low doped CaO, fresh samples and after capturing for 3-6 weeks at room temperature	67
Table 5.4.6	The average value of maximum mass ratio of saturated mass and initial mass of 0.5CoO:CaO samples	69
Table 5.4.7	The average value of maximum mass ratio of saturated mass and initial mass of 0.5NiO:CaO samples	70
Table 5.4.8	The average value of maximum mass ratio of saturated mass and initial mass of $0.25Fe_2O_3$:CaO samples	72
Table 5.4.9	The specific surface area of highly low doped CaO, fresh samples and after capturing for 3-6 weeks at room temperature	72
Table 5.4.10	The maximum mass ratio in percentage of each sample as a function of different temperatures	74

1. Introduction

Nanoparticles (NPs) are a group of materials made up of small particles that should have at least one dimension less than 100 nm. These materials became exceedingly important since their properties are highly influenced by their size that leading to various potential applications. Many research works have been reported regarding the applications of different metal oxide nanoparticles. Al_2O_3 nanoparticles have been suggested to enhance the mechanical properties of cement[1]. Fe_3O_4, TiO_2, CuO, and ZnO were reported as potential candidates for antibacterial agents [2]. Metal oxide nanoparticles can be used as antimicrobial agents, prospective drug delivery agents and in various other biomedical applications.

The metal oxide nanoparticles can be produced by using various methods such as sol-gel [3–5], thermal decomposition [6–8], hydrothermal technique, combustion method, co-precipitation technique [9], [10], biogenic method, precipitation method, two-step thermal decomposition technique, one step multi-component synthesis [11], microwave synthesis [12] and sonication method [13]. The metal oxide nanoparticles can be used to capture CO_2 [14].

Carbon dioxide CO_2 is a crucial player in the greenhouse effect. CO_2 emission is mostly attributed to the burning of fossil fuels, notably from coal power plants and industrial operations. The growing quantity of CO_2 in the atmosphere negatively affects the environment, especially in the form of climate change and global warming. One possible solution is to use CO_2 capture and storage (CCS) technology. The capturing of CO_2 by using CaO-based adsorbents has attracted industrial sectors due to the great theoretical capacity of CO_2 capturing, cheap cost, and promising applications on a massive scale.

In synthesizing CaO nanoparticles, several variables synthesis should be addressed to increase the sintering-resistant capabilities of CaO-based adsorbents, such as decreasing the particle size, increasing the surface area and distributing CaO over an inert substrate, in addition to surface modification [15].

Calcium oxide CaO is an important inorganic substance utilized in a range of different applications attracting interest in the area of materials research. It has been utilized as a catalyst [16–18], pellet for CO_2 capture and kinetic analysis [19-20], toxic-waste remediation agent, or as an additive in refractory and paint industries [21]. CaO nanoparticles can be used as an antimicrobial agent, a potential drug delivery agent, as well as in various other biomedical applications. Due to its possibility to modify electrical and optical (dielectric) properties, CaO

was utilized as a constituent of composite or doped material in thin-film manufacturing. CaO has been interested as a CO_2 absorber, owing to its excellent kinetics and substantial capturing efficiency, even at weak CO_2 concentration environment [22–28]. But CaO is unstable and will eventually interact with CO_2 to change back to $CaCO_3$ when cooled back to ambient temperature [29].

Hence, this study aims to optimize sustainable sorbent efficiency in long-term capturing applications. Several techniques can be utilized to prepare CaO nanoparticles. The chemical and physical characteristics of CaO can be modified to the nano level. Morphology, surface area and capturing efficiency can be carefully managed under precise synthesis environments, different parameters and favorably influence the sorbents' reactivity [21, 28–31].

2. Literature Review

2.1 The synthesis of metal oxide nanoparticles

Metal oxide nanoparticles have been produced from different reagents by different synthesis techniques, including precipitation, combustion, sol-gel, wet chemical, microwave, mechanochemical, and hydrolysis. As the following; Al_2O_3 nanoparticles were synthesized using the precipitation technique from various reagents, including aluminum isopropoxide, $Al(NO_3)_3 \cdot 9H_2O$ and $AlCl_3 \cdot 6H_2O$, as well as additional reactants, such as HCl, deionized water, ethyl alcohol, ammonium hydroxide, and ethanol [32]. Furthermore, a solvent-free hydrothermal-assisted calcination procedure using $Al(OH)_3$ was used to produce Al_2O_3 nanoparticles [33].

BeO nanopowder was produced using sol-gel, co-precipitation, and hydrothermal from beryllium sulfate tetrahydrate and ammonium hydroxide [34-35]. Moreover, BeO nanofluid was synthesized by polyacrylamide gel route from beryllium sulfate tetrahydrate [36]. Besides, BeO was produced by using heat-treating method from the beryllium hydroxide at the calcination temperature of 350-400 °C [37-38].

CaO has been produced by using different synthesis methods such as co-precipitation, precipitation, thermal decomposition, sol-gel [39-41] and microwave synthesis. CaO could be produced using different reagents such as $CaCO_3$, $Ca(NO_3)_2$, $CaCl_2$, and NaOH. While, CdO has been produced by co-precipitation [42–44], photochemical synthesis [45] and soft chemical method [46] using cadmium acetate dihydrate $Cd(COOCH)_3$ and NaOH. Furthermore, CdO has prepared via green chemistry process [47] and hydrothermal synthesis [48] using $Cd(NO_3)_3 \cdot 4H_2O$.

CoO nanoparticles have been produced only at very high temperatures and transformed to Co_3O_4 when it is cooled down in air. CoO nanoparticles are stable only in the unoxidized environment [49]. Co_3O_4 has been produced through different routes such as green synthesis [50], liquid phase synthesis, precipitation, co-precipitation, electrospinning, an impregnation-reduction, surfactant-assisted self-assembly, wet chemical, template-assisted, cotton template route, sol-gel, hydrothermal or solvothermal, nonchemical and chemical bath deposition method [51]. In the synthesis of cobalt oxides, different cobalt salts have been used as the reactants, such as cobalt nitrate, cobalt sulfate, cobalt chloride and cobalt acetate [52-53]. CuO nanowires, nanorods, and nano pellets have been mostly produced from copper chloride and

NaOH by using poly templating [54], wet chemical [55], hydrothermal [56] and sol-gel methods [57-58].

Fe_2O_3 nanoplate and nanosheet have been produced by using spray pyrolysis technique [59], photo-assisted electrocatalytic methanol [60], two-step hydrothermal synthesis [61] and microwave hydrothermal synthesis [62]. Moreover, co-precipitation method, sonolysis synthesis using $FeCl_3$ and NaOH, gas decomposition, sol-gel, bulk solution, and microemulsion are also mentioned as the synthesis methods of iron oxide nanoparticles [63]. Fe_2O_3 nanoparticles have been produced through the precipitation method from ferric sulfate precursor and ammonium hydroxide [64].

MgO has been produced by using different routes such as green synthesis [65-66], precipitation method from $MgCl_2$ and NaOH [67], sol-gel, co-precipitation from $Mg(NO_3)_2$ and ammonia solution [68–71] and solvent mixed spray pyrolysis technique [72]. MnO nanoparticles with different shapes, such as nanocrystals, nanofibers, nanosheets, nanoclusters, nanocubes and nanoflake have been produced by using different routes, such as thermal decomposition from $Mn(HCOO)_2$, $Mn(C_6H_5N_2O_2)_2$, $MnCl_2$ [73-74] and sol-gel method [75]. NiO nanosheets have been produced from $NiCl_2$ and NaOH using thermal decomposition [76], biosynthesis [77-78] and microemulsion method [79]. Furthermore, co-precipitation [80], dehydration- decomposition [81], solid-state decomposition [82], microwave [83], isothermal decomposition [84], ion diffusion [85], sonochemical method [86] and precipitation method from $NiCl_2$ and urea [87] were also used. SnO nanosheets has been produced by using isothermal synthesis [88], two step-chemical method from $SnCl_2$ and deionized water [89], microwave-assisted-hydrothermal synthesis [90-92] and hydrothermal synthesis [93] from $SnCl_2$ and ammonium hydroxide.

ZnO nanoparticles have been produced by using different routes such as hydrothermal process from $Zn(NO_3)_2$ [94], sol-gel method, solvothermal method, microwave-assisted method, precipitation method, ultrasonic method, biological method, green synthesis method [95]. ZnO has been produced from different precursors such as $Zn(CH_3CO_2)_2 \cdot 2H_2O$, $ZnCl_2$ and $Zn(NO_3)_2$ with different reactants ethanol, oxalic acid, methanol, acetone, NaOH, and butyl alcohol.

Table 2.1 shows metal oxides which produced using precipitation techniques from metal chloride and NaOH reagents. Furthermore, metal oxides have been produced by using different routes employing metal chloride and NaOH.

Table 2.1: Synthesis methods of metal oxide nanoparticles from different metal chloride and NaOH

Composition of products	Reagents		Synthesis method	Calcination temperature °C	Crystallite size (nm)	Size of nano-particle nm	Ref
Al_2O_3	$AlCl_3$	HCl/ Ammonia (NH_3)/ Ethanol (C_2H_5OH) /PVP	precipitation	550-1100	30-100 10-26		[96-98]
BeO	$Be(SO)_4$	NH_4OH	Co-precipitation	800-1200	20-66		[99]
CaO	$CaCl_2$	NaOH	precipitation	600	48	150-200	[100]
CaO	$CaCl_2$	NaOH	Co-precipitation	450	11		[101]
CdO	$Cd(COOCH_3)_2$	NaOH	precipitation	500	21-33		[102]
CdO	$CdCl_2$	NaOH	microemulsion	720	40	200	[103]
CdO	$CdCl_2$	NaOH	sol-gel		11-24	70	[104]
CoO	$CoCl_2$	NaOH	precipitation	600-800	50	224	[105]
CoO	$CoCl_2$	Na_2CO_3	Co-precipitation	500	100-200		[50]
CoO	$CoCl_2$	NaOH	Green Synthesis	600		650	[106]
CuO	$CuCl_2$	NaOH	precipitation	500		≈ 200	[56]
CuO	$CuCl_2$	NaOH	hydrothermal	105-150	25-66	-	[58]
CuO	$CuCl_2$	NaOH	sol-gel		20	50	[107]
Fe_2O_3	$FeCl_3$	NaOH	Co-precipitation		10	90-140	[108]
Fe_2O_3	$FeCl_3$	NaOH	Sonochemical	500	19	12-24	[109]
NiO	$NiCl_2$	NaOH	Hydrothermal	300-600		25-120	[110-111]
MgO	$MgCl_2$	NaOH	Spinning Disk Reactor	450-600	30-70	150	[68]
SnO_2	$SnCl_2$	NaOH	Hydrothermal solution method	< 300 = SnO not stable, > 400-700			[112]
ZnO	$ZnCl_2$	NaOH	precipitation		16-22	300-500	[113]
ZnO	$Zn(NO_3)_2$	NaOH	precipitation	50-70	25-34		[114]

Knowledge gap: There is no study describing the possible candidates of metal oxide nanoparticles can be synthesized through the precipitation-calcination method from metal chloride and NaOH.

As a theoretical approach, the possibility of producing metal oxides will be calculated through precipitation-calcination method in this research.

2.2 Metal oxides nanoparticles for CO_2 capturing

CO_2 capture and storage (CCS) technology is the common techniques to reduce CO_2 emissions [115]. Moreover, there are a few novel methods in development that are focused on the periodic capturing of CO_2 using calcium-based sorbents and might possibly lower the expense of CO_2 absorption significantly [116], and new zero-emission power generation concepts using calcium-based sorbents as CO_2 capture materials (CCM), such as American zero emission coal alliance (ZECA) process [117] and the Japanese hydrogen production by reaction integrated novel gasification process [118]. Preliminary analysis showed that all of these systems were economically attractive, particularly new zero-emission power generation systems that can potentially achieve a power plant efficiency up to 70% even after CO_2 capture [119]. Therefore, the development of calcium-based sorbents for these processes is technically and financially interesting.

FeO, Fe_2O_3 and Fe_3O_4 iron oxides have been investigated for CO_2 capturing process [120]. K_2O transformed to K_2CO_3 in water and CO_2 environment [121]. Regarding the thermodynamic data at 300 K, the Gibbs free energy value of carbonation for BeO is 1.665 kJ/mol. Therefore, it transforms into complex BeO instead of $BeCO_3$. However, BeO nanotube has been used for CO_2 absorption [122-123]. Li_2O transformed to Li_2CO_3 under CO_2 environment at low temperatures; this decarbonation process works at 600 °C [124-125]. MgO particles has been produced for carbonation at room temperature to 316 °C and decarbonation process at 320-460 °C [126]. Na_2O has better CO_2 absorption ability than Li_2O and K_2O for carbon capturing [127]. The Gibbs free energy value of some reaction at 300 K have been described [128-129].

$MgO + CO_2 = MgCO_3$ is -48.206 kJ/mol

$CaO + CO_2 = CaCO_3$ is -130.127 kJ/mol

$SrO + CO_2 = SrCO_3$ is -188.805 kJ/mol

$BaO + CO_2 = BaCO_3$ is -220.394 kJ/mol

$Na_2O + CO_2 = Na_2CO_3$ is -231.9 kJ/mol

and $K_2O + CO_2 = K_2CO_3$ is -309.5 kJ/mol

Among those metal oxides (M = Mg, Ca, K, Na), MgO has less CO_2 absorption capacity compared to CaO, K_2O and Na_2O. CaO and MgO metal oxides have the capability of carbonation- decarbonation process in several cycles. The carbonation process of MgO was done at 25-100 °C [130-131]. NiO particles have the capability for carbonation- decarbonation

process when it is done at low temperatures [132]. ZnO particles have the capability for carbonation- decarbonation process when the carbonation process is done at a temperature range of 25-100 °C in air, under flowing CO_2 gas. Moreover, decarbonation process of ZnO was done at 250-300 °C [133-134].

Knowledge gap: The missing information is the potential applications of metal oxide nanoparticles for CO_2 capturing.

2.3 The synthesis of CaO nanoparticles and the characterizations

Pure CaO is an oxide that has a cubic lattice structure with anisotropic catalytic properties and is often investigated as a component in catalytic powder materials or cement [135]. CaO can also be used as a component of composite or doped material, while the application fields become extended by thin film technology due to the possibility of modifying electrical and optical (dielectric) properties. CaO nanoparticle is commonly prepared via bio-directed synthesis of calcium oxide from limestone using honey and by a two-step thermal decomposition method under ambient temperature.

CaO is also known as a dopant able to stabilize cubic zirconia [136] or hafnia [137] and modify the refractive index of silicate glasses [138]. Due to its wide band gap (7.1 eV) [170], high dielectric constant and ability to form solid solutions and ternary crystalline phases. CaO and its ternary alloys can be considered as interesting dielectric gate materials, exhibiting high mechanical and radiation resistance.

Few research groups have reported the synthesis routes of CaO nanoparticles by thermal decomposition, combustion method, sol-gel, hydrothermal technique, co-precipitation technique, biogenic method, two-step thermal decomposition technique, and microwave synthesis. Generally, CaO nanoparticles are often produced via the thermal treatment of $Ca(OH)_2$ [139]. $Ca(OH)_2$ normally decomposes at about 500 °C under atmospheric pressure. The grain size of CaO grew faster as the calcination temperature and heating time increased [140].

CaO nanoparticles are produced by the decomposition of $CaCO_3$ at a high temperature greater than 900 °C [141] or by precipitation method using different reagents [142]. Calcium oxide (CaO) nanoparticles were synthesized by sol-gel method [30]. The findings demonstrate that spherical calcium oxide nanoparticles were produced with particle sizes 30–40 nm utilizing the thermal-decomposition technique [143].

Two researchers [99-100] recently produced CaO nanoparticles by using $CaCl_2$ and NaOH reagents through precipitation- calcination process. The calcination process was done in the N_2 environment. Figure 2.3-1 shows the XRD pattern of the produced CaO. Regarding XRD pattern, $CaCO_3$ and $Ca(OH)_2$ have been detected in the produced CaO samples. Moreover, TEM micrograph of CaO sample showed the morphology and the crystallite size are on a micro-scale. SEM micrograph of CaO showed the morphology of the agglomerated crystallite or particles on a micro-scale.

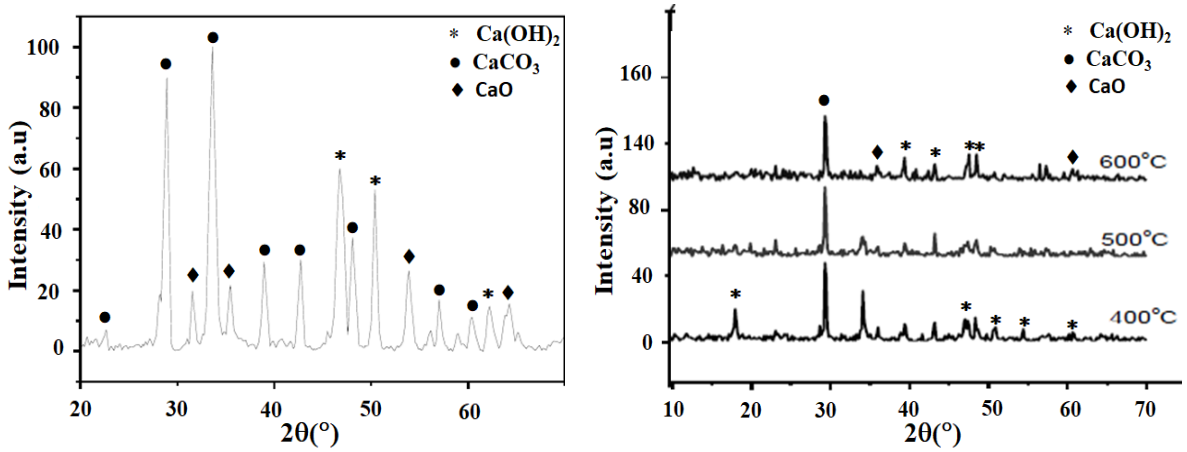

(a) (b)

Figure 2.3-1. The XRD diffractograms of CaO produced by the precipitation-calcination method [99-100]

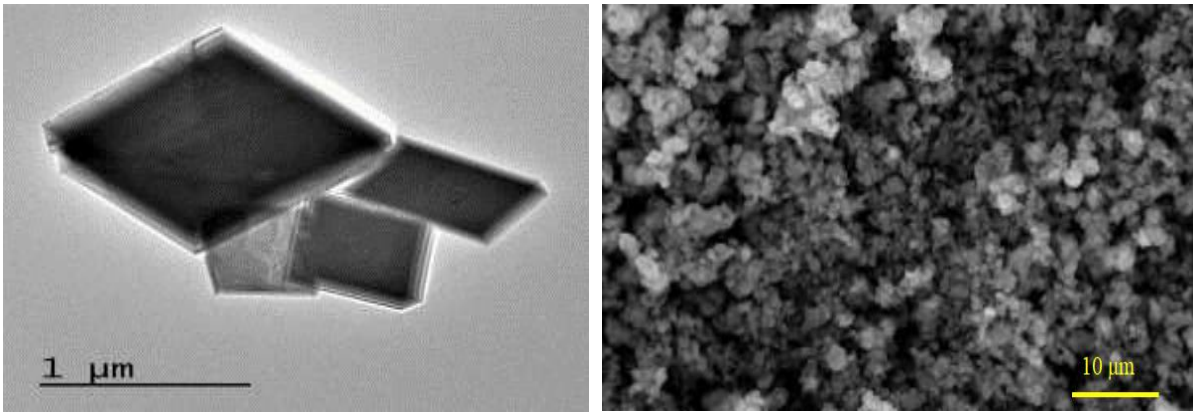

(a) (b)

Figure 2.3-2. (a) TEM and (b) SEM micrographs of CaO powder produced by the precipitation-calcination method [99]

Varying the synthesis techniques, all physical and chemical features of nano-CaO could be modified. Shape, surface area and capture efficiency can be precisely regulated under particular synthesis conditions [29]. The calcination temperatures of CaO from $Ca(OH)_2$

precursor are between 450- 650 °C [144–147]. The grain size of CaO increases rapidly when the calcination temperature and heating duration are increased. To increase the sintering-resistant capabilities of CaO-based adsorbents, several variables should be addressed, such as reducing the particle size, increasing the surface area, distributing CaO over an inert substrate, as well as surface modification [148].

Generally, CaO nanoparticles have been produced via thermal treatment of $Ca(OH)_2$ followed by calcination under N_2 atmosphere at 650 °C for 1 hr, decomposition of $CaCO_3$ at a high temperature greater than 900 °C and precipitation method using different reagents. The characterizations of CaO nanoparticles through different synthesis and different precursors are shown in Table 2.2.

Table 2.2: The characterizations and syntheses of CaO nanoparticles using different precursor

Synthesis Method	Precursor	Characterization					Ref
		XRD size nm	SEM Particle size nm	TEM nm	BET Specific surface area m^2/g	TG Calcination temperature ^oC	
Co-precipitation	$Ca(NO_3)_2 \cdot 6H_2O$	15	<100		-	-	[142]
Thermal-decomposition	$Ca(NO_3)_2$	14	-	14	-	700	[9]
Microwave-assisted	$Ca(NO_3)_2 \cdot 4H_2O$	24	32		74.46	-	[12]
Sonication-assisted	$Ca(NO_3)_2 \cdot 4H_2O$	139	-	95	-	700	[13]
Ultrasonic-assisted	$C_4H_6CaO_4$	98.6	65-80		8.89	-	[149]
Thermal decomposition	$CaCl_2 \cdot 2H_2O$	40	-	90	13.86	650	[150]
Green-synthesis	Eggshells, $Ca(NO_3)_2$	23-40	86-117	-	8.0142	867	[151]
A facile carbon template	$C_{12}H_{24}CaO_{15}$	14.75	94.4	-	-	700	[152]
Solution combustion	$Ca(NO_3)_2 \cdot 4H_2O$	39.03	-	-	-	700	[25]
Bio-Directed Synthesis	$CaCO_3$	16-28	50	-	-	-	[21]
Sol-Gel	Eggshells	24.51	300	-	-	700	[41]

Knowledge gap: The missing information is the possibility of producing CaO nanoparticles by calcination in air. Moreover, to produce 100 % pure CaO and small particle size (below 100 nm) could be considered.

2.4 Enhancing the properties of CaO by doping using different metal oxides

Doping CaO nanoparticles with various atoms is recognized as an essential way to boost the capturing effectiveness and the stability of the sorbent materials [153]. Several research studies have been done that exhibit superior characteristics of metal-doped CaO nanoparticles. ZrO_2 doped to CaO was conducted to increase the sorption of CO_2 [154]. The stability of Zr-doped CaO sorbents is tested for CO_2 capturing that extended operation cycles with different molar ratios. Zr-doped CaO nanoparticles act as a barrier against heating in high temperatures and preventing CaO grain growth [155–157]. Potassium ion-doped calcium oxide nanoparticles can be used as a solid catalyst for the transesterification of a variety of triglycerides [158]. A series of metal dopants (M = Cr, Mn, Si, Cu, Ti, Co, Zr, and Ce) for CaO have been characterized for their efficiency in CO_2 adsorption capacity and stability [159-160]. Moreover, Ni ion-doped CaO nanorods were produced through wet chemical method, which have better catalyst activity [161]. CaO-based sorbents doped with different amounts of CeO_2 were synthesized through sol-gel method, producing special morphology and small crystallite size of CaO; thus, the sorbent exhibited outstanding stability. The doping of CeO_2 also improved the sorbent's carbonation rate, resulting in a high capacity in a short period of time [162]. Iron is an effective dopant to increase the capacity of calcium chloride [163] and calcium compounds [164–166].

Iron (III) oxide decomposed from $Fe(OH)_3$. Fe_2O_3 has been prepared from different precursors using thermal decomposition method and precipitation method at low temperatures [167]. Iron (III) oxide and cobalt doped to CaO are used for the preparation of composite materials [168 –170]. Fe ion-doped CaO was investigated at low-temperature conditions below 700 ℃ as a catalyst to absorb CO_2. Iron is an excellent element to improve both the catalytic activity and the carbon deposition in catalytic examinations. The reaction of Fe_2O_3 and CaO has enhanced the properties of CaO [171]. Iron oxide has been prepared using the precipitation method from iron salt at 650 ℃ [172], co-precipitation, electrochemical, and many other methods [173]. Fe_2O_3 can be used as a dopant to metal oxides. Fe_2O_3 doped CeO_2 nanoparticles were studied for the purification of manganese ions from the aqueous media through the chemical precipitation method [174] and Cr(II) removal from the waste water. Fe_2O_3 can be used as an electrode material for electrochemical supercapacitors, sensors, catalysts, and energy-related applications, absorbents for wastewater treatment. The application of Fe_2O_3 was used as an oxygen carrier and CH_4 as a reduction gas in CLC system as a solid lopping material. Moreover, nickel oxide and cobalt oxide are also useful as looping material in the chemical

looping combustions CLC techniques [175]. Fe_2O_3 was produced from $FeCl_3.6H_2O$ and NaOH solution. NiO and CoO used for the carbon adsorbent NiO:CaO catalyst was prepared using metal nitrate through a wet impregnation method that has been used for the synthesis of ceramic materials [176]. $NiCl_2$ was applied as a reactant with NaOH to formed $Ni(OH)_2$ [177].

CaO by doping of Na_2CO_3 has been investigated for more efficient sorption. Moreover, the crystallite size is smaller than pure CaO [178]. CaO-based sorbents doped with varying quantities of CeO_2 were produced by a sol-gel process which formed unique morphology and CaO minute crystallite size. Therefore, the sorbent demonstrated exceptional stability. The doping of CeO_2 also increased the carbonation rate of the sorbent, resulting in a high capacity in a short amount of time.

Iron (II) oxide, iron (III) oxide, nickel (II) oxide and cobalt (II) oxide are the most suitable metals which can be used for doping to CaO. Those metal oxides have more positive Gibb's free energy than calcium oxide, which may increase the stabilization of CaO. The doping of different elements that rely on Gibb's free energy to CaO can be controlled by the capacity of the carbonation.

Knowledge gap: There is no study to describe the characterizations of the metal oxides doped CaO nanoparticles through precipitation-calcination method.

2.5 Absorption of CO_2 by CaO nanoparticles

The use of calcium-based sorbents for CO_2 absorption was primarily done through capture/regeneration loops of CaO utilizing the following reaction:

$$CaO + CO_2 \Leftrightarrow CaCO_3$$

The capturing operation is a chemical process. Generally, at 650 °C under ambient pressure of CO_2. As a result, CaO and $CaCO_3$ are formed in the process. The carbonated sorbent is then exposed to the regenerator for decarbonation, an operation that normally happens at 900 °C under ambient pressure. The decarbonation of $CaCO_3$ is performed utilizing external heating or internal heating from power stations. Several researchers have examined the utilization of CaO from naturally occurring materials, such as limestone and dolomite. Nevertheless, such sorbents support the issue of loss-in-capacity, i.e., the capacity of CO_2 absorption drop significantly after a few rounds of reaction/ regeneration [179].

The phenomenon has been largely related to the heat treatment of the CaO and $CaCO_3$ during the regeneration phase. The regeneration temperature is as high as 900 °C and

substantial sintering of $CaCO_3$ particles takes place, which promotes agglomeration of crystals and exchanges the surface area and pore volume. The speed of the gas-solid reaction consequently deteriorates dramatically with increasing rounds of reaction/regeneration. The transformation generally decreases to a residual after extended rounds of reaction/regeneration [180]. The loss-in-capacity issue must be overcome before the use of calcium-based sorbents become common.

Six strategies have been offered to address this challenge in the literature, involving: (i) developing better calcium precursors to create CaO sorbent, (ii) employing various calcium-based natural occurring materials like dolomite and hematite [181] or alternative calcium sources like shell [182], (iii) producing a customized CO_2 sorbent like CaO from precipitated $CaCO_3$ (PCC) [183], (iv) optimizing the porosity of CaO by hydration process [184]; (v) altering CaO-based sorbents [185] and (vi) generating novel CaO based sorbents at elevated temperature [186–188].

Undoubtedly, calcium precursors are particularly significant in the manufacture of calcium-based sorbents. The features of CaO sorbent, which decomposed from nanosized $CaCO_3$ (40 nm) possess CO_2 capturing capabilities with a high residue and carbonations at 650 °C. The variations in the absorption capacity for numerous CaO dissociated from calcium nitrate tetrahydrate, calcium hydroxide, calcium carbonate, and calcium acetate monohydrate. They demonstrated that CaO degraded from the organometallic precursors such as calcium acetate monohydrate. That has better to apply than other calcium precursors in CO_2 absorption.

CaO was prepared from $CaCO_3$ with the decomposition temperature above 900 °C. The development of CaO-based adsorbents decreases over several cycles of CaO carbonation/calcination [189-191]. CaO rapidly degrades due to the application of the sorbent. The CO_2 capturing of CaO sorbent was done at high temperatures between 550-800 °C. The CaO nanoparticles have comparatively high absorption efficiency and capabilities of multiple carbonations and decarbonation cycles.

The use of CaO nanoparticles as CO_2 absorbance has excessively reduced the sorption capacity and renderability of the pure sorbent. The reduction in CaO reactivity (and hence the level of transformation) has been ascribed mostly to heat treatment of the CaO particle throughout the carbonation cycle. The reducing of the surface energy of the grains induced by reducing their surface area or increasing their particle size that is the driving factor for sintering. Reduced surface area leads to a decrease in the number of active sites accessible for the

carbonation process [192], the development of a $CaCO_3$ deposit on the sorbent surface, as well as preventing CO_2 diffusion and absorption [193]. As a consequence, a substantial amount of inactive CaO cycles through the calcium looping system are produced, increasing capital and operational expenses [194].

To increase the performance of CaO-based sorbents, several approaches have been suggested, including pore structure manipulation and new metal doping. The use of sintering-resistant inert supports as CaO dopants (Si, Ti, Cr, Co, Zr, and Ce) is widely established. This includes spreading CaO in a stable, solid matrix composed of the inert substance, so preserving the accessible active surface layer of CaO, and reducing conversion loss with cycling [195].

The Tammann temperature may be used to predict a material's tendency to sintering. The following equation describes the relationship between Tammann(T) and melting temperatures T_m using the unit of kelvin K:

$$T_T = 0.5\ T_m$$

As a result, supporting materials having melting temperatures greater than $CaCO_3$(1339 °C) would potentially provide sintering resistance to the sorbent [196]. Some researchers believe that this semi-empirical association is oversimplified. Since the commencement of sintering is affected by other parameters such as particle size and shape and the degree of porosity.

Additionally, calcium aluminates have repeatedly been found to resist sintering while having a relatively low Tammann temperature [197]. The investigation of inert support materials involving a variety of refractories of Zr [198], Al [199-200], La [201], Mg [202] and Y [203] dopants has resulted in sorbents that function well for CO_2 collection. By using the flame spray pyrolysis (FSP) technique, $CaO/CaZrO_3$ has been produced and investigated the impact of various zirconia loadings on the capture mechanism [204]. Additionally, CaO absorbent may be utilized to capture CO_2 at high temperatures and SO_2 conditions [205].

CeO_2 is an excellent inert material with a Tammann temperature of 1064 °C, which may similarly be integrated into CaO. Lately, there is no more scientist studying this subject through the use of a co-precipitation technique; a number of metal-doped calcium-based sorbents, such as Cr, Mn, Cu, Ce, and Co, have been developed. Some researchers examined the effects of Al, W, Hf, Ce, and Y on the Zr/Ca sorbents' ability to trap particles. While the comparison of Zr/Ca sorbent and Ce-doped Zr/Ca sorbent did not exhibit any clear positive impacts. At 700 °C, CaO, CeZr-doped sorbent was integrated with $CexZr1\text{-}xO_2$ and

LaAlyMg1-yO_3. The research has not investigated the effect of CeO_2 on the long-term viability of CaO-based sorbents for CO_2 collection. Therefore, an examination using the CaO-based sorbents doped with CeO_2 for CO_2 collection is still required [162].

The objective of this study is to provide some new findings regarding the precipitation-calcination process of producing CaO nanoparticles. The product is characterized using a variety of analytical methods, and the outcomes of CO_2 absorption studies at lower temperatures are also reported.

Knowledge gap: (i) The missing information is that is it possible to capture CO_2 at low temperatures? (ii) Moreover, can metal oxide-doped CaO nanoparticles control the stability of CO_2 capturing at low temperatures?

2.6 Scientific Goals

In this research, two main categories are contained: the theoretical calculations of the metal oxide nanoparticles and the experimental results of the produced nanoparticles.

- Based on a theoretical strategy, to calculate the possibility of the metal oxide nanoparticles by using precipitation-calcination method from metal chlorides and NaOH.
- To suggest the possibility of producing different metal oxide nanoparticles based on theoretical calculation. Moreover, to experimentally produce different metal oxide nanoparticles using the precipitation-calcination process, including CaO, CoO/Co_3O_4, NiO, Fe_2O_3 calcination in air.
- To produce three different metal oxides doped to CaO by using precipitation-calcination method.
- To analyze the characterizations of pure CaO and the metal oxides (CoO/Co_3O_4, NiO Fe_2O_3) doped CaO nanoparticles. The samples will be characterized using different characterization methods such as Scanning Electron Microscope (SEM), Transmission Electron Microscope (TEM), X-ray Diffraction (XRD), Energy Dispersive Spectroscopy (EDS) and BET analysis of the specific surface area and pore size.
- To analyze the capturing of CO_2 and compare the absorption capacity of pure CaO and three different metal oxides doped CaO nanoparticles.

3. Theoretical calculation of the metal oxide synthesis through the precipitation-calcination method

As an example, the synthesis of CaO nano-particles by adding NaOH solution dropwise to $CaCl_2$ solution and forming $Ca(OH)_2$ precipitates, and after washing-filtering it to calcine it to form CaO. This was done to capture CO_2 with the formation of $CaCO_3$. Firstly, NaOH is indeed a suitable reagent. There are several reasons for that:

1. NaOH is a bulk and cheap reagent. It is produced as a side product of the PVC industry, where they produce Cl_2 gas on the anode by electrochemical disintegration of NaCl from a water solution and forming NaOH on the cathode. The huge amount of NaOH formed nearby to Miskolc in Kazincbarcika at BorsodChem / Wanhua chemical plant makes NaOH a cheap reagent.

2. NaOH has good solubility in water: 100 g/100 g of H_2O at 25 °C. The molar mass of NaOH of 40.0 g/mol provides 10.5 M solubility at 0 °C and 86.8 M solubility at 100 °C.

3. The product of the reaction with NaOH is NaCl. From the initial 2 M NaOH solution, a maximum of 2 M NaCl solution is formed. Its solubility is 36 g/100 g of H_2O at 25 °C. The molar mass of 58.4 g/mol of NaCl is 6.1 M at 0 °C and 6.70 M solubility of NaCl in water. Therefore, 2M of NaCl is much lower than its soluble molarity in water. In the reaction, NaCl will not co-precipitate with the hydroxide product and will not contaminate it.

4. During the reaction, NaOH is converted into NaCl; it can be done efficiently if the difference between their molar standard Gibbs energies is as negative as possible. The molar standard Gibbs energy of the formation of NaCl is -383.9 kJ/mol (300 K) and -374.6 kJ/mol (400 K). The molar standard Gibbs energy of the formation of NaOH is -379.5 kJ/mol (300 K) and -363.8 kJ/mol (400 K).
Thus, the molar standard Gibbs energy change accompanying the transformation of NaOH into NaCl is -4.4 kJ/mol (300 K) and -10.8 kJ/mol (400 K).

Therefore, it will help the transformation of other chlorides into hydroxides. The calculation of the following steps is based on the CRC Handbook of Chemistry and Physics [206] and Barin Thermochemical Data of Pure Substances [207].

3.1 Condition 1. Existence and solubility of a stable chloride for a given metal

The reaction takes place between an aqueous solution of the metal chloride (MCl_x) and NaOH. The first condition is whether the given metal has a stable chloride and whether its solubility in water is sufficient. To be sufficient, the solubility should be larger than the planned concentration. The planned concentration should be taken in stoichiometry with 2 M NaOH. Thus, for MCl_x, the required solubility,

$$s_{r(MClx)} = 2/x \text{ M} \qquad \text{Eq 3.1-1}$$

Where S_r = required solubility in molarity M, x = the positive integer.
If $MCl_x = CaCl_2$, x = 2; $s_{r(CaCl2)} = 2/x = 1$ M

Thus, the solubility of MCl_x should be higher than 2/2 = 1 M. Its actual solubility is 81.3 g/100 g of H_2O at 20 °C. But the solubility given in g/100g of H_2O, the unit can be recalculated to the unit of molarity M.

$$s_{a(M)(MClx)} = s_{a(g)MClx} * 10 / M_{MClx} \qquad \text{Eq 3.1-2}$$

Where $s_{a(M)(MClx)}$ = the actual solubility of metal chloride with unit molarity M, $s_{a(g)MClx}$ = actual solubility of metal chloride with unit g/100 g of H_2O, M_{MClx} = molar mass of metal chloride with unit g/mol.

As these values are higher than the required value of 1 M, M = Ca obeys the condition.

In Table 3.1.1, the metal chlorides are listed that have sufficient solubility for this technology: M = Al, Au (III), Ba, Be, Ca, Cd, Co (II), Cs, Cu (II), Fe (III), Fe (II), In (III), K, La, Li, Mg, Mn (II), Na, Nd, Ni (II), Pr, Pt (IV), Rb, Sb (III), Sm (III), Sn (II), Sr, Y, Zn. These are altogether 29 chlorides for 29 metals. The metals which do not obey condition 1 are: M = Ag (I), Au (I), Cu (I), Hg (I), Hg (II), Pb (II), Ra, Tl (I), as seen in Table 3.1.2. These metals are excluded from further consideration.

Table 3.1.1: Metals chlorides with high enough solubilities obey condition I

M	x	s_{rMClx} (M)	$s_{a(g)(MClx)}$ g/100g H_2O	M_{MClx} (g/mol)	$s_{a(M)(MClx)}$ (M)
		Eq 3.1.1			Eq 3.1.2
Al	3	0.67	45.1	133.33	3.38
Au	3	0.67	68	303.35	2.24
Ba	2	1	37	208.2	1.78
Be	2	1	71.5	79.91	8.95
Ca	2	1	81.3	110.98	7.33
Cd	2	1	120	183.3	6.55
Co	2	1	56.2	129.83	4.33
Cs	1	2	191	168.35	11.35
Cu	2	1	75.7	134.45	5.63
Fe	2	1	65	126.75	5.13
Fe	3	0.67	91.2	162.2	5.62
In	3	0.67	195.1	221.15	8.82
K	1	2	35.5	74.55	4.76
La	3	0.67	95.7	245.25	3.90
Li	1	2	84.5	42.39	19.93
Mg	2	1	56	95.21	5.88
Mn	2	1	77.3	125.84	6.14
Na	1	2	36	58.44	6.16
Nd	3	0.67	100	205.55	4.86
Ni	2	1	67.5	129.59	5.21
Pr	3	0.67	96.1	247.25	3.89
Pt	4	0.5	142	336.9	4.21
Rb	1	2	93.9	120.92	7.77
Sb	3	0.67	987	228.15	43.26
Sm	3	0.67	93.8	256.75	3.65
Sn	2	1	178	189.6	9.39
Sr	2	1	54.7	158.52	3.45
Y	3	0.67	75.1	195.26	3.85
Zn	2	1	408	136.28	29.94

Table 3.1.2: Metals chlorides with not sufficient solubilities which do not obey condition I

M	x	s_{rMClx} (M)	$s_{a(g)(MClx)}$ g/100g H_2O	M_{MClx} (g/mol)	$s_{a(M)(MClx)}$ (M)
		Eq 3.1.1			Eq 3.1.2
Ag	1	2	0.00019	143.32	1.33E-05
Au	1	2	0.000031	232.42	1.33E-06
Cu	1	2	0.0047	98.99	4.75E-04
Hg	2	1	7.31	271.52	0.23
Hg	1	1	0.0004	472.09	8.47E-06
Pb	2	1	1.08	278.1	0.04
Ra	2	1	24.5	296.09	0.83
Tl	1	2	0.33	189.68	0.02

3.2 Condition 2. Spontaneous reaction between metal chloride and NaOH

The reaction is written as:

$$MCl_x + x\ NaOH = x\ NaCl + M(OH)_x \qquad \text{Eq 3.2-1}$$

Where MCl_x = metal chloride, x = positive integer, $M(OH)_x$ = metal hydroxide. This reaction will be spontaneous if the standard molar Gibbs energy change accompanying this reaction is as negative as possible. As there are (1+x) moles on both sides of the above reaction, the concentration ratio of $M(OH)_x$ / MCl_x is the (1+ x) root of the equilibrium constant of reaction 3.2.1. To have a sufficient driving force for this reaction, which is needed for fast reaction and that is needed for fast nucleation and that is needed for nano-structure, at least 100 should be the ratio of concentrations $M(OH)_x$ / MCl_x. So, the equilibrium constant of reaction (3.2-1) should be $K = 100^{1+x}$. From here, the standard Gibbs energy change of reaction (3.2-1) should be more negative than the following value.

$$\Delta_r G^0_{required} = -4.61RT(1+x) \qquad \text{Eq 3.2-2}$$

where $\Delta_r G^0_{required}$ = the required Gibbs free energy value for the reaction with unit kJ/mol, R = gas constant value with unit $Jmol^{-1}K^{-1}$, T= Temperature with unit K.

If M = Ca and x = 2, the standard Gibbs energy change of reaction (3.2-2) should be more negative than -115T, i.e. for T = 300 K, it should be more negative than -34.5 kJ/mol.

$$\Delta_{r1} G^0 = (\Delta_f G^0_{M(OH)x} - \Delta_f G^0_{MClx}) \qquad \text{Eq 3.2-3}$$

$$\Delta_{r2} G^0 = (\Delta_f G^0_{NaOH} - \Delta_f G^0_{NaCl}) \qquad \text{Eq 3.2-4}$$

The calculation of Gibbs free energy value for the reaction 3.2-1 is;

$$\Delta_{r3}G^0 = \Delta_{r1}G^0 - x\Delta_{r2}G^0 \qquad \text{Eq 3.2-5}$$

where $\Delta_{r1}G^0$, $\Delta_{r2}G^0$, $\Delta_{r3}G^0$ = Gibbs free energy value for the reaction with unit kJ/mol, $\Delta_f G^0_{M(OH)x}$= the standard molar Gibbs energy of formation of metal hydroxide with unit kJ/mol, $\Delta_f G^0_{MClx}$ = the standard molar Gibbs energy of formation of metal chloride with unit kJ/mol, $\Delta_f G^0_{NaOH}$ = the standard molar Gibbs energy of formation of NaOH with unit kJ/mol, $\Delta_f G^0_{NaCl}$ = the standard molar Gibbs energy of formation of NaCl with unit kJ/mol.

The standard molar Gibbs energies of the formation of $CaCl_2$, $\Delta_f G^0_{CaCl2}$ is -747,8 kJ/mol (300 K). For $Ca(OH)_2$, $\Delta_f G^0_{Ca(OH)2}$ is: -897.9 kJ/mol (300 K). Thus, converting $CaCl_2$ into $Ca(OH)_2$ is accompanied by the molar standard Gibbs energy change = -150.1 kJ/mol (300 K). Comparing it to the above values, the molar standard Gibbs energy change accompanying the transformation of NaOH into NaCl; $\Delta_{r2}G^0$ is -4.4 kJ/mol (300 K). The standard molar Gibbs energy change of (3.2-3) for $CaCl_2$ (300 K) is -150.1 – 2 * (-4.4) = -141.31 kJ/mol.

The value of standard molar Gibbs energy change is more negative than the above-mentioned criteria (-34.5 kJ/mol at 300 K). Therefore, as a conclusion, M = Ca condition 2 is also obeyed.

In Table 3.2.1, the metals are listed for which condition 2 is also obeyed from the above list of 29 chlorides (for which condition 1 is obeyed): M = Al, Au (III), Ba, Be, Ca, Cd, Co (II), Cu (II), Fe (III), Fe (II), Li, Mg, Mn (II), Ni (II), Sb (III), Sn (II), Sr, Zn = 18 chlorides for 18 metals. The metals which do obey condition 1 but do not obey condition 2 are: M = Cs, In (III), K, La, Na, Nd, Pr, Pt (IV), Rb, Sm (III), Y as seen in Table 3.2.2. These metals are excluded from further consideration.

Table 3.2.1: $\Delta_r G$ (kJ/mol) for the required and the actual value of the reactions at T = 300K from reactions 3.2-5, which obey condition 2 (passed condition 1 from Table 3.1.1)

M	x	$\Delta_f G^0_{MClx}$	$\Delta_f G^0_{M(OH)x}$	$\Delta_{r1} G^0$	$\Delta_r G^0_{required}$	$\Delta_{r3} G^0$
				Eq 3.2.3	Eq 3.2.2	Eq 3.2-5
Al	3	-629.5	-1137.8	-508.32	-45.99	-495.12
Au	3	-47.3	-316.2	-268.80	-45.99	-255.60
Ba	2	-809.9	-858.9	-48.96	-34.49	-40.16
Be	2	-449.2	-815.4	-366.19	-34.49	-357.39
Ca	2	-747.8	-897.9	-150.11	-34.49	-141.31
Cd	2	-343.6	-473.2	-129.61	-34.49	-120.81
Co	2	-269.4	-453.6	-184.25	-34.49	-175.45
Cu	2	-173.5	-358.5	-184.97	-34.49	-176.17
Fe	2	-302	-486.5	-178.37	-34.49	-169.57
Fe	3	-333.5	-695.7	-362.18	-45.99	-348.98
Li	1	-383.9	-423.2	-54.81	-23.00	-50.41
Mg	2	-591.8	-833.1	-313.31	-34.49	-304.51
Mn	2	-440.2	-608.14 [208]	-170.23	-34.49	-161.43
Ni	2	-258.8	-452 [208]	-188.42	-34.49	-179.62
Sb	3	-322	-644.4 [209]	-322.30	-45.99	-309.10
Sn	2	-285.9	-493.86 [210]	-594.59	-34.49	-585.79
Sr	2	-779.65	-880.5	285.79	-34.49	294.59
Zn	2	-369.1	-553.2 [211]	-184.13	-34.49	-175.33

Table 3.2.2: $\Delta_r G$ kJ/mol for the required and the actual value of the reactions at T = 300K from reactions 3.2.3, which do not obey condition 2 (passed condition 1 from Table 3.1.1)

M	x	$\Delta_f G^0_{MClx}$	$\Delta_f G^0_{M(OH)x}$	$\Delta_{r1} G^0$	$\Delta_r G^0_{required}$	$\Delta_{r3} G^0$
				Eq 3.2.3	Eq 3.2.2	Eq 3.2-5
Cs	1	-414.2	-370.4	43.778	-23.00	48.178
In	3	-461.7	-	-	-	-
K	1	-408.6	-378.6	29.981	-23.00	34.381
La	3	-994.9	-	-	-	-
Na	1	-383.9	-379.5	4.356	-23.00	8.756
Nd	3	-966.1	-	-	-45.99	-
Pt	4	-163.3	-	-	-	-
Pr	3	-980.3	-	-	-	-
Rb	1	-407.6	-	-	-	-
Sm	3	-765.9	-	-	-	-
Y	3	-927.3	-	43.778	-	-

3.3 Condition 3. Fast precipitation of metal hydroxide

The metal hydroxide formed in the previous step should precipitate fast in order to form nano crystallite. For that, the solubility of metal hydroxide should be much lower than actual concentration. The concentration of metal hydroxide is a maximum about 1/x M (supposing the same volume of NaOH solution is added to the same volume of metal chloride solution). To make sure the precipitation is fast, it is required at least 10 times less solubility, i.e., below 0.1/x M.

$$s_{(\text{required})M(OH)x} = 0.1/x \text{ M} \qquad \text{Eq 3.3-1}$$

Where $s_{(\text{required})M(OH)x}$ = the required solubility of metal hydroxides with unit molarity M.

For $Ca(OH)_2$, x = 2, so actual solubility should be below 0.05 M in water. The actual value $s_{a(g)(Ca(OH)2)}$ with unit g/ 100 g of H_2O is 0.16 g/ 100 g (20 °C). The unit should be recalculated to molarity. Therefore, the actual solubility $Ca(OH)_2$ with unit molarity is, $s_{a(M)(Ca(OH)2)}$ = 0.0250 M (0 °C) and 0.010 M (100 °C). As that value is below the required of 0.05 M, M = Ca, obeys condition 3.

Those metals which obey this condition are listed in Table 3.3.1. Their hydroxides are expected to precipitate speedily: M = Al, Au (III), Be, Ca, Cd, Co (II), Cu (II), Fe (III), Fe (II), Mg, Mn (II), Ni (II), Sb (III), Sn (II), Zn = 15 hydroxides of 15 metals. This is less than after condition 2; the missing metals are: Ba, Li, Sr. Those metals which do obey condition 2 but do not obey condition 3 as seen in Table 3.3.2. These metals are excluded from further consideration.

Table 3.3.1: The metal hydroxides that have low enough solubility in water at T = 300K which obey condition 3 (passed condition 2 from Table 3.2.1)

M	x	$s_{a(g)(M(OH)x)}$	$M_{M(OH)x}$	$s_{(required)M(OH)x}$	$s_{a(M)(M(OH)x)}$
		g/ 100g H_2O	g/mol	M	M
Al	3	0	78	0.033	0
Au	3	0	247.9	0.033	0
Be	2	0	43.01	0.050	0
Ca	2	0.16	74.1	0.050	0.022
Cd	2	0.00015	146.4	0.050	1.02E-05
Co	2	0	92.9	0.050	0
Cu	2	0	97.6	0.050	0
Fe	2	0.000052	89.9	0.050	5.78E-06
Fe	3	0	106.9	0.033	0
Mg	2	0.00069	58.3	0.050	1.18E-04
Mn	2	0.00034	88.9	0.050	3.82E-05
Ni	2	0.00015	92.7	0.050	1.62E-05
Sb	3	0	172.78	0.033	0
Sn	2	0	152.7	0.050	0
Zn	2	0.000042	99.42	0.050	4.22 E-06

Table 3.3.2: The metal hydroxides that have low enough solubility in water at T = 300K which do not obey condition 3 (passed condition 2 from Table 3.2.1)

M	x	$s_{a(g)(M(OH)x)}$	$M_{M(OH)x}$	$s_{(required)M(OH)x}$	$s_{a(M)(M(OH)x)}$
		g/ 100g H_2O	g/mol	M	M
Ba	2	4.91	171.3	0.050	0.29
Li	1	12.5	23.9	0.100	5.23
Sr	2	2.25	121.6	0.050	0.19

3.4 Condition 4. Ability of metal hydroxide to convert into metal oxide upon heating

The following chemical reaction is expected that metal hydroxide converts to metal oxides:

Case I: if x = even (2, 4, 6….)

$$M(OH)_x = \frac{x}{2} H_2O + MO_{\frac{x}{2}} \qquad \text{Eq 3.4-1}$$

Case II: if x = odd (1, 3, 5….)

$$2\ M(OH)_x = x\ H_2O + M_2O_x \qquad \text{Eq 3.4-2}$$

If x = 2, the reaction 3.4-1 can be written: $M(OH)_2 = H_2O + MO$

As the only gaseous component of the reaction equation, 3.4-1 and 3.4-2 are on the right-hand side; this reaction will be shifted to the right with increasing temperature. Therefore, it is expected that at least some of the hydroxides will thermally decompose at a higher temperature. This reaction should take place spontaneously, preferably without using vacuum, at a reasonably low temperature, meaning at least below half of the melting point of metal oxide, denoted as T* or T_T (Tammann temperature). Meanwhile, T_T is the same as the decomposition temperature of metal hydroxide. As above this temperature, the nano-particles will easily sinter and lose their nanostructure. The decomposition temperature of equations 3.4-1 and 3.4-2 are known. Moreover, the decomposition temperature of metal hydroxides should be in a reasonable engineering range, not above 1500 K.

For $M(OH)_x$, M = Ca, x = 2. The decomposition temperature of $Ca(OH)_2$, $T_{D(Ca(OH)2)}$ is about 823 K < 1500 K. Therefore, the decomposition temperature is within the range of common temperature as an engineering point of view. Moreover, the melting point of CaO, $T_{m(CaO)}$ = 3171 K, half of it, $\frac{1}{2}T_{m(CaO)}$= 1585 K > 823 K. Thus, condition 4 is obeyed for M = Ca, where $T_{D(M(OH)x)}$ = the decomposition temperature of metal hydroxides with the unit kelvin K, $T_{m(MOx)}$ = the melting point of metal oxides with the unit kelvin K.

Table 3.4.1 shows the metals which obey this condition and using the technology; chloride + NaOH = hydroxide + NaCl + washing + precipitation of hydroxide + calcination leading to an oxide; the following 13 oxides can be produced. M = Al, Be, Ca, Cd, Co (II), Cu (II), Fe (III), Fe (II), Mg, Mn (II), Ni (II), Sn (II), Zn = 13 oxides of 13 metals. The metals which do not obey this condition: Au (III), Sb (III) as seen in Table 3.4.2.

Table 3.4.1: Ability of metal hydroxide to convert into metal oxide upon heating which obeys condition 4 (passed condition 3 from Table 3.3.1)

M	x	T_m MO_x or T_m M_2O_x	½[T_m MO_x or T_m M_2O_x]	T_D $M(OH)_x$
		K	K	K
Al	3	2326	1163 [212-214]	473-873
Be	2	2850	1425	473-500
Ca	2	3171	1585.5	823
Cd	2	1700	850	403
Co	2	2103	1051.5	433
Cu	2	1719	859.5	353
Fe	2	1650	825 [215]	523-623
Fe	3	1838	919	523-923
Mg	2	3098	1549 [67]	605
Mn	2	2112	1056 [216-218]	300
Ni	2	2228	1114	503
Sn	2	1080	540 [219]	250-500
Zn	2	2248	1124	413

Table 3.4.2: Ability of metal hydroxide to convert into metal oxide upon heating which do not obey condition 4 (passed condition 3 from Table 3.3.1)

M	x	T_m M_2O_x	½ T_m M_2O_x	T_D $M(OH)_x$
		K	K	K
Au	3	423	211.5	373
Sb	3	929	464	-

3.5 Additional Condition: CO_2 capturing efficiency of the metal oxide produced by the precipitation-calcination method

All the above is done in order to produce an oxide that is able to capture CO_2, according to the reaction:

Case I: if x = even (2, 4, 6….)

$$MO_{\frac{x}{2}} + \frac{x}{2} CO_2 = M(CO_3)_{\frac{x}{2}} \qquad \text{Eq 3.5-1}$$

Case II: if x = odd (1, 3, 5….)

$$M_2O_x + x\ CO_2 = M_2(CO_3)_x \qquad \text{Eq 3.5-2}$$

where, $MO_{\frac{x}{2}}$, M_2O_x = metal oxides, $M(CO_3)_{\frac{x}{2}}$, $M_2(CO_3)_x$ metal carbonates.

If x = 2, reaction (3.5-1) simplifies as: $MO + CO_2 = CaCO_3$

As in the reaction, the gaseous component is on the left-hand side; this reaction will be shifted to the left with increasing T. Thus, let us check the possibility of this reaction at T = 300 K. If it does not work at T = 300 K, it will not work at higher temperatures either.

The current concentration of CO_2 in the atmosphere is 420 ppm. To call a capturing technology efficient, it should decrease this value by 10 times. Thus, reaction equation 3.5-1 should have an equilibrium at a partial pressure of CO_2 of 42 ppm i.e., p = 4.2 E-5 bar. Thus, the equilibrium constant of reaction 3.5.1 should be at least the inverse of this value to the power of K = 2/x: $(2.38\ E4)^{2/x}$ at least at T = 300 K.

If M = Ca: x = 2, i.e., K should be at least 2.38 E4 at T = 300 K. This is possible if the molar standard Gibbs energy accompanying reaction 3.5-1, $\Delta_{r4}G^0$ is more negative than – RTlnK = - 25.1 kJ/mol. The standard molar Gibbs energies of formation at T = 300 K are $\Delta_f G^0_{CaO}$ = -603.3 kJ/mol, $\Delta_f G^0_{CO2}$ = - 394.4 kJ/mol, $\Delta_f G^0_{CaCO3}$= - 1127.3 kJ/mol.

Thus, the standard molar Gibbs energy change accompanying reaction 3.5.1 is

Case I : if x = even (2,4,6,….)

$$\Delta_{r4}G^0 = \Delta_f G^0_{M(CO3)_{\frac{x}{2}}} - (\Delta_f G^0_{MO_{\frac{x}{2}}} + \frac{x}{2}\Delta_f G^0_{CO2}) \qquad \text{Eq 3.5-3}$$

Case II : if x = odd (1,3,5,….)

$$\Delta_{r5}G^0 = \Delta_f G^0_{M_2(CO3)_x} - (\Delta_f G^0_{M_2O_x} + x\Delta_f G^0_{CO2}) \qquad \text{Eq 3.5-4}$$

where $\Delta_{r2}G^0$, $\Delta_{r3}G^0$ = the standard molar Gibbs energy change accompanying reaction with unit kJ/mol, $\Delta_f G^0_{M(CO3)_{\frac{x}{2}}}$, $\Delta_f G^0_{M_2(CO3)_x}$ = the standard molar Gibbs energies of formation of metal carbonates with unit kJ/mol, $\Delta_f G^0_{MO_{\frac{x}{2}}}$, $\Delta_f G^0_{M_2O_x}$= the standard molar Gibbs energies of formation of metal oxides with unit kJ/mol, $\Delta_f G^0_{CO2}$ = the standard molar Gibbs energies of formation of CO_2 with unit kJ/mol.

If M = Ca, the standard molar Gibbs energy change accompanying reaction 3.5-3 is -129.6 kJ/mol at T = 300 K, which is more negative than -25.1 kJ/mol. So, as a conclusion CaO is efficient in capturing CO_2.

Table 3.5.1 shows the metal oxides which also satisfy this condition: M = Ca, Cd, Co (II), Mn (II), i.e., the following oxides (i) can be produced using our technology and at the same time (ii) they are able to capture CO_2. In sequence from the strongest to the weakest: CaO, MnO, CdO, CoO. So, the best is CaO. FeO, MgO, ZnO and NiO are weaker in reaction for carbonation. Al_2O_3, BeO, CuO, Fe_2O_3 and SnO are not obeyed for carbonation as seen in Table 3.5.2.

Table 3.5.1: CO_2 capturing efficiency of the metal oxide at T= 300K, which obeys additional condition (passed condition 4 from Table 3.4.1)

M	x	2/x	K	-RTlnK	$\Delta_{r4}G^0$ (Eq 3.5-3)
				kJ/mol	kJ/mol
Ca	1	2	23800	-25.14	-130.94
Cd	1	2	23800	-25.14	-46.86
Co	1	2	23800	-25.14	-28.22
Mn	1	2	23800	-25.14	-59.42

Table 3.5.2. CO_2 capturing efficiency of the metal oxide at T= 300K, which do not obey additional condition (passed condition 4 from Table 3.4.1)

M	x	2/x	K	-RTlnK	$\Delta_{r4}G^0$ or $\Delta_{r5}G^0$ Eq 3.5.3 or Eq 3.5.4
				kJ/mol	kJ/mol
Fe	1	2	23800	-25.14	-20.87
Mg	1	2	23800	-25.14	-16.58
Ni	1	2	23800	-25.14	-11.97
Zn	1	2	23800	-25.14	-16.64
Al	3	0.67	23800	-25.14	-
Be	1	2	23800	-25.14	-
Cu	1	2	23800	-25.14	-
Fe	3	0.67	23800	-25.14	-
Sn	1	2	23800	-25.14	-

4. Materials and methods

4.1 Materials

$CaCl_2xH_2O$ (≥95%, Sigma Aldrich), $CoCl_2xH_2O$ (≥99%, VWR Ltd.), $FeCl_3xH_2O$ (≥95%, Sigma Aldrich), $NiCl_2xH_2O$ (≥99%, VWR Ltd.), and NaOH (≥98%, VWR Ltd.) were used as reactants for the preparation of the samples. Different concentrations of these reactants were used for the synthesis. 1M concentration of $CaCl_2$, $CoCl_2$, $FeCl_3$, $NiCl_2$ and 2M concentration of NaOH were prepared by using distilled water.

4.2 Synthesis of metal oxides nanoparticles by using precipitation-calcination method

In this section, the preparations of pure metal oxides CaO, CoO/Co_3O_4, Fe_2O_3 and NiO are described. Each metal chloride and NaOH were used as the initial reagents for the synthesis of $M(OH)_2$ powder. First, both aqueous solutions (MCl_x and NaOH) were heated up to 80 °C separately. At this fixed temperature, a given NaOH solution was added dropwise to a given MCl_x solution under stirring at 1300 rpm by a magnetic stirrer for 30 minutes. The process takes place according to the following reaction:

$$MCl_{x(aq)} + xNaOH_{(aq)} \longrightarrow M(OH)_{x(s)} + xNaCl_{(aq)} \qquad \text{Eq 4.2-1}$$

As a result, the precipitates were formed. After that, the mixtures were filtered and washed five times with 120 ml of distilled water per occasion to remove NaCl from the suspension. A white precipitate of $Ca(OH)_2$, pinky precipitate of $Co(OH)_2$, a reddish precipitate of $Fe(OH)_3$ and a greenish precipitate of $Ni(OH)_2$ in the reactions:

$$M(OH)_{x(s)} + xNaCl_{(aq)} + nH_2O \longrightarrow nH_2O + xNaCl_{(aq)} / M(OH)_{x(s,wet)} \qquad \text{Eq 4.2-2}$$

The wet precipitates of $M(OH)_x$ were dried in air at room temperature over one night to collect a semi-dry precipitate $M(OH)_x$. The color of the dry precipitate can be seen in Figure 4.2. The collected semi-dry precipitates of $M(OH)_x$ were calcined in the furnace with a heating rate of 15 °C/min in air. As a result, metal oxides CaO, CoO/Co_3O_4, Fe_2O_3 and NiO powder were produced by calcination while the dissociation product H_2O was evaporated, as shown in the following equation:

Case I: if x = even (2, 4, 6, ….)

$$M(OH)_{x(s)} \longrightarrow MO_{\frac{x}{2}} + \frac{x}{2} H_2O \uparrow \qquad \text{Eq 4.2-3}$$

Case II: if x = odd (1,3, 5….)

$$2M(OH)_{x(s)} \rightarrow M_2O_x + xH_2O \uparrow \qquad \text{Eq 4.2-4}$$

The calcined powder of the metal oxides can be seen in Figure 4.2-1. In fact, CoO nanoparticles were produced initially; i.e CoO oxidized in air and transformed to Co_3O_4 [49]. Therefore, only Co_3O_4 has been detected. The molarity, volume, precipitate color, and calcination temperature for each metal oxide are mentioned in the following Table 4.2.1.

Table 4.2.1: The molarity and volume of the reactants used in the synthesis

MCl_x	$V_{MClx(aq)}$ 1M	$V_{(NaOH)(aq)}$ 2M	Precipitate color	Calcination temperature °C	$MO_{\frac{x}{2}}$ or M_2O_x or $M_{3x/2}O_{2x}$
	mL	mL			
$CaCl_2$	20	20	White	650	CaO
$CoCl_2$	20	20	Light pink	170	CoO/Co_3O_4
$NiCl_2$	20	20	Light green	600	NiO
$FeCl_3$	20	30	Dark red	450	Fe_2O_3

Figure 4.2-1: The precursors of metal oxides $Ca(OH)_2$, $Co(OH)_2$ and $Ni(OH)_2$

4.2.1 The calcination of CaO nanoparticles calcined from wet precipitate in different environments

There are two types of calcination conditions. Table 4.2.2 mentions the CaO samples as a function of temperatures and calcination environment. The two samples were used to analyze the crystallite size and the formation of hydroxide to oxide.

Table 4.2.2: The list of the samples upon the calcination temperatures and environments during the calcination process

Sample name	Composition	Calcination	Environment
Sample 1	CaO	wet precipitate at 25 ºC to 650 ºC	vacuum
Sample 2	CaO	wet precipitate 25 ºC to 650 ºC	in air

4.3 Synthesis of metal oxides doped CaO nanoparticles

In this section, the synthesis of three metal oxides CoO, Fe_2O_3 and NiO doped calcium oxides nanoparticles are described. In the synthesis, 0.1:1 ratio of MCl_x to $CaCl_2$ was used to obtain $M(OH)_2$:$Ca(OH)_2$ powder. To prepare high doping amount, 0.5:1 ratio of MCl_x to $CaCl_2$ was used in the reactions with NaOH. The composition, concentrations, and volume of the solution for the reactions are described in Table 4.3. Based on this information, the sample was named in this dissertation, as seen in Table 4.3.

Table 4.3: Compositions, concentrations, and volume of the solution prepared at 1300rpm stirring speeds to produce CoO doped CaO, NiO doped CaO and Fe_2O_3 doped CaO

Names of the samples	$CoCl_2$		$CaCl_2$		NaOH	
	Concentration (mol/L)	Volume (mL)	Concentration (mol/L)	Volume (mL)	Concentration (mol/L)	Volume (mL)
0.1CoO:CaO	1	2	1	20	2	22
0.5CoO:CaO	1	10	1	20	2	30
	$NiCl_2$					
0.1NiO:CaO	1	2	1	20	2	22
0.5NiO:CaO	1	10	1	20	2	30
	$FeCl_3$					
0.05Fe_2O_3:CaO	1	1	1	10	2	11.5
0.25Fe_2O_3:CaO	1	5	1	10	2	17.5

The initial reagents $CoCl_2$/ $NiCl_2$/$FeCl_3$, $CaCl_2$ and NaOH solutions were synthesized to produce metal oxides CoO, Fe_2O_3 and NiO doped CaO nanoparticles. First, all of the aqueous solutions ($CoCl_2$ /$NiCl_2$ /$FeCl_3$, $CaCl_2$ and NaOH) were heated up to 80 °C. At that fixed temperature, a given NaOH solution was added dropwise to the mixture of $CoCl_2$ + $CaCl_2$, $NiCl_2$ + $CaCl_2$ and $FeCl_3$ + $CaCl_2$ solution under stirring at 1300 rpm by a magnetic stirrer for 30 minutes. During the wet synthesis process, a light color precipitate for low doping precipitate and dark color precipitate for high doping precipitate was formed. The chemical reaction is as follows:

$$zMCl_{x(aq)} + CaCl_2 + (2+zx)\ NaOH_{(aq)} \rightarrow zM(OH)_{x(s)} + Ca(OH)_{2(s)} + (2+zx)\ NaCl_{(aq)} \quad \text{Eq 4.3-1}$$

where z = 0.1, 0.5 doping amount (mole/ 1 mole of $CaCl_2$) for $NiCl_2$ and $CoCl_2$, z = 0.05, 0.25 doping amount (mole/ 1 mole of $CaCl_2$) for $FeCl_3$, x = positive integer

After that, the mixture was filtered and washed five times with 100- 150 ml of distilled water per occasion to remove NaCl from the suspension. The duration of each filtering process was 2-3 hr. As a result, light pink-purple color precipitate for 0.1:1 and dark pink-purple color precipitate for 0.5:1 of $Co(OH)_2$:$Ca(OH)_2$ were formed as seen in Figure 4.3 a. Light greenish colour precipitate for 0.1:1 and dark greenish colour precipitate for 0.5:1 of $Ni(OH)_2$:$Ca(OH)_2$ were formed as seen in Figure 4.3 b. Light reddish precipitate for 0.1:1 and a dark reddish color precipitate for 0.5:1 of $Fe(OH)_3$:$Ca(OH)_2$ were formed, as seen in Figure 4.3 c. The precipitates occurred according to the reactions:

$$M(OH)_x\text{: } Ca(OH)_{2(s)} + NaCl_{(aq)} + H_2O \rightarrow \begin{cases} H_2O + NaCl_{(aq)} \text{ (passed the filter)} \\ M(OH)_x\text{: } Ca(OH)_{2(\text{wet solid})} \text{ (filtered wet precipitate)} \end{cases} \quad \text{Eq 4.3-2}$$

The wet precipitate of z($Co(OH)_2$:$Ca(OH)_2$, $Ni(OH)_2$:$Ca(OH)_2$ and $Fe(OH)_3$:$Ca(OH)_2$) were dried at room temperature over one night in air to collect a semi-dry precipitate z($Co(OH)_2$:$Ca(OH)_2$, $Ni(OH)_2$:$Ca(OH)_2$ and $Fe(OH)_3$:$Ca(OH)_2$).

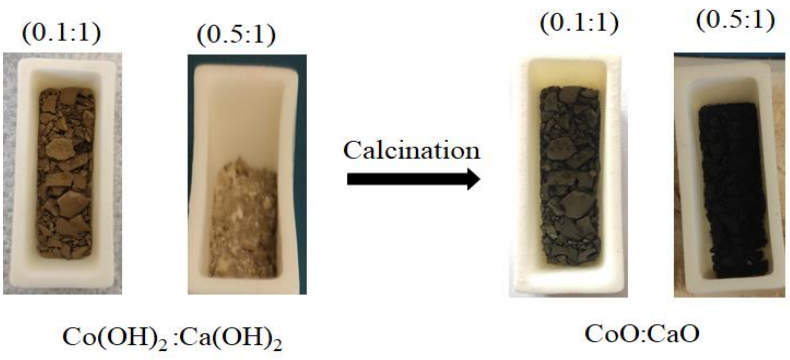

(a)

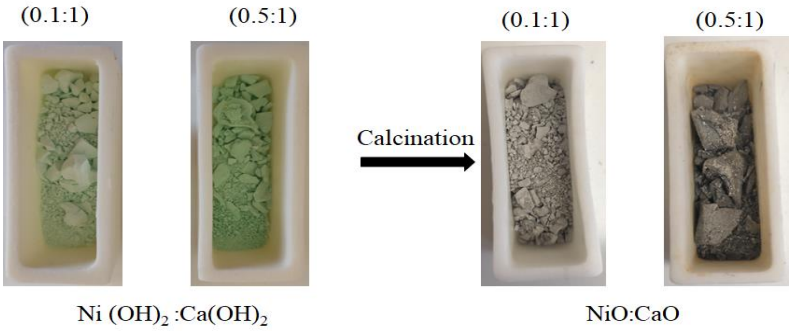

(b)

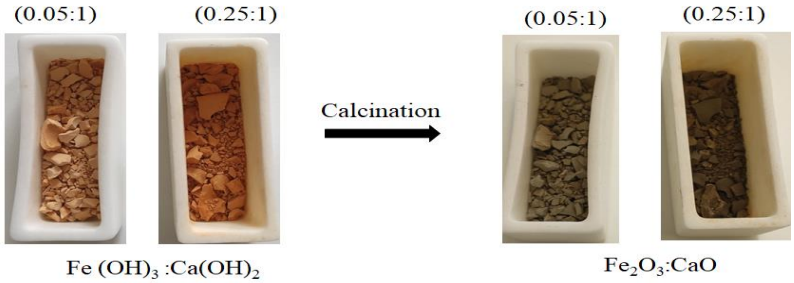

(c)

Figure 4.3: The precursor of metal oxides doped to CaO prepared from 0.1:1 and 0.5:1 metal chlorides to $CaCl_2$ (a) $zCo(OH)_2$:$Ca(OH)_2$ to zCoO:CaO (b) $zNi(OH)_2$:$Ca(OH)_2$ to zNiO:CaO (c) $zFe(OH)_3$:$Ca(OH)_2$ to zFe_2O_3:CaO

There are two different calcination conditions: wet precipitates calcined in air and dried precipitates calcined in air. Part of the wet precipitates was used to measure the crystallite size and quantitative value of the phases of the samples. During the heating process in the range of 25-650 ºC, the samples were analyzed by XRD at each 50 ºC.

All the precursors collected from dry precipitate were calcined at 650 ºC for one hour in the furnace with a heating rate of 15 °C/min in air.

As a result, 0.1CoO:CaO, 0.5CoO:CaO, 0.1NiO:CaO, 0.5NiO:CaO and $0.05Fe_2O_3$:CaO, $0.25Fe_2O_3$:CaO powder were produced. H_2O was evaporated by dissociation, as shown in the following equations:

Case I: if x = even (2, 4, 6 ….)

$$zM(OH)_x{:}Ca(OH)_{x(s)} \rightarrow zMO_{\frac{x}{2}}{:}CaO_{(s)} + (\frac{zx}{2} + 1)H_2O \uparrow \quad \text{Eq 4.3-3}$$

Case II: if x = odd (1, 3, 5 ….)

$$zM(OH)_x{:}Ca(OH)_{x(s)} \rightarrow \frac{z}{2}M_2O_x{:}CaO_{(s)} + (\frac{zx}{2} + 1)H_2O \uparrow \quad \text{Eq 4.3-4}$$

4.4 The absorption capacity of pure CaO and metal oxides doped CaO nanoparticles

In this section, the absorption capacity for CO_2 capturing of pure CaO and metal oxides doped CaO (CoO:CaO, NiO:CaO, Fe_2O_3:CaO) was described. The list of samples is shown in the following Table 4.4.

Table 4.4. The samples were kept at different temperatures for the absorption process

Temperatures ºC	Samples			
	CaO	CoO:CaO	NiO:CaO	Fe_2O_3:CaO
0	CaO	0.1CoO:CaO 0.5CoO:CaO	0.1NiO:CaO 0.5NiO:CaO	$0.05Fe_2O_3$:CaO $0.25Fe_2O_3$:CaO
25	CaO	0.1CoO:CaO 0.5CoO:CaO	0.1NiO:CaO 0.5NiO:CaO	$0.05Fe_2O_3$:CaO $0.25Fe_2O_3$:CaO
50	CaO	0.1CoO:CaO 0.5CoO:CaO	0.1NiO:CaO 0.5NiO:CaO	$0.05Fe_2O_3$:CaO $0.25Fe_2O_3$:CaO
75	CaO	0.1CoO:CaO 0.5CoO:CaO	0.1NiO:CaO 0.5NiO:CaO	$0.05Fe_2O_3$:CaO $0.25Fe_2O_3$:CaO
100	CaO	0.1CoO:CaO 0.5CoO:CaO	0.1NiO:CaO 0.5NiO:CaO	$0.05Fe_2O_3$:CaO $0.25Fe_2O_3$:CaO
200	CaO	0.1CoO:CaO 0.5CoO:CaO	0.1NiO:CaO 0.5NiO:CaO	$0.05Fe_2O_3$:CaO $0.25Fe_2O_3$:CaO

In the process, the produced samples (after the calcination of the samples) were kept at each temperature 0, 25, 50, 75, 100, 200 ºC for 3-6 weeks. The mass increasing for each sample has been measured every day until the mass becomes maximum while the samples are saturated after capturing.

4.5 Characterization techniques

XRD investigations were performed using two instruments, both with Cu K-alpha source, 40 kV and 40 mA generator settings, parallel beam with a Göbel mirror. The obtained powder calcined in air was measured (instrument 1) on Bruker D8 Advance (Vantec-1 PSD with 1° opening, scanning rate 0.007 °(2Th)/24 sec. The wet precipitate was in-situ calcined between 25-650 ºC, recording at each 50 ºC, in an Anton Paar HTK 1200N heating under vacuum and in air inside the chamber with 60 °C/min heating rate, 0.01 mbar when vacuum applied mounted (instrument 2) on Bruker D8 Discover Lynx Eye XE-T solid-state ED detector in 0 D mode, scanning rate 0.014 °(2Th)/24 sec as seen in Figure 4.5-1. XRD analysis was done to investigate the crystallite size based on the Scherrer's equation of the detected samples.

$$D = \frac{k\lambda}{\beta \mathrm{Cos}\theta}$$

Where D = crystallite sizes (nm), k = 0.9 (Scherrer constant), λ= 0.154 nm (wavelength of the X-ray source), β = FWHM (full width at half maximum, radians), θ= peak position (radians).

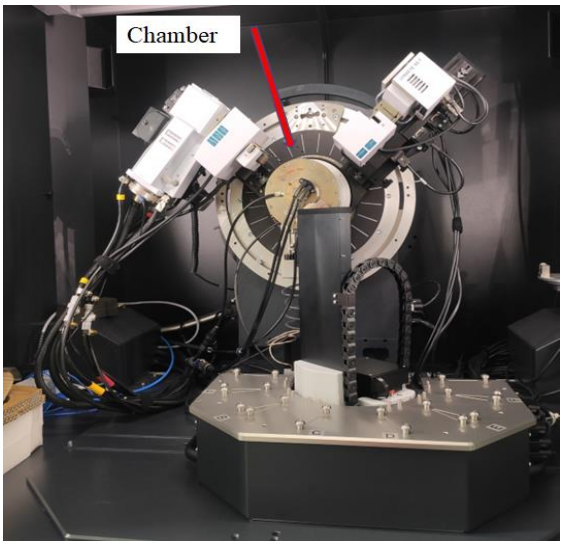

Figure 4.5-1: XRD instrument 2 with chamber to analysis sample during the calcination process under vacuum and in air

For the capturing process, the samples from dry precipitate were calcined in air for one hour using the furnace with a heating rate of 15 °C/ as seen in Figure 4.5-2 a. The measurements of the CO_2 capturing process in air were done in the low-temperature furnace used as an oven, as seen in Figure 4.5.2-b.

(a) (b)

Figure 4.5-2: Furnaces (a) calcined samples in air (b) low-temperature furnace used as an oven for long period to measure the CO_2 capturing efficiency

The SEM and EDS investigations are performed at a magnification of 5000x at 20 kV accelerating voltage (ThermoFisher Helios G4 PFIB SEM equipped with an EDAX Octane ElectPlus EDS), as seen in Figure 4.5-3. In addition to energy dispersive X-ray spectroscopy, a transmission electron microscope (TEM) was applied during SEM investigations.

SEM investigations of the samples, the average particle sizes were measured via "image J" software using the mode of threshold adjustment to analyze particles. The result of the particle sizes shows the particles (agglomerated crystallite). The result is automatically detected by threshold frequency mode on the captured SEM micrographs. It shows the average value of the detected particles. EDS investigations were done during the investigations of SEM. It reveals the existence of gold Au and carbon C; those are from the sample preparations. The powder sample was set on the carbon layer and the gold coating was applied to the powder sample before investigations of SEM and EDS.

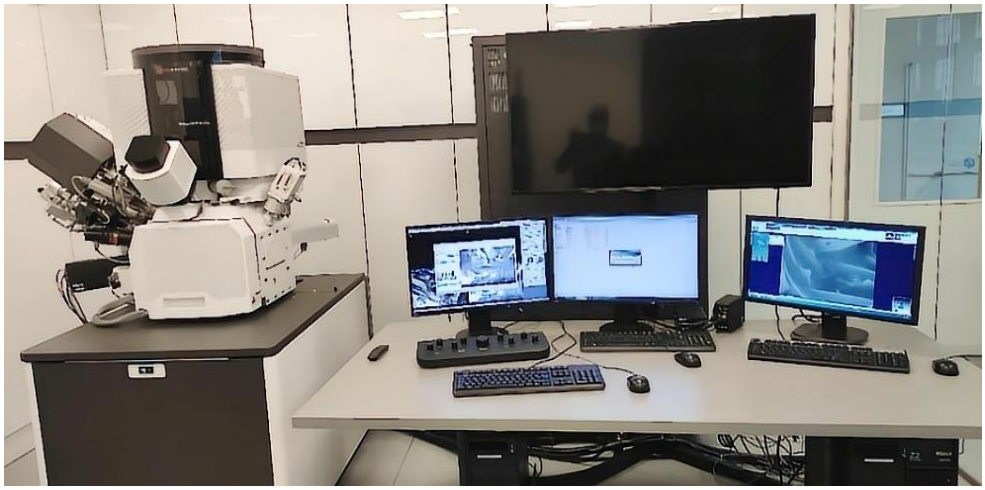

Figure 4.5-3: SEM and EDS instruments to investigate the morphology and the particles sizes

TEM measurements were done by Fei Tecnai G2 20 XTwin equipment with a tungsten cathode and an acceleration voltage of 200 kV. The bright field images were recorded by FEI Eagle 2k CCD camera, as seen in Figure 4.5-4. TEM has a higher magnification than SEM; it shows the morphology, crystallite size and crystal structure of the sample on nanoscale.

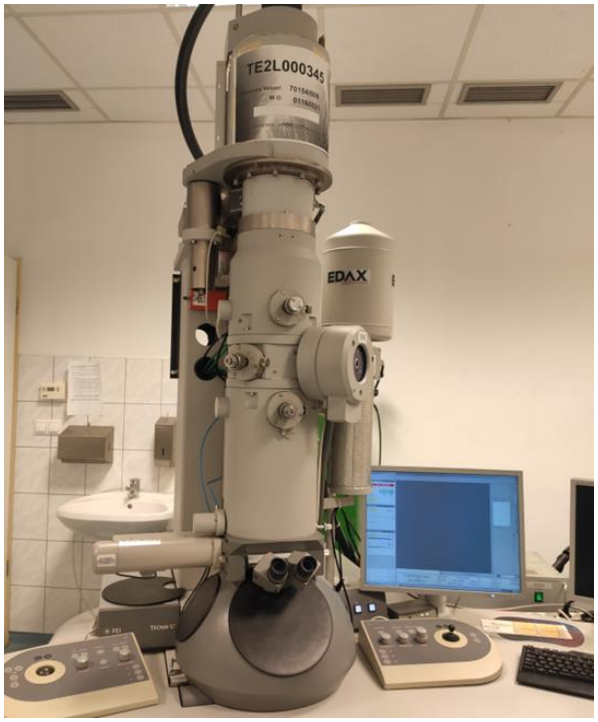

Figure 4.5-4: TEM instrument to investigate the crystallite size

Figure 5.4-5 shows the instrument for BET analysis that was performed under N_2 environment under atmospheric pressure. The following mode was used: TriStar 3000, Unit 1, Serial 1109, sample density 1 g/cm^3, 10-second interval, warm free space 7.37 cm^3, cold free space 22.55 cm^3, analysis bath 77.3 K. BET analysis is an analytical technique utilized for determining specific surface areas and pore size distributions of solid materials. BET is a method for estimating the specific surface area of a non-porous solid. BJH (BJH the method of Barrett, Joyner, and Halenda) is a method to determine the pore size distribution of a mesoporous solid.

Figure 4.5-5: BET instrument to investigate the specific surface areas and pores diameter

5. Results and Discussion

5.1 Synthesis of metal oxides nanoparticles by precipitation-calcination method

XRD analysis confirmed that pure CaO powder with 80 nm of crystallite size is detected, as seen in Figure 5.1-1, which has a cubic crystalline lattice system. XRD diffractograms show only the existence of Co_3O_4 i.e; CoO transformed into Co_3O_4 in the oxidizing environment. CoO phase is only at high temperatures, which transformed into Co_3O_4 when it was cooled down, which is a stable phase. The crystallite size of Co_3O_4 is 17 nm, as seen in Figure 5.1-2 and it has a hexagonal crystallite lattice system. Figure 5.1-3 shows Fe_2O_3 (hematite) with 16 nm of crystallite size. Figure 5.1-4 shows XRD diffractogram of NiO with 30 nm of the crystallite size. Moreover, the other researchers produced CuO and ZnO through the same routes using metal chloride and NaOH with the crystallite size in sub-micro and nanoscale. Furthermore, BeO, NiO, MgO, and SnO have been produced using metal chlorides and NaOH through different routes seen in Table 2.1.

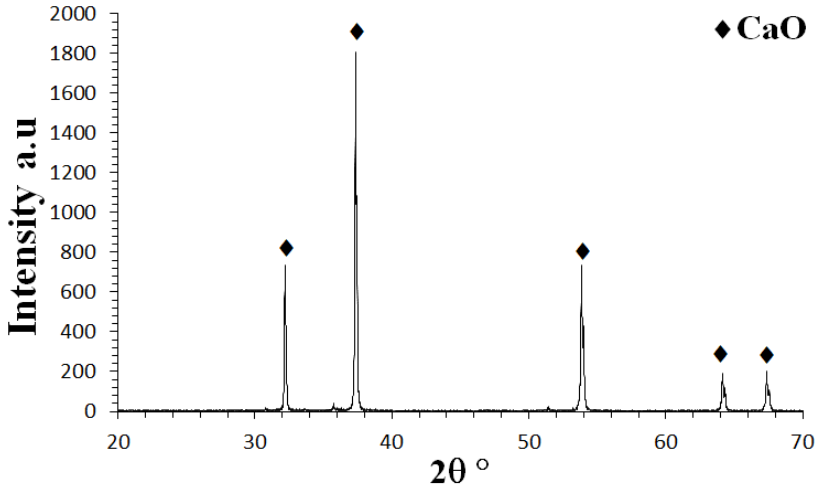

Figure 5.1-1: XRD diffractogram of CaO from dry precipitate $Ca(OH)_2$ calcined at 650 °C for one hour in air

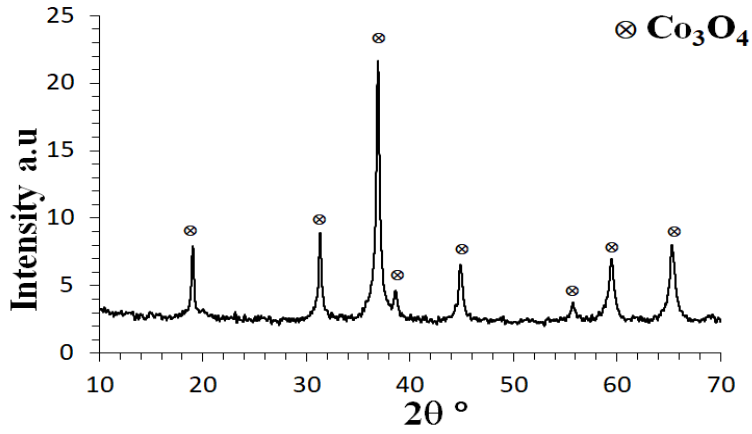

Figure 5.1-2: XRD diffractogram of Co_3O_4 from dry precipitate $Co(OH)_2$ calcined at 170 °C for one hour in air

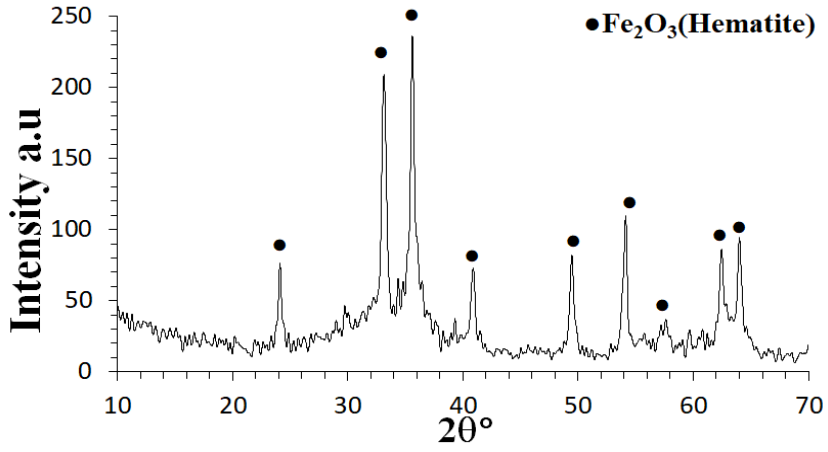

Figure 5.1-3: XRD diffractogram of Fe_2O_3 from dry precipitate $Fe(OH)_3$ calcined at 450 °C for one hour in air

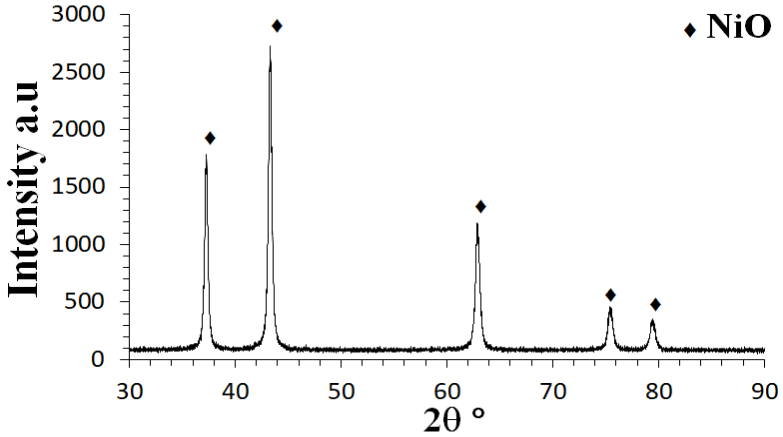

Figure 5.1-4: XRD diffractogram of NiO from dry precipitate $Ni(OH)_2$ calcined at 600 °C for one hour in air

TEM micrographs of the metal oxides are described in Figure 5.1-5. The result of the TEM micrographs agrees with the crystallite size taken from the XRD result. SEM micrographs and the EDS spectra of the metal oxide nanoparticles CaO, CoO/Co_3O_4 and NiO are shown in Figure 5.1-6. The particles (agglomerated crystallite) of TEM result have the similar result of SEM micrographs.

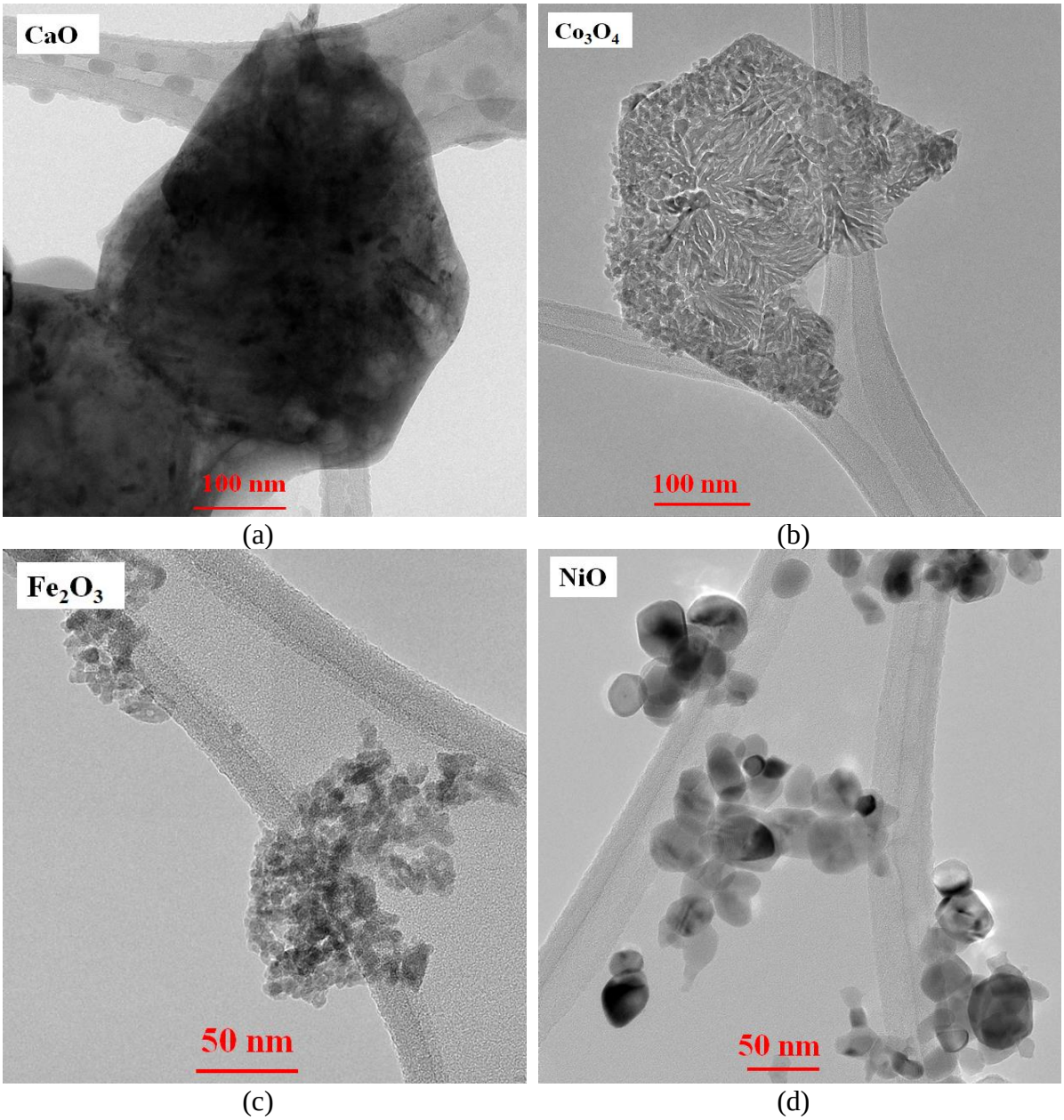

Figure 5.1-5: TEM micrographs of (a) CaO (b) CoO/Co_3O_4 (c) Fe_2O_3 and (d) NiO

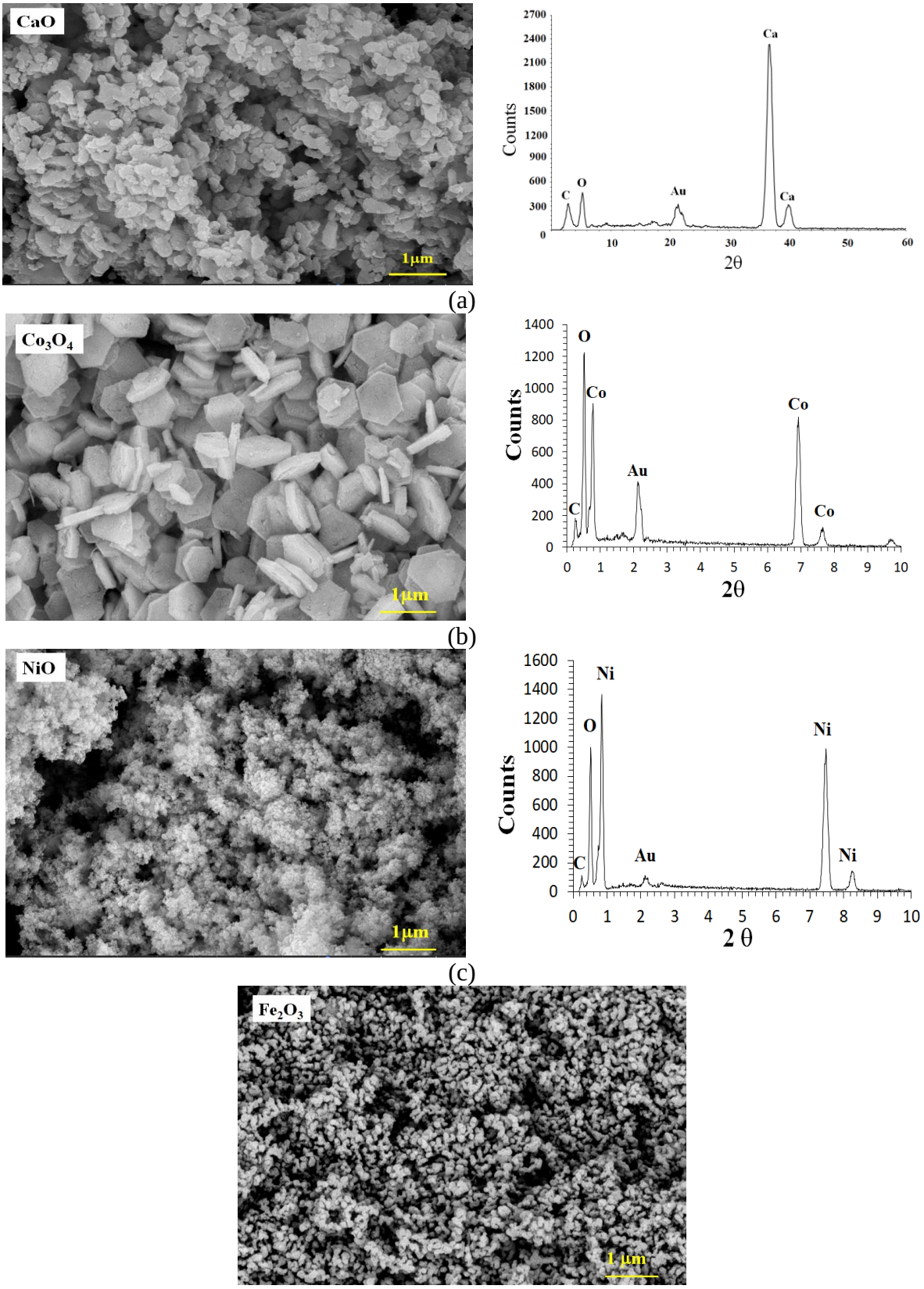

Figure 5.1-6: SEM micrographs and EDS spectra of (a) CaO (b) CoO/Co_3O_4 and (c) NiO (d) Fe_2O_3

5.2 Characterization methods of CaO nanoparticles produced by precipitation-calcination method

TEM micrographs of samples are shown as both single crystallite with high magnifications (low nanoscale) and agglomerated crystallite with low magnifications (high nanoscale). Single crystallite from TEM micrographs confirms the result of the crystallite size by XRD. The agglomerated crystallite from TEM micrographs confirms the result of the particle size (agglomerated crystallite) from SEM micrographs.

5.2.1 Crystallite sizes of CaO nanoparticles.

The wet precipitates $Ca(OH)_2$ were calcined under vacuum and in air at the temperature range of 25 - 650 °C in the chamber of the XRD instrument 2. Figure 5.2-1 shows a series of XRD diffractograms of sample 1(calcination under vacuum). Figure 5.2-2 shows a series of XRD diffractograms of sample 2(calcination in air). Note that the preparations of CaO samples 1 and 2 are shown in section 4.2.1. The calcination process of sample 1 under vacuum showed that the initial wet precipitate at 25 ºC contains mostly $Ca(OH)_2$ with very few amounts of $CaCO_3$. The peaks $Ca(OH)_2$ disappeared in the temperature range between 250 and 300 ºC while a new peak of CaO appeared. The small peak of $CaCO_3$ disappeared in the temperature range between 500 and 550 ºC. Similar results of sample 2 (calcination in air) are shown in Figure 5.2-2. In this case, the in-situ calcination in the XRD equipment was performed in air. To compare Figure 5.2-2, sample 2 calcination in air (instead of vacuum) leads to prolonged stability by about 150 ºC. For both initial compounds, $Ca(OH)_2$ transformed to CaO from 300 ºC calcination under vacuum and 450 ºC calcination in air. The peak of $CaCO_3$ disappeared from the samples calcined at 500 ºC under vacuum and from samples calcined at 650 ºC in air; that is shown in Figure 5.2-1 and 5.2-2, Table 5.2-1. This is due to the high entropy of the gaseous reaction products (H_2O and CO_2) that drive the dissociation reaction in a vacuum further and faster compared to the case when calcination is performed in air.

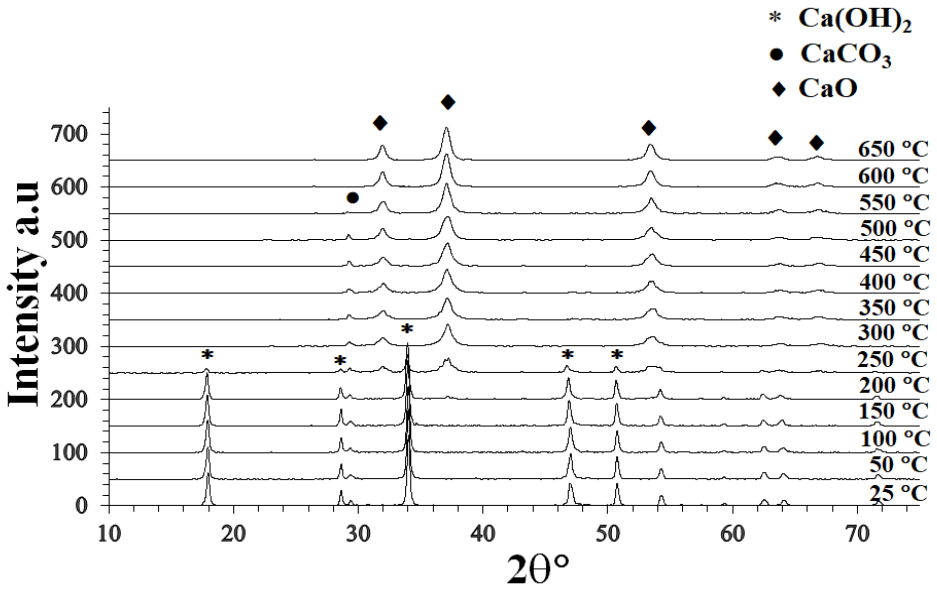

Figure 5.2-1: The XRD diffractograms of sample 1 CaO during its calcination steps under vacuum in the temperature interval of 25 - 650 ºC

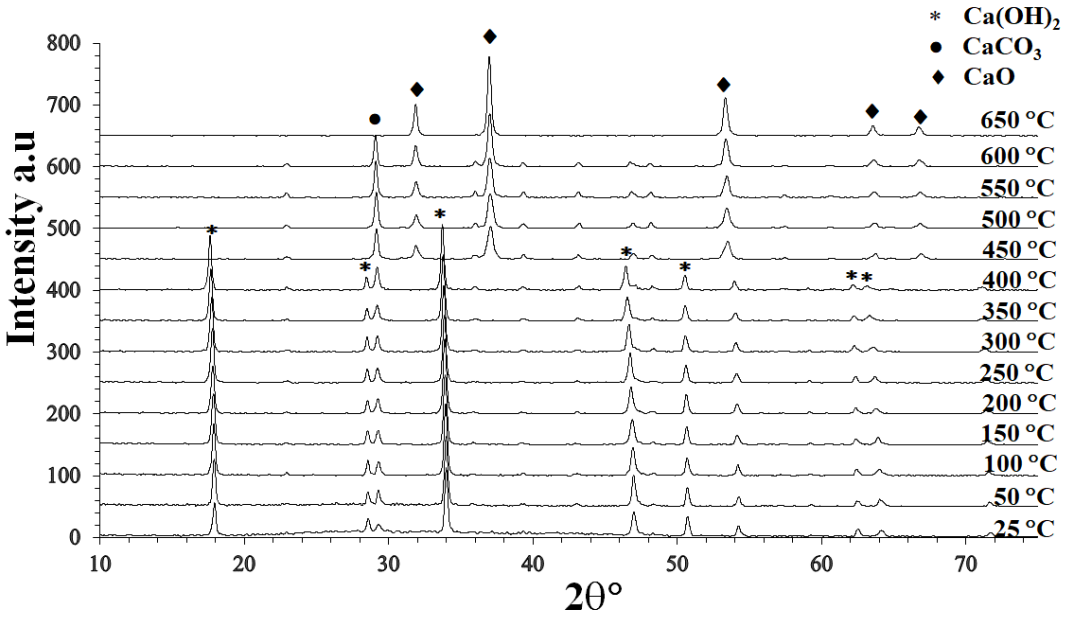

Figure 5.2-2: The XRD diffractograms of sample 2 CaO during its calcination steps under air in the temperature interval of 25 - 650 ºC

Based on the series of XRD graphs, the phases of CaO nanocrystalline powder were mentioned upon the temperature and the calcination environment, as seen in Table 5.2.1.

Table 5.2.1: Phases formed from wet precipitate $Ca(OH)_2$ during its calcination at different temperatures to CaO

Phases	In vacuum (Fig. 5.2-1) Sample 1	In air (Fig. 5.2-2) Sample 2
$Ca(OH)_2 + CaCO_3$	25 - 150 ºC	25 - 400 ºC
$Ca(OH)_2 + CaCO_3 + CaO$	200 - 250 ºC	-
$CaCO_3 + CaO$	300 - 550 ºC	450 - 600 ºC
CaO	600 - 650 ºC	650 ºC

Figure 5.2-3 shows the temperature dependence of the crystallite sizes with a deviation of CaO obtained by calcination under vacuum sample 1 and calcination in air sample 2 using the XRD technique. The crystallite sizes of CaO calcined under vacuum go through a maximum at 550 ºC. Around this temperature, the CaO particles undergo recrystallization by eliminating lattice defects and dislocations. However, this maximum is not present for the case when CaO was obtained by calcination in air. The final crystallite size of CaO calcined under vacuum is about 140 nm and the final crystallite size of CaO calcined in air is about 80 nm.

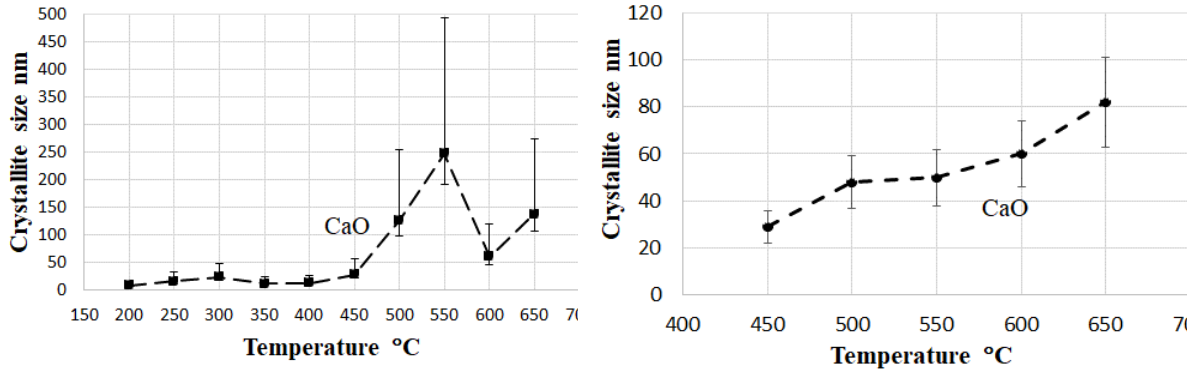

(a) (b)

Figure 5.2-3: The crystallite sizes of CaO (a) Sample 1 calcination under vacuum (b) Sample 2 calcination in air as a function of temperature

5.2.2 SEM, EDS and TEM characterization of CaO nanoparticles

TEM micrographs in Figure 5.2-4 confirms that the particle sizes of the produced CaO samples are in the nano size. Figure 5.2-5 shows the SEM micrograph and EDS spectrum of CaO. Agglomerated crystallite of CaO regarding the TEM micrographs in Figure 5.2-4 b revealed similar results to the SEM micrographs in this research work.

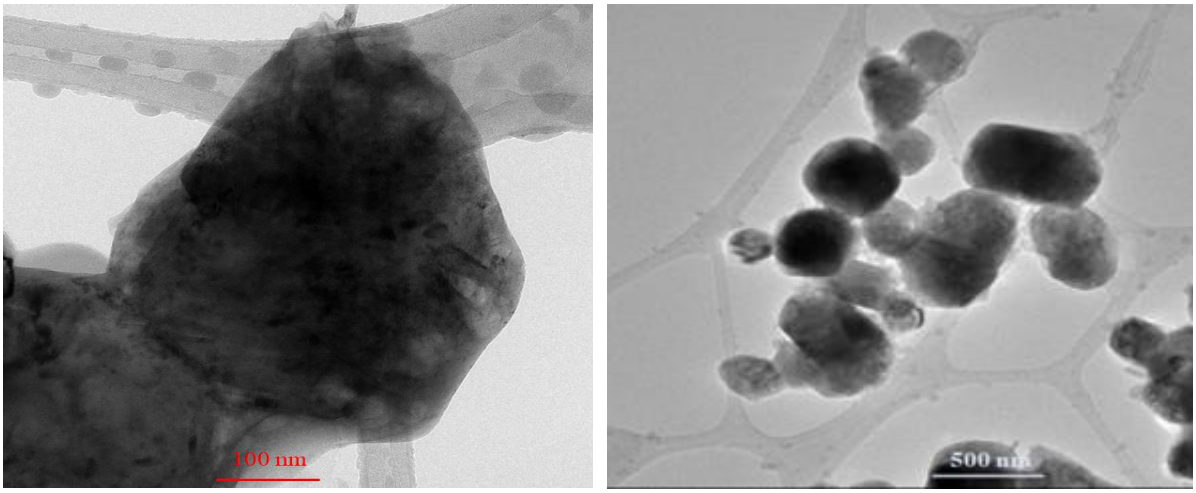

(a) (b)

Figure 5.2-4: TEM micrographs of CaO produced from dry precipitate $Ca(OH)_2$ calcined in air (a) single crystallite (b) agglomerated crystallite (particle)

Regarding SEM micrographs of pure CaO samples revealed that the average particle size was found in the range of 105 – 255 nm. The morphology of the CaO is flake shape and fluffy structure. The EDS investigation confirmed the presence of Ca and O (a small amount of C is from the sample holder), as seen in Figure 5.2-5.

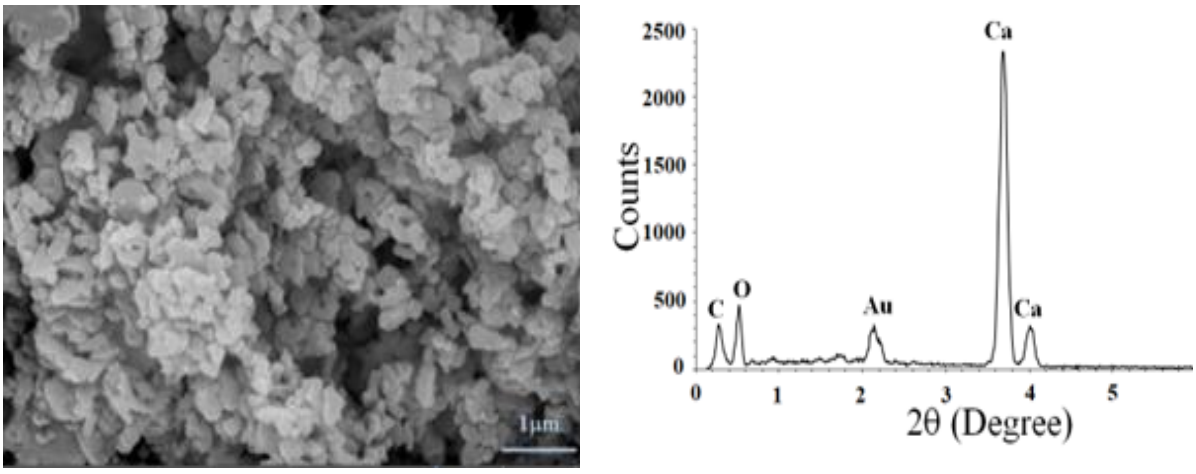

(a) (b)

Figure 5.2-5: (a) SEM micrographs and (b) EDS spectra of CaO nanoparticles. The peak for gold in the Figure corresponds to the coating added during sample preparation.

Table 5.2.2 shows the BET analysis of a pure CaO sample (obtained by calcination in air at 650 ºC for 1 h) which has 4.34 m^2g^{-1} of specific surface area. The absorption and desorption surface area of the pore for pure CaO sample is 3.05 m^2g^{-1}. The absorption average pore diameter is 11 nm.

Table 5.2.2: The specific surface area of CaO sample calcined in air at 650 ºC for 1 hour

Sample	Specific surface area (BET) m^2g^{-1}	Surface area of pore (BJH)		Cumulative pore volume of pore (BJH)		Absorption average pore diameter
		Absorption m^2g^{-1}	Desorption m^2g^{-1}	Absorption $cm^3\ g^{-1}$	Desorption m^2g^{-1}	(BET) nm
CaO	4.34	3.05	3.2	0.016	0.016	11

5.3: Characterization of metal oxides doped CaO nanoparticles

In this section, XRD, SEM, EDS and TEM analysis of three different metal oxides (CoO, NiO and Fe_2O_3) doped CaO are described. Each doping sample was prepared based on the ratio 0.1: 1 and 0.5:1 of MCl_x to $CaCl_2$ during the reactions.

5.3.1 XRD result of low doped CaO.

In this section, the analysis of the crystallite size and the function upon the temperature of pure CaO sample and metal oxides low doped CaO (0.1CoO:CaO, 0.1NiO:CaO and 0.05Fe_2O_3:CaO) were done by XRD method. The crystallite size analysis for all doped samples was done from the wet precursors. The wet precipitate of $Co(OH)_2$:$Ca(OH)_2$, $Ni(OH)_2$:$Ca(OH)_2$ and $Fe(OH)_3$:$Ca(OH)_2$ were calcined in air at the temperature range of 25 - 650 °C in the chamber of XRD instrument 2. At the same time, the samples were measured by XRD at each 50 °C in the series.

5.3.1.1 XRD result of 0.1CoO:CaO sample

The XRD result of the 0.1CoO:CaO sample produced by wet precipitate $Co(OH)_2$:$Ca(OH)_2$ calcined in air is shown in Figure 5.3-1. XRD diffractogram reveals the existence of $Ca(OH)_2$, $Co(OH)_2$ and very few amounts of $CaCO_3$ at 25 ºC. $Co(OH)_2$ exists between 25 - 200 ºC. $Ca(OH)_2$ started to transform to CaO at 450 ºC while the peaks of $CaCO_3$ are still remaining. At the temperature between 500-550 ºC, the formation of $Ca_2Co_2O_5$ was found. At 650 ºC, the peak of $CaCO_3$ disappeared and the sample was completely calcined with the existence of CaO and $Ca_2Co_2O_5$.

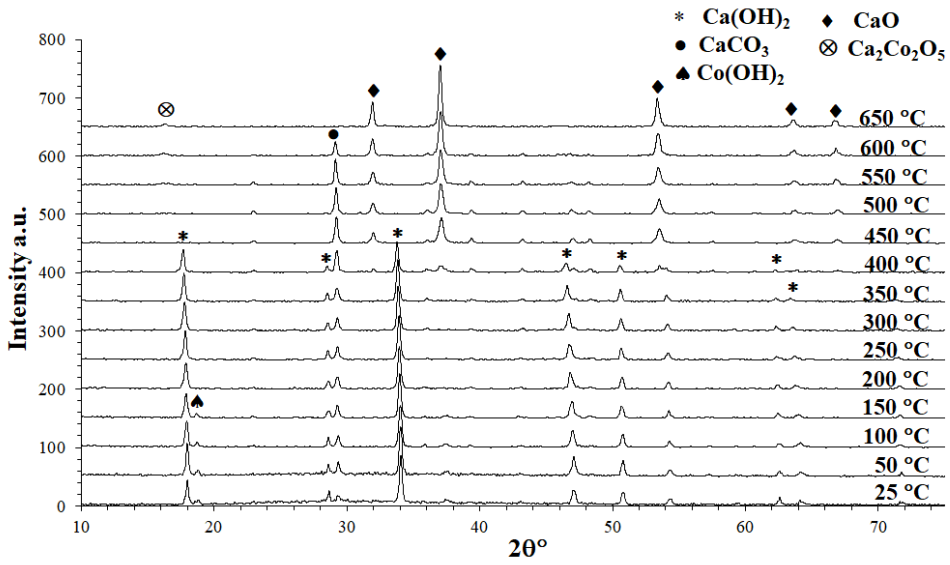

Figure 5.3-1: The XRD diffractogram of 0.1CoO:CaO prepared from 0.1:1 mole ratio of $CoCl_2$ to $CaCl_2$ by wet precipitate $Co(OH)_2$:$Ca(OH)_2$ calcined in air between 25-650 ºC measured at each 50 ºC

5.3.1.2 XRD result of 0.1NiO:CaO sample

Figure 5.3-2 shows the XRD result of 0.1NiO:CaO produced by wet precipitate $Ni(OH)_2$:$Ca(OH)_2$ calcined in air. At 25 ºC, the existence of $Ca(OH)_2$ and very few amounts of $CaCO_3$ have been detected. At 450 ºC, $Ca(OH)_2$ completely transformed to CaO while the $CaCO_3$ is still remaining until 600 ºC. At 650 ºC, the sample contains only CaO and NiO without the peak of $CaCO_3$. Therefore, the complete calcination temperature of 0.1NiO:CaO was found to be 650 ºC.

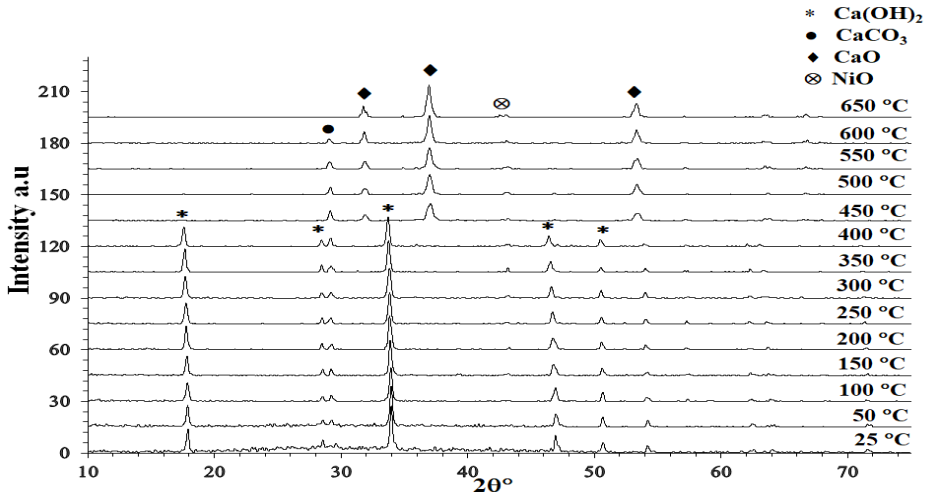

Figure 5.3-2: The XRD diffractogram of 0.1NiO:CaO prepared from 0.1:1 mole ratio of $NiCl_2$ to $CaCl_2$ by wet precipitate $Ni(OH)_2$:$Ca(OH)_2$ calcination in air between 25-650 ºC measured at each 50 ºC

5.3.1.3 XRD result of 0.05Fe_2O_3:CaO sample

The XRD result of 0.05Fe_2O_3:CaO sample produced by wet precipitate $Fe(OH)_3$:$Ca(OH)_2$ calcination in air is shown in Figure 5.3-3. Between 25 - 300 ºC, the existence of $Ca(OH)_2$ with very few amounts of $CaCO_3$ have been detected. At 350 ºC, a new peak of $Ca_2Fe_2O_5$ appeared. The peak of Fe_2O_3 also occurred at 400 ºC. $Ca(OH)_2$ completely transformed into CaO at 450 ºC while $CaCO_3$ still remain in the sample. The peak of $CaCO_3$ disappeared between 600-650 ºC and only the existence of CaO, Fe_2O_3 and $Ca_2Fe_2O_5$ have been detected. Therefore, 650 ºC is required to complete the calcination process.

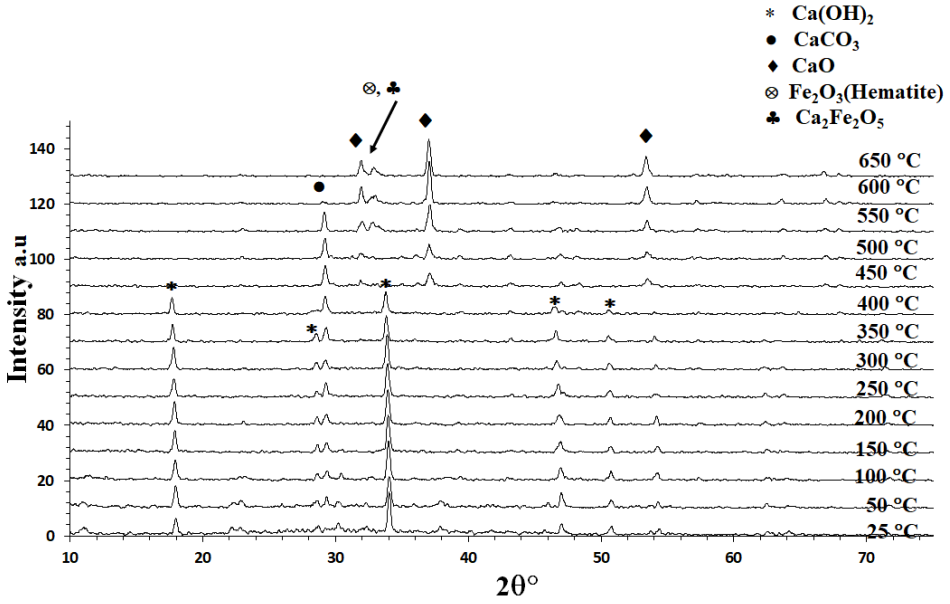

Figure 5.3-3: The XRD diffractogram of 0.05Fe_2O_3:CaO prepared from 0.1:1 mole ratio of $FeCl_3$ to $CaCl_2$ by wet precipitate $Fe(OH)_3$:$Ca(OH)_2$ calcination in air between 25-650 ºC measured at each 50 ºC

5.3.1.4 Crystallite size of low-doped CaO.

In 0.1CoO:CaO sample, CaO and $Ca_2Co_2O_5$ phases were found to be with crystallite sizes of 105 and 50 nm, as shown in Figure 5.3-4 a. For 0.1NiO:CaO sample, the CaO and NiO phases were detected with crystallite sizes less than 50 nm, as shown in Figure 5.3-4 b. CaO, Fe_2O_3 and $Ca_2Fe_2O_5$ phases were detected in 0.05Fe_2O_3:CaO samples with the crystallite size of 165, 808, 14 nm, respectively, as seen in Figure 5.3-4 c. The crystallite sizes are described at 650 ºC and that temperature is required to complete the calcination process for all low-doped CaO samples.

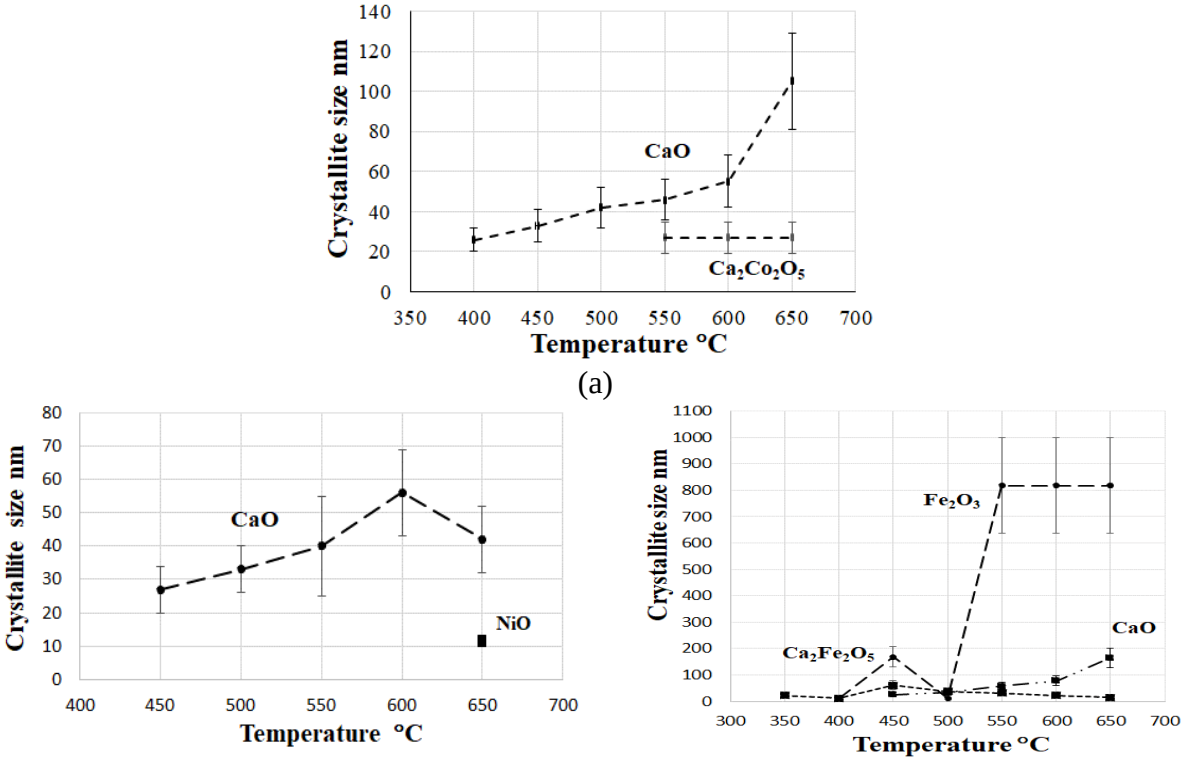

Figure 5.3-4: The crystallite sizes of (a) 0.1CoO:CaO (b) 0.1NiO:CaO and (c) 0.05Fe_2O_3:CaO prepared from 0.1:1 mole ratio of MCl_x to $CaCl_2$ by wet precipitate calcination in air between 25-650 ºC measured at each 50 ºC

Based on the series of XRD diffractograms in Figure 5.3-1 – 5.3-3, the formations of phases for the sample 0.1CoO:CaO, 0.1NiO:CaO and 0.05Fe_2O_3:CaO were mentioned upon the temperature as seen in Tables 5.3.1 – 5.3.3. Moreover, the quantitative value (the amount percentage of the detected phases) of the samples at each temperature are also mentioned in Tables 5.3.4 – 5.3.6.

Table 5.3.1: Phases formed from wet precipitate $Co(OH)_2$:$Ca(OH)_2$ during its calcination at different temperatures to 0.1CoO:CaO

Temperature ºC	Phases from Figure 5.3-1
25-150	$Ca(OH)_2 + Co(OH)_2 + CaCO_3$
200 -350	$Ca(OH)_2 + CaCO_3$
400	$Ca(OH)_2 + CaCO_3 + CaO$
450-500	$CaCO_3 + CaO$
550 -600	$CaCO_3 + CaO + Ca_2Co_5O_5$
650	$CaO + Ca_2Co_5O_5$

Table 5.3.2: Phases formed from wet precipitate $Ni(OH)_2$:$Ca(OH)_2$ during its calcination at different temperatures to 0.1NiO:CaO

Temperature ºC	Phases from Figure 5.3-2
25- 400	$Ca(OH)_2 + CaCO_3$
450-600	$CaCO_3 + CaO$
650	CaO + NiO

Table 5.3.3: Phases formed from wet precipitate $Fe(OH)_3$:$Ca(OH)_2$ during its calcination at different temperatures to 0.05Fe_2O_3:CaO

Temperature ºC	Phases from Figure 5.3-3
25	$Ca(OH)_2$
50-300	$Ca(OH)_2 + CaCO_3$
350	$Ca(OH)_2 + CaCO_3 + Ca_2Fe_2O_5$
400	$Ca(OH)_2 + CaCO_3 + Ca_2Fe_2O_5 + Fe_2O_3$
450-600	$CaCO_3 + CaO + Ca_2Fe_2O_5 + Fe_2O_3$
650	$CaO + Ca_2Co_5O_5$

Table 5.3.4: The volume percentages of the different phases (%) found by XRD in the 0.1CoO:CaO sample prepared by heating in air as a function of temperature from Figure 5.3-1

Phases of 0.1CoO:CaO sample	Temperature ºC													
	25	50	100	150	200	250	300	350	400	450	500	550	600	650
$Co(OH)_2$	5	5	5	5										
$Ca(OH)_2$	81	83	76	76	76	78	78	65	50					
$CaCO_3$	14	12	19	19	24	22	22	35	38	52	53	42	22	
CaO									12	48	45	56	74	96
Ca_2Co_2O											2	2	4	4

Table 5.3.5: The volume percentages of the different phases (%) found by XRD in the 0.1NiO:CaO sample prepared by heating in air as a function of temperature from Figure 5.3-2

Phases of 0.1NiO:CaO sample	Temperature ºC													
	25	50	100	150	200	250	300	350	400	450	500	550	600	650
$Ca(OH)_2$	95	95	94	83	85	80	82	87	72					
$CaCO_3$	5	5	6	17	15	20	18	13	28	17	20	24	13	
CaO										83	80	76	87	96
NiO														4

Table 5.3.6: The volume percentages of the different phases (%) found by XRD in the $0.05Fe_2O_3$:CaO sample prepared by heating in air as a function of temperature from Figure 5.3-3

Phases of $0.05Fe_2O_3$:CaO sample	Temperature ºC													
	25	50	100	150	200	250	300	350	400	450	500	550	600	650
$Ca(OH)_2$	100	70	65	78	78	74	82	62	37					
$CaCO_3$		30	35	22	22	26	18	22	37	49	49	29	5	
CaO										41	39	44	68	55
Ca_2Fe_2O								16	22	5	10	26	26	42
Fe_2O_3									4	5	2	1	1	3

5.3.2 SEM, EDX and TEM characterization of low doped CaO

SEM and EDS examinations of 0.1CoO:CaO, 0.1NiO:CaO and $0.05Fe_2O_3$:CaO are described in this section which, prepared from 0.1:1 mole ratio of metal chloride MCl_x to $CaCl_2$. All the low-doped samples are prepared from the dried precipitates of $Co(OH)_2$:$Ca(OH)_2$, $Ni(OH)_2$:$Ca(OH)_2$ and $Fe(OH)_3$:$Ca(OH)_2$, which calcined at 650 °C for one hour in air using the furnace with a heating rate of 15 °C/min.

According to the SEM micrographs, 0.1CoO:CaO samples revealed that the average particle sizes are in the range of 108 – 255 nm. 0.1NiO:CaO sample has average particle sizes

in the range of 128 – 255 nm. 0.1CoO:CaO and 0.1NiO:CaO samples have flake shapes and fluffy structures. 0.05Fe_2O_3:CaO sample has an average particle size in the range of 120 – 255 nm and it has mostly flake shape and some sphere shape as well.

The EDS spectra and the elemental composition of the 0.1CoO:CaO sample confirmed the presence of Ca, Co and O. For 0.1NiO:CaO, the presence of Ca, Ni and O were confirmed. For 0.05Fe_2O_3:CaO sample, the presence of Ca, Fe and O were detected. Note that the existence of a small amount of C comes from the sample holder, as seen in Figure 5.3-5.

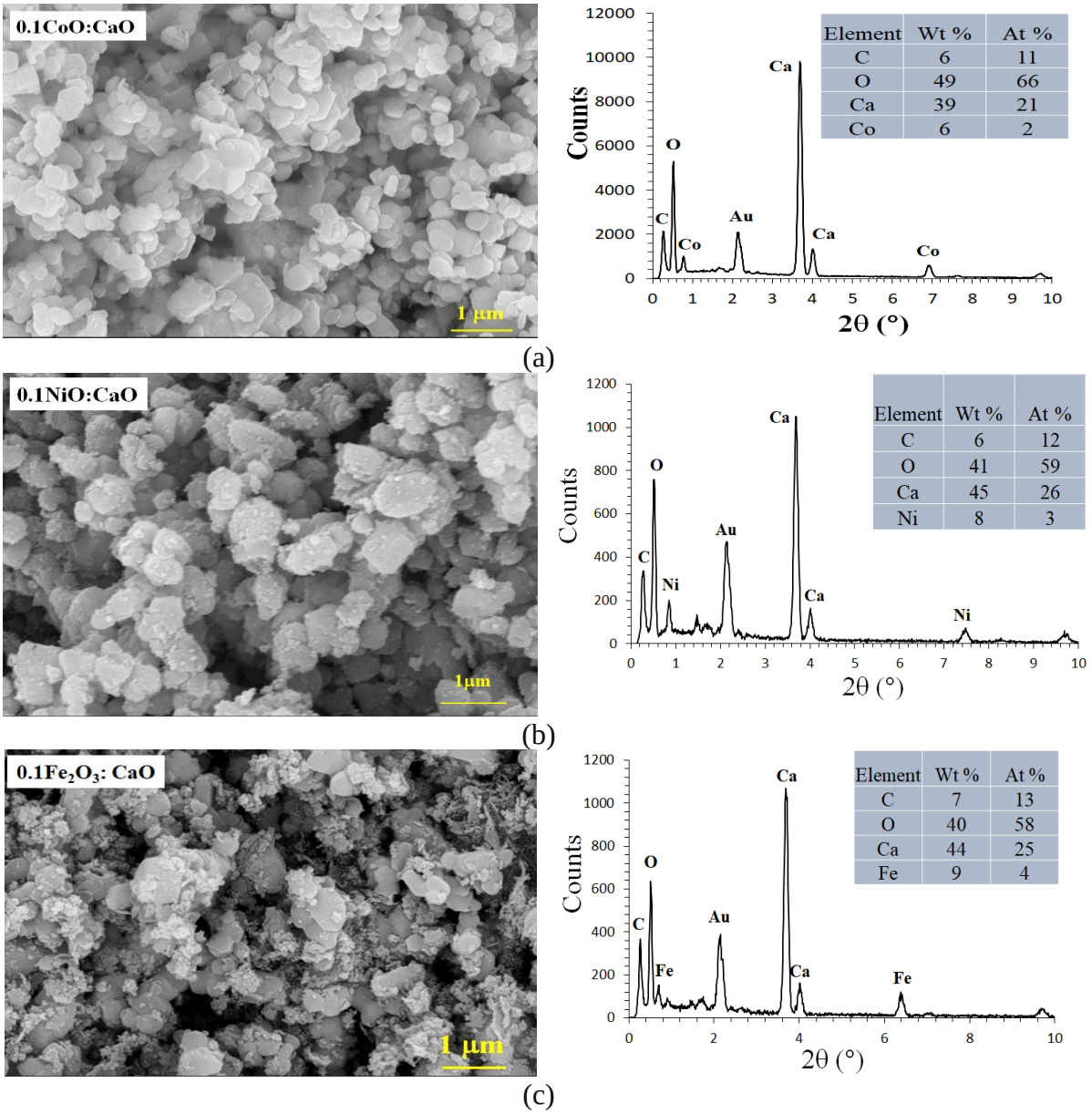

Figure 5.3-5: SEM micrographs (left) showed the morphology of the agglomerated particles and (right) showed the chemical composition of the samples (a) 0.1CoO:CaO (b) 0.1NiO:CaO (c) 0.05Fe_2O_3:CaO

TEM micrographs of the samples 0.1CoO:CaO, 0.1NiO:CaO, 0.05Fe_2O_3:CaO are shown in Figure 5.3-6. The left side of the TEM micrographs is the single crystallite (single primary crystal) of each sample which has similar results to XRD. On the right side of the TEM micrographs are the agglomerated crystallite(particle) of each sample which has similar results to the SEM micrographs.

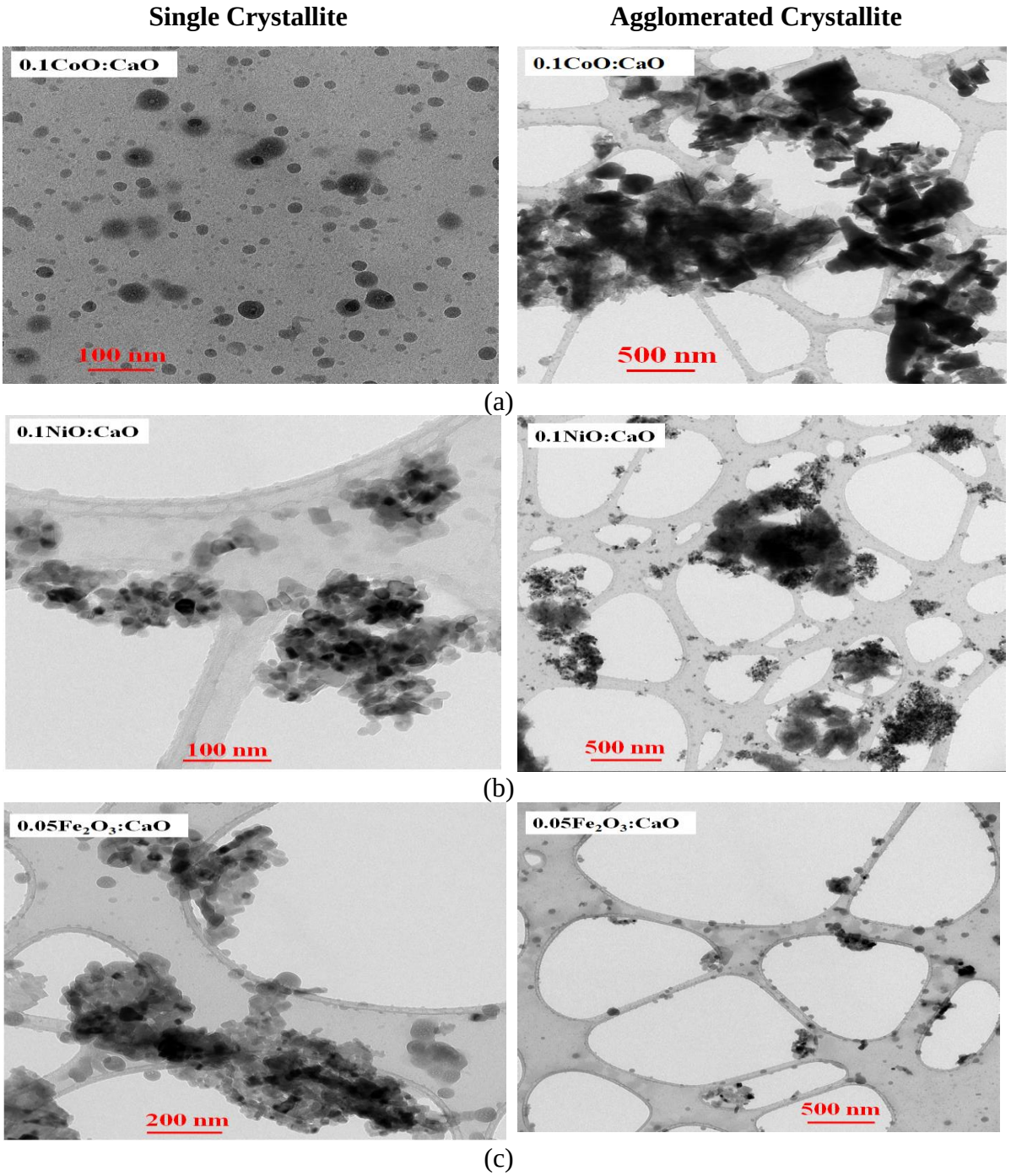

Figure 5.3-6: TEM micrographs(left) showing the single crystallite and (right) showing the agglomerated crystallite (particle) of the samples (a) 0.1CoO:CaO (b) 0.1NiO:CaO (c) 0.05Fe_2O_3:CaO

5.3.3 XRD characterization of highly doped CaO

In this section, the analysis of the crystallite size and the function upon the temperature of metal oxides highly doped CaO (0.5CoO:CaO, 0.5NiO:CaO and 0.25Fe_2O_3:CaO) are described.

5.3.3.1 XRD result of 0.5CoO:CaO sample

Figure 5.3-7 shows the XRD result of the 0.5CoO:CaO sample produced by wet precipitate $Co(OH)_2$:$Ca(OH)_2$ calcined in air. At 25 ºC, the existence of $Ca(OH)_2$, $Co(OH)_2$ and very few amounts of $CaCO_3$ were found. $Co(OH)_2$ exists between 25 and 200 ºC while the peak of Co_3O_4 appeared at 200 ºC. At 300 ºC, $Ca(OH)_2$ and $Co(OH)_2$ start transforming to CaO and CoO. The phase CoO is not stable; it only exists between 300 – 400 ºC. At 500 ºC, a new peak of $CaCo_2O_4$ appeared. The peak of $CaCO_3$ disappeared at 600 ºC. It is proved that the complete calcination temperature is 600 ºC with the formations of CaO, Co_3O_4 and $CaCo_2O_4$ phases. Co_3O_4 exits only at low temperatures and then it reacts with CaO and partially transforms to $CaCo_2O_4$ upon a higher temperature. There is no existence of Co_3O_4 at 650 ºC due to the oxidation and deoxidation reacting with CaO and forming new phases.

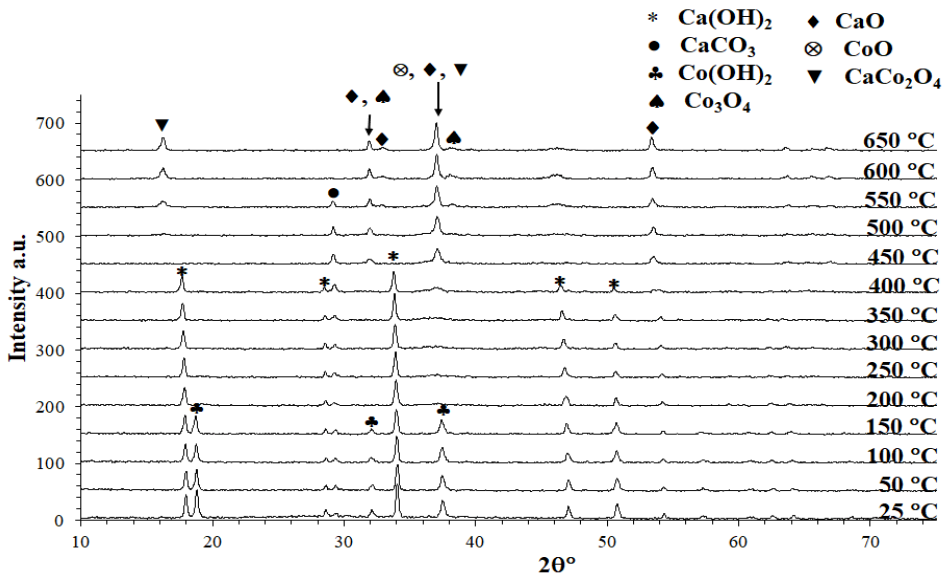

Figure 5.3-7: The XRD diffractogram of 0.5CoO:CaO prepared from 0.5:1 mole ratio of $CoCl_2$ to $CaCl_2$ by wet precipitate $Co(OH)_2$:$Ca(OH)_2$ calcination in air between 25-650 ºC measured at each 50 ºC

5.3.3.2 XRD result of 0.5NiO:CaO sample

Figure 5.3-8 shows the XRD result of the 0.5CoO:CaO sample produced by wet precipitate $Co(OH)_2$:$Ca(OH)_2$ calcined in air. At the temperature range of 25 – 350 ºC, $Ca(OH)_2$ and very few amounts of $CaCO_3$ exist. $Ca(OH)_2$ started to transform to CaO at 400 ºC while a new peak of NiO appeared. At 450 – 600 ºC, there are three phases of CaO, $CaCO_3$ and NiO. The sample was completely calcined at 650 ºC with the existence of CaO and NiO without $CaCO_3$. Therefore, the complete calcination temperature of 0.5NiO:CaO is 650 ºC.

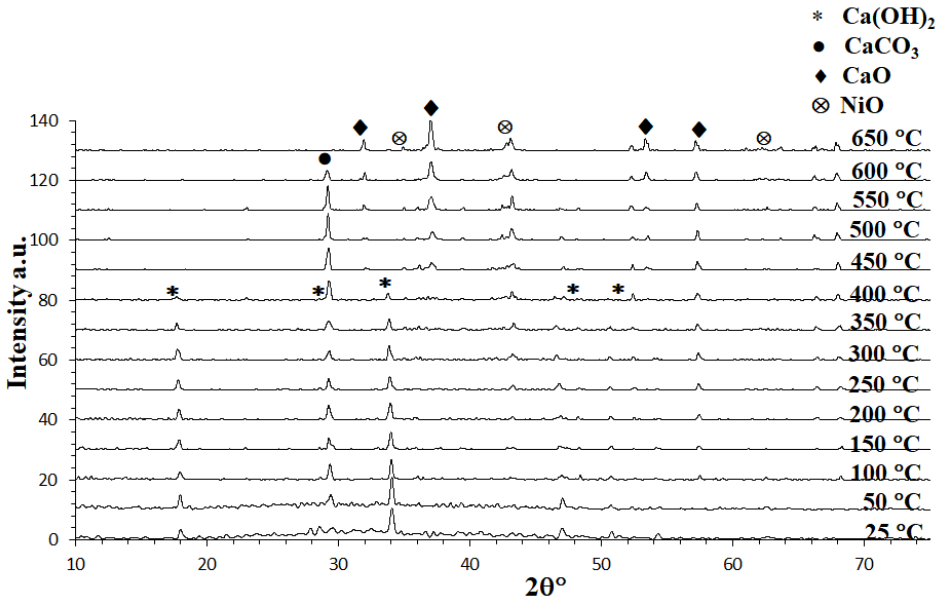

Figure 5.3-8: The XRD diffractogram of 0.5NiO:CaO prepared from 0.5:1 mole ratio $NiCl_2$ to $CaCl_2$ by wet precipitate $Ni(OH)_2$:$Ca(OH)_2$ calcination in air between 25-650 ºC measured at each 50 ºC

5.3.3.3 XRD result of 0.25Fe_2O_3:CaO sample

XRD result of the 0.25Fe_2O_3:CaO sample produced by wet precipitate $Fe(OH)_3$:$Ca(OH)_2$ calcined in air is exhibited in Figure 5.3-9. The existence of $Ca(OH)_2$ and very few amounts of $CaCO_3$ and $Ca_4Fe_2O_6CO_3.12H_2O$ have been detected at the temperature range of 25 – 100 ºC. Between 150 – 300 ºC, the phases of $Ca(OH)_2$ and $CaCO_3$ exist. The new peak of $Ca_2Fe_2O_5$ appeared at 500 ºC. The new peak of CaO appeared at 600 ºC. At 650 ºC, there are only two phases of CaO and $Ca_2Fe_2O_5$ while the peak of $CaCO_3$ disappeared. As a conclusion, the complete calcination temperature of 0.25Fe_2O_3:CaO sample is 650 ºC.

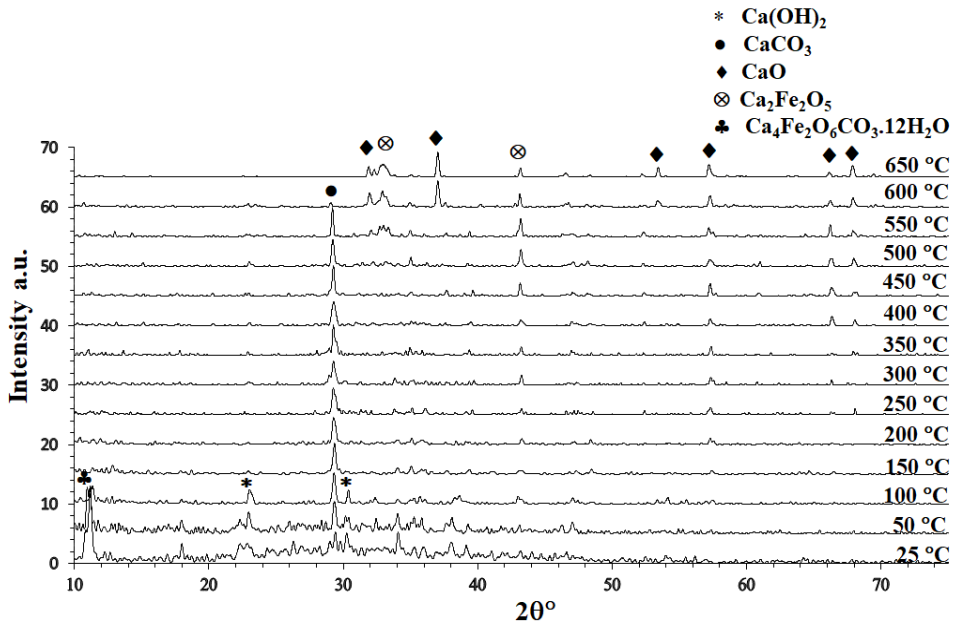

Figure 5.3-9: The XRD diffractogram of $0.25Fe_2O_3$:CaO prepared from 0.5:1 mole ratio of $FeCl_3$ to $CaCl_2$ by wet precipitate $Fe(OH)_3$:$Ca(OH)_2$ calcination in air between 25-650 ºC measured at each 50 ºC

In conclusion, the phases of 0.5CoO:CaO are CaO, CoO and $CaCo_2O_4$ with 180, 20 and 40 nm of crystallite size at 600 ºC as seen in Figure 5.3-10 a. For 0.5NiO:CaO sample, there are CaO and NiO phases with 198 and 45 nm of crystallite size, as seen in Figure 5.3-10 b. For $0.25Fe_2O_3$:CaO sample, CaO and $Ca_2Fe_2O_5$ phases were detected with the crystallite sizes of 818 and 30 nm, as seen in Figure 5.3-10c.

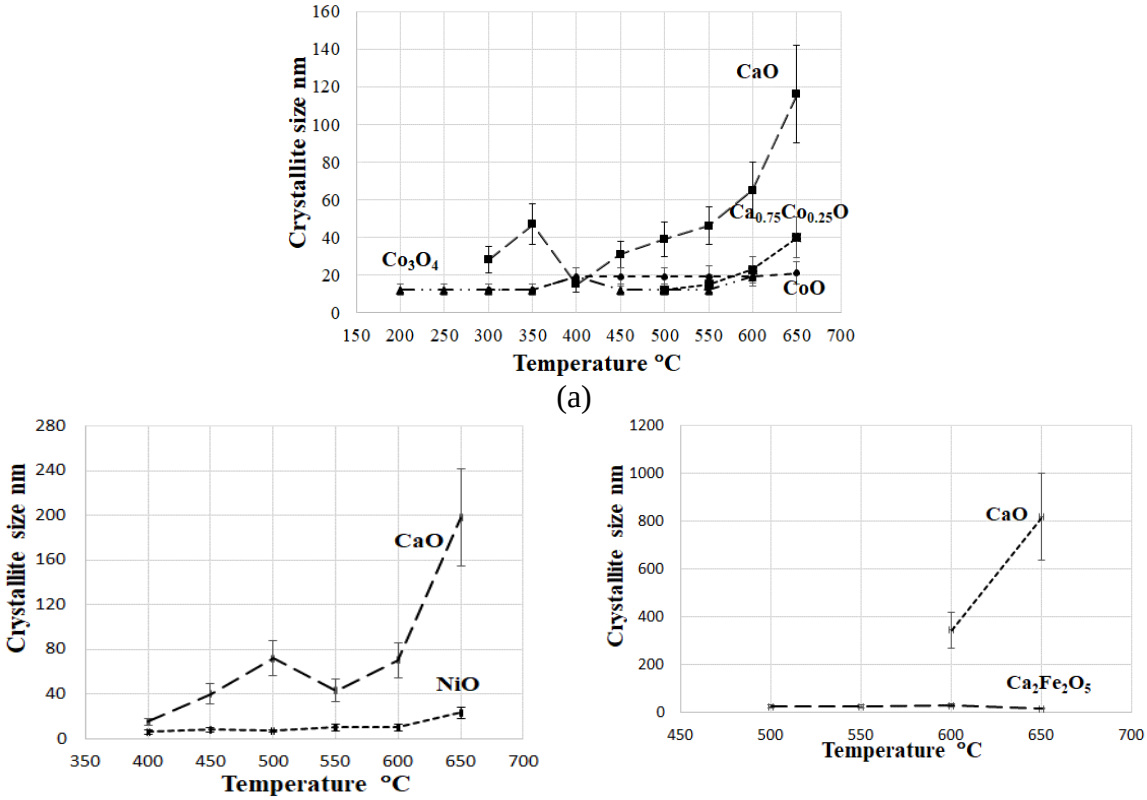

Figure 5.3-10: The crystallite sizes of (a) 0.5CoO:CaO (b) 0.5NiO:CaO and (c) 0.25Fe_2O_3:CaO prepared from 0.5:1 mole ratio of MCl_x to $CaCl_2$ by wet precipitate calcined calcination in air between 25-650 ºC measured at each 50 ºC

The phases as a function of the temperature for 0.5CoO:CaO, 0.5NiO:CaO and 0.25Fe_2O_3:CaO samples were mentioned as seen in Tables 5.3.7 – 5.3.9. Moreover, the quantitative value of the samples at each temperature is also mentioned in Tables 5.3.10 – 5.3.11. Note that the result of the quantitive value for 0.25Fe_2O_3:CaO sample could not be identified exactly.

The crystallization and phase formation of metal oxide doped CaO nanoparticles could not be detected (i) if the crystallite is not large enough (ii) if the concentration is not high enough (iii) if the crystallite is in the amorphous phase. Regarding the series of XRD of zCoO:CaO, zNiO:CaO and zFe_2O_3:CaO (z = 0.1,0.5 / 0.05,0.025) during the calcination, only $Co(OH)_2$ phase at low temperatures has been detected for zCoO:CaO samples. There is no peak of $Ni(OH)_2$ for NiO:CaO sample, and there is no peak of $Fe(OH)_3$ for Fe_2O_3:CaO samples during the calcination at low temperatures. Those happen in both low and high doping amounts of metal oxides doped CaO.

Table 5.3.7: Phases formed from wet precipitate $Co(OH)_2$:$Ca(OH)_2$ during its calcination at different temperatures to 0.5CoO:CaO

Temperature ºC	Phases from Figure 5.3-7
25-150	$Ca(OH)_2 + Co(OH)_2 + CaCO_3$
200	$Ca(OH)_2 + Co(OH)_2 + CaCO_3 + Co_3O_4$
250	$Ca(OH)_2 + CaCO_3 + Co_3O_4$
300-400	$Ca(OH)_2 + CaCO_3 + CaO + CoO + Co_3O_4$
450	$CaCO_3 + CaO + Co_3O_4$
500	$CaCO_3 + CaO + Co_3O_4 + CaCo_2O_4$
500-550	$CaCO_3 + CaO + Co_3O_4 + CaCo_2O_4 + CoO$
600	$CaO + Co_3O_4 + CaCo_2O_4 + CoO$
650	$CaO + CaCo_2O_4 + CoO$

Table 5.3.8: Phases formed from wet precipitate $Ni(OH)_2$:$Ca(OH)_2$ during its calcination at different temperatures to 0.5NiO:CaO

Temperature ºC	Phases from Figure 5.3-8
25- 350	$Ca(OH)_2 + CaCO_3$
400	$Ca(OH)_2 + CaCO_3 + CaO + NiO$
450-600	$CaCO_3 + CaO + NiO$
650	$CaO + NiO$

Table 5.3.9: Phases formed from wet precipitate $Fe(OH)_3$:$Ca(OH)_2$ during its calcination at different temperatures to 0.25Fe_2O_3:CaO

Temperature ºC	Phases from Figure 5.3-9
25	$Ca(OH)_2$
50-300	$Ca(OH)_2 + CaCO_3$
350-450	$CaCO_3$
500-550	$CaCO_3 + Ca_2Fe_2O_5$
600	$CaCO_3 + CaO + Ca_2Fe_2O_5$
650	$CaO + Ca_2Fe_2O_5$

Table 5.3.10: The volume percentages of the different phases (%) found by XRD in the 0.5CoO:CaO sample prepared by heating in air as a function of temperature from Figure 5.3-7

Phases of 0.5CoO:CaO sample	Temperature ºC													
	25	50	100	150	200	250	300	350	400	450	500	550	600	650
$Co(OH)_2$	39	36	38	32	8									
$Ca(OH)_2$	55	53	52	56	67	64	65	58	37					
$CaCO_3$	6	11	11	12	11	15	14	18	28	26	20	17		
CaO							3	2	13	49	46	51	68	78
Co_3O_4					14	12	18	20	22	25	20	14	9	
CoO							1	1	0.1					
$CaCo_2O_4$											12	10	10	6

Table 5.3.11: The volume percentages of the different phases (%) found by XRD in the 0.5NiO:CaO sample prepared by heating in air as a function of temperature from Figure 5.3-8

Phases of 0.5NiO:CaO sample	Temperature ºC													
	25	50	100	150	200	250	300	350	400	450	500	550	600	650
$Ca(OH)_2$	69	62	43	41	32	65	55	28	10					
$CaCO_3$	31	38	57	59	68	35	45	72	43	58	54	49	20	
CaO									4	14	17	32	44	79
NiO									43	28	29	19	36	21

5.3.4 SEM, EDX and TEM characterization of highly doped CaO

SEM and EDS examinations of 0.5CoO:CaO, 0.5NiO:CaO and 0.25 Fe_2O_3:CaO are described in this section. The detailed information of the synthesis is the exact process of low doping amount of metal oxides doped CaO as mentioned in section 4.3.

Figure 5.3-11 showed SEM micrographs of 0.5CoO:CaO, 0.5NiO:CaO and 0.25Fe_2O_3:CaO samples. The average particle size of 0.5CoO:CaO, 0.5NiO:CaO and 0.25Fe_2O_3:CaO were found to be in the range of 146 – 255 nm, 120 – 255 nm and 130 – 255 nm, respectively. The morphology of the 0.5CoO:CaO has a flake shape and homogeneous structure. The morphology of the 0.5NiO:CaO has a sphere shape and the particles are homogeneous structure. The morphology of 0.25Fe_2O_3:CaO has mainly a flake shape and with a few amount are in sphere shape, the sample is not homogeneous.

The EDS spectra and the element composition of the samples 0.5CoO:CaO confirmed the presence of Ca, Co and O. For 0.5NiO:CaO samples, the presence of Ca, Ni and O were confirmed. For 0.25Fe_2O_3:CaO sample, the presence of Ca, Fe and O were found.

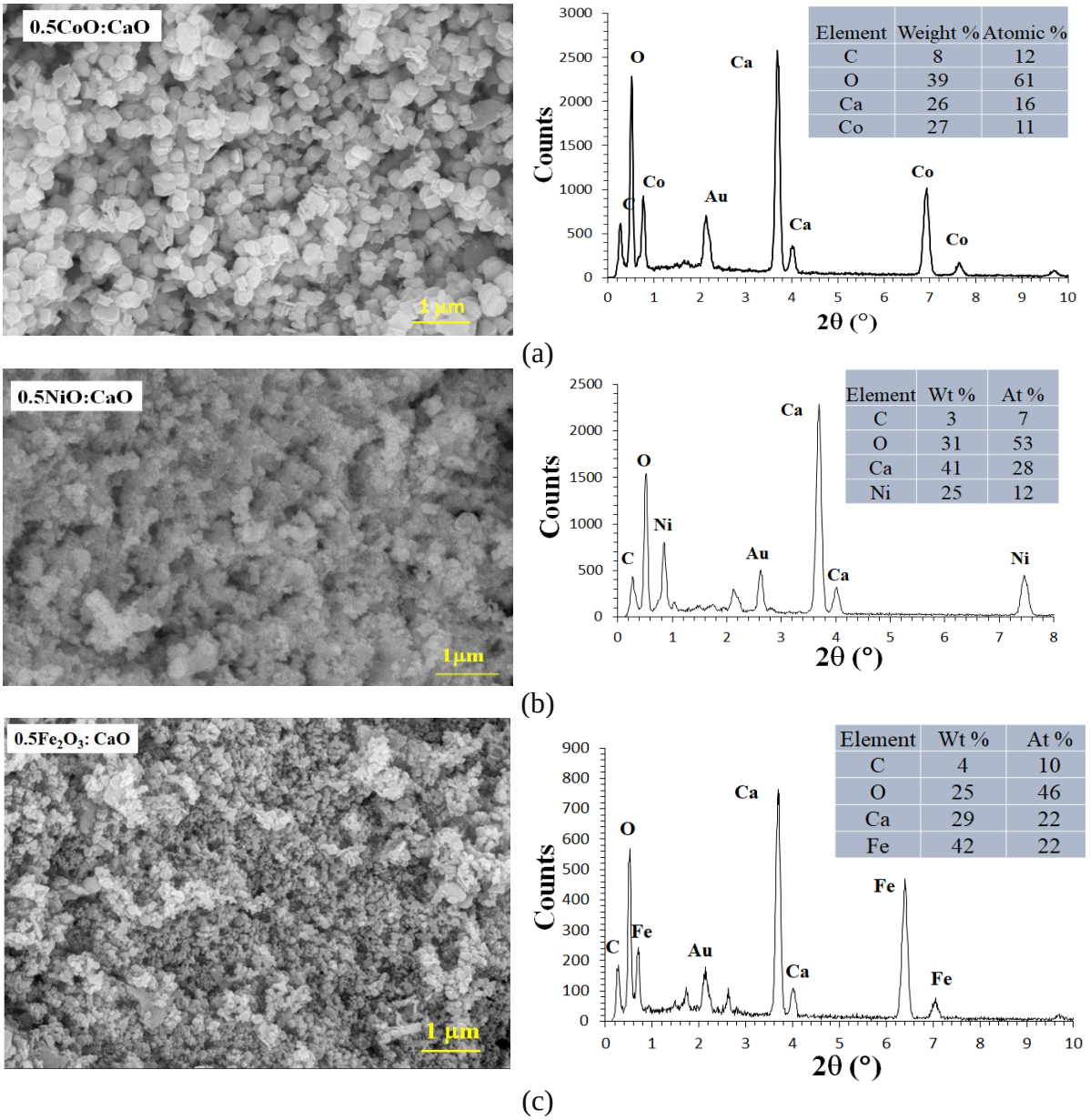

Figure 5.3-11: SEM micrographs (left) showed the morphology of the agglomerated particles and (right) showed chemical composition of the samples (a) 0.5CoO:CaO (b) 0.5NiO:CaO (c) 0.25Fe_2O_3:CaO

TEM micrographs of the samples 0.5CoO:CaO, 0.5NiO:CaO, 0.25Fe_2O_3:CaO are shown in Figure 5.3-12. The left side of the TEM micrographs are the single crystallite (primary single crystal) of each sample which has similar results to XRD. The right side of the TEM micrographs are the agglomerated crystallite (particle) of each sample which has similar results to the SEM micrographs.

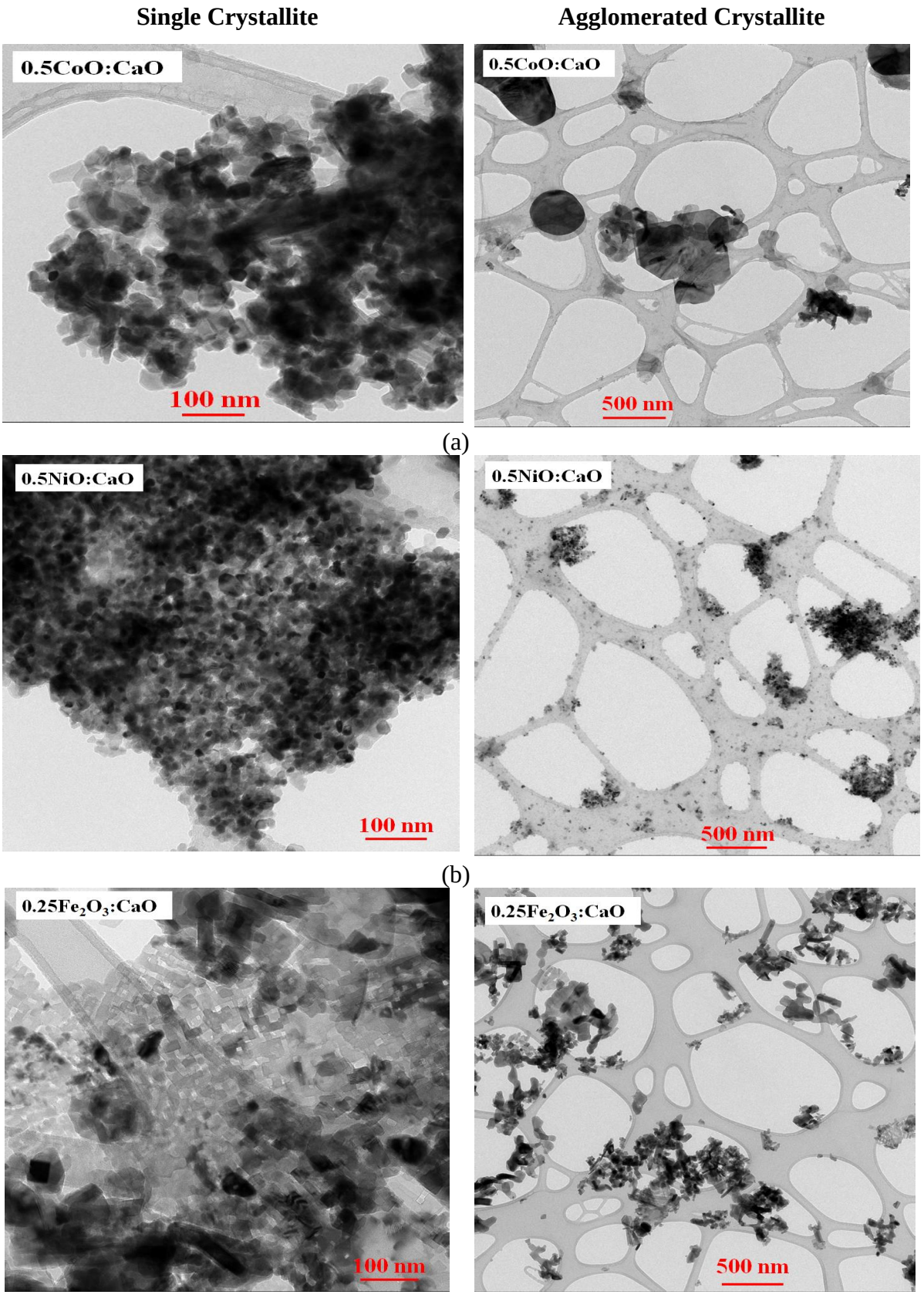

Figure 5.3-12: TEM micrographs(left) showing the single crystallite and (right) showing the agglomerated crystallite (particle) of the samples (a) 0.5CoO:CaO (b) 0.5NiO:CaO (c) 0.25Fe_2O_3:CaO

5.4 Absorption capacity and specific surface areas of pure CaO and metal oxides doped CaO.

In this section, the measurements of CO_2 absorption of pure CaO samples and low-doped and highly-doped CoO, NiO and Fe_2O_3 to CaO samples are mentioned. Each doping sample was prepared based on the ratio 0.1:1 and 0.5:1 of MCl_x to $CaCl_2$ during the reactions. All the samples were calcined from the dry precipitates at 650 °C for one hour in air using the furnace with a heating rate of 15 °C/min. The measurements were performed time dependences of the mass increasing in air. The samples were exposed to air at different temperatures 0, 25, 50, 75, 100, 200 °C until the samples became saturated about 3-6 weeks. The list of the samples at different temperatures for the capturing process has been described in section 4.4.

5.4.1 Absorption capacity and specific surface areas of pure CaO and low-doped CaO.

5.4.1.1 Absorption capacity of pure CaO

The time dependences of the mass increasing for CaO samples at different temperatures are shown in Figure 5.4-1. The initial and final masses of the samples were measured upon the time. As follows from the figure, the mass increasing is faster withing a few initial hours that compare to the mass increasing for the whole process. Moreover, after 3 weeks, all samples reached the saturation stage, i.e., their masses did not increase any more with further holding time. Figure 5.4-2 showed that the fresh CaO sample and the CaO samples which kept at different temperatures for 3-6 weeks. More importantly, the mass increasing of the samples decelerated with the increasing temperature. The average values of the maximum mass ratio of saturated mass and initial mass of the samples are shown in Table 5.4.1.

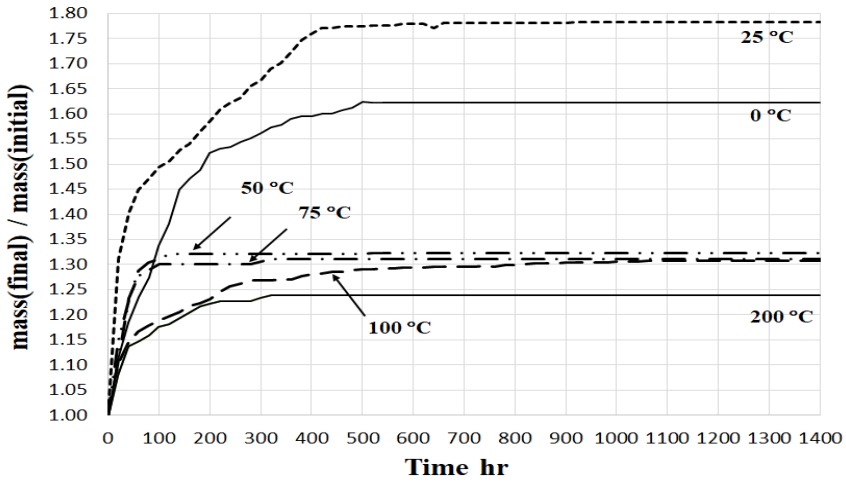

Figure 5.4-1: The time dependence of the relative mass change of pure CaO samples exposed to air at different temperatures

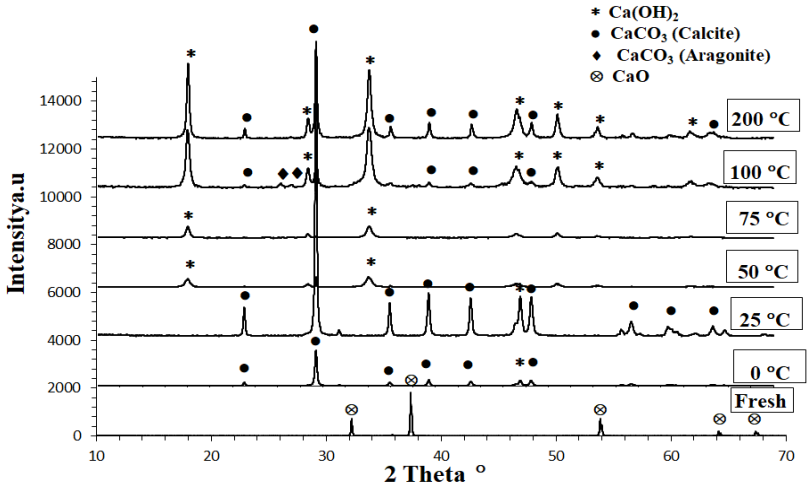

Figure 5.4-2: The XRD diffractograms of pure CaO, fresh sample and after the measurements of the sample exposed to air at different temperatures

Table 5.4.1: The average value of maximum mass ratio of saturated mass and initial mass for pure CaO samples

Temperatures ºC	Initial mass	Saturated mass	average value of maximum mass ratio- m(final)/m(initial)
0	0.89	1.45	1.62
25	0.87	1.55	1.78
50	0.87	1.15	1.32
75	0.9	1.18	1.31
100	0.83	1.08	1.30
200	0.88	1.09	1.23

5.4.1.2 Absorption capacity of 0.1CoO:CaO

The mass increasing depends on the time for 0.1CoO:CaO samples at each different temperature are shown in Figure 5.4-3. The sample measured at 200 ºC which has the capturing process longer than the samples measured at the other different temperatures as seen in figure 5.4.3. The phases changed from the freshly produced sample and after the measurements at different temperatures as see in Figure 5.4-4. The peak formations of $CaCO_3$ and $Ca(OH)_2$ were found to compare with the fresh sample. There is no peak of carbonation or hydration of CoO. The saturated mass and the saturation hour of 0.1CoO:CaO samples at each different temperatures are described in Table 5.4.2.

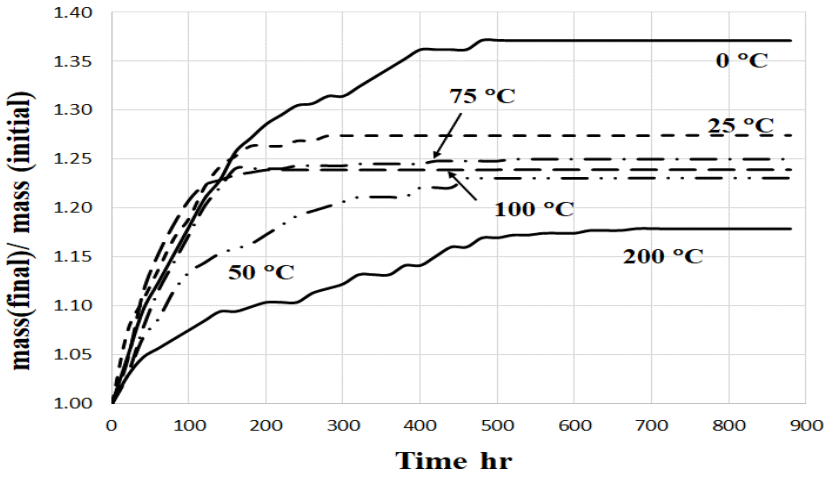

Figure 5.4-3: The time dependence of the relative mass change of 0.1CoO:CaO samples exposed to air at different temperatures

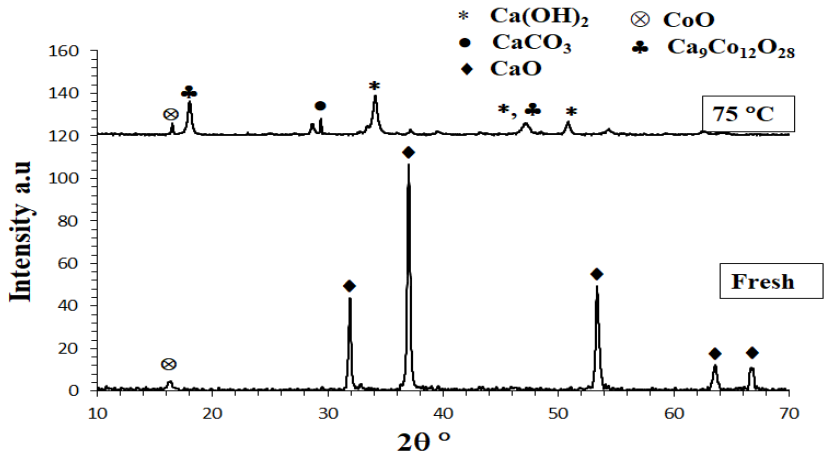

Figure 5.4-4: The XRD diffractogram of 0.1CoO:CaO, fresh sample and after the measurements of the sample exposed to air at different temperatures

Table 5.4.2: The average value of maximum mass ratio of saturated mass and initial mass for 0.1CoO:CaO samples

Temperatures ºC	Initial mass	Saturated mass	average value of maximum mass ratio- m(final)/m(initial)
0	1.05	1.44	1.37
25	0.95	1.21	1.27
50	1.01	1.25	1.24
75	1.04	1.3	1.25
100	1.04	1.28	1.23
200	1.06	1.25	1.18

5.4.1.3 Absorption capacity of 0.1NiO:CaO

Figure 5.4-5 shows the mass increasing upon the time for 0.1NiO:CaO sample. The mass increasing of the sample kept at 0 ºC becomes constant about 6 weeks. In the samples measured at 50 -75 ºC, the mass increases faster in the initial hours and becomes constant within a few hours. Figure 5.4-6 shows the phases changed from the freshly produced sample and the sample after the measurement at different temperatures. The XRD diffractograms of the measured samples at different temperatures revealed the new peak formations of $CaCO_3$ and $Ca(OH)_2$. There is no peak of carbonation or hydration of NiO. The average value of the maximum mass ratio of saturated mass and initial mass for 0.1NiO:CaO samples at different temperatures are shown in Table 5.4.3.

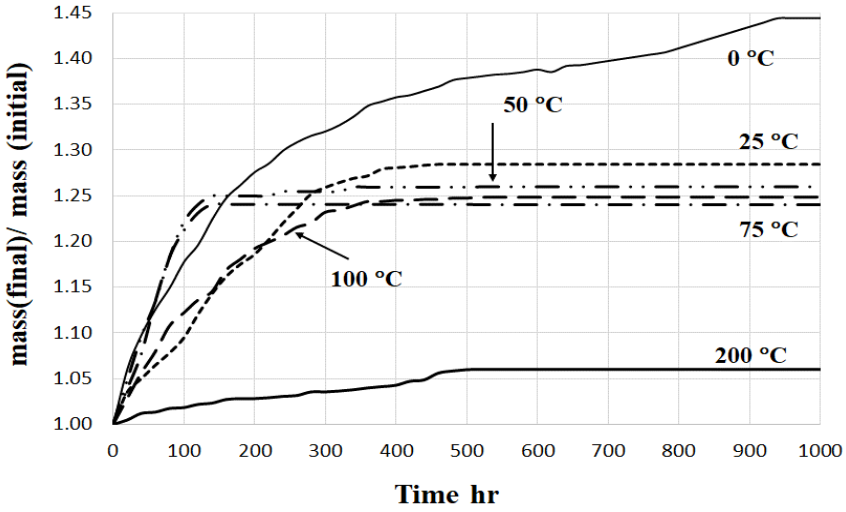

Figure 5.4-5: The time dependence of the relative mass change of 0.1NiO:CaO samples exposed to air at different temperatures

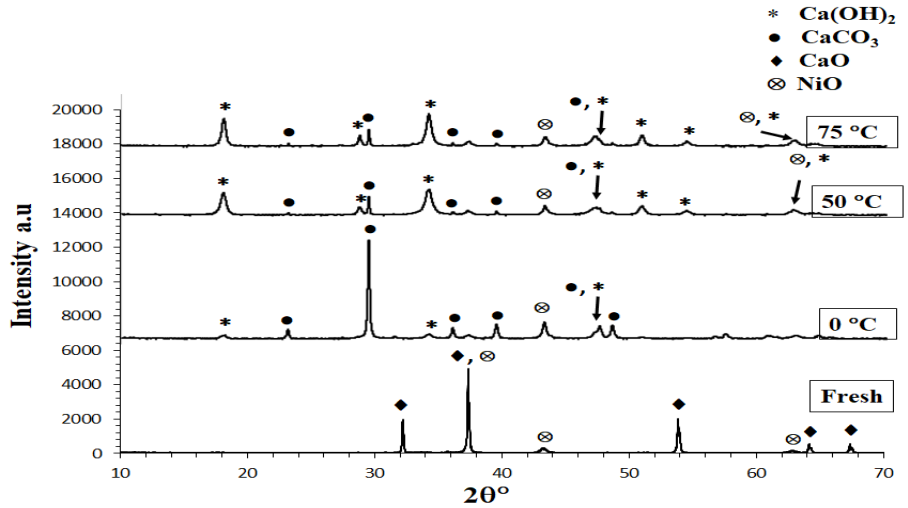

Figure 5.4-6: The XRD diffractogram of 0.1NiO:CaO fresh sample and after the measurements of the sample exposed to air at different temperatures

Table 5.4.3: The average value of maximum mass ratio of saturated mass and initial mass for 0.1NiO:CaO samples

Temperatures ºC	Initial mass	Saturated mass	average value of maximum mass ratio- m(final)/m(initial)
0	1.07	1.55	1.45
25	1.09	1.4	1.28
50	1.04	1.31	1.26
75	1.04	1.29	1.24
100	1.07	1.33	1.25
200	1.03	1.09	1.06

5.4.1.4 Absorption capacity of $0.05Fe_2O_3$:CaO

In Figure 5.4-7, the sample measured at 0 ºC showed a mass increases gradually over time and the saturated hour is about 6 weeks. The samples measured at other different temperatures became saturated within 3 weeks. Figure 5.4-8 shows the XRD diffractograms in which only two new peaks formations were occurred for the measured samples to compare the freshly prepared sample; there is no peak of carbonated or hydrated of iron oxide. Thus, the exact situation occur as 0.1CoO:CoO and 0.1NiO:CaO samples. Table 5.4.4 shows the average value of the maximum mass ratio of saturated mass and initial mass for $0.05Fe_2O_3$:CaO samples.

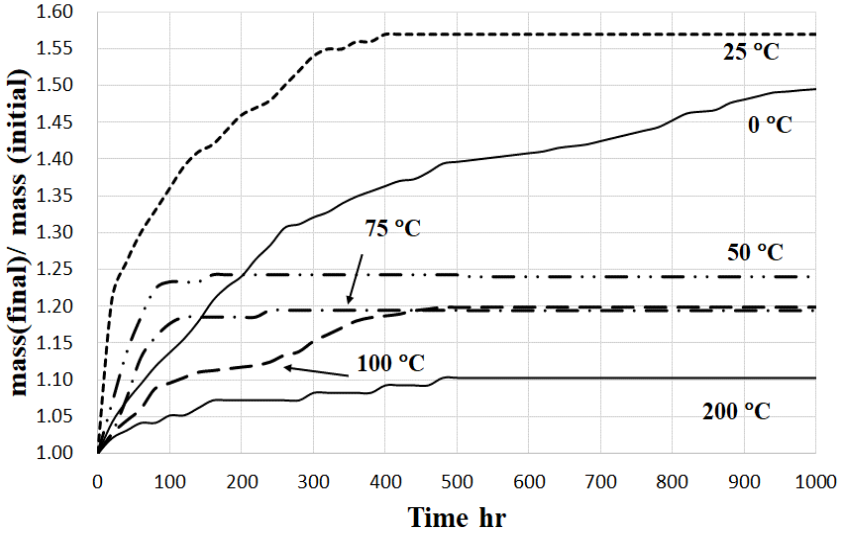

Figure 5.4-7: The time dependence of the relative mass change of $0.05Fe_2O_3$:CaO samples exposed to air at different temperatures

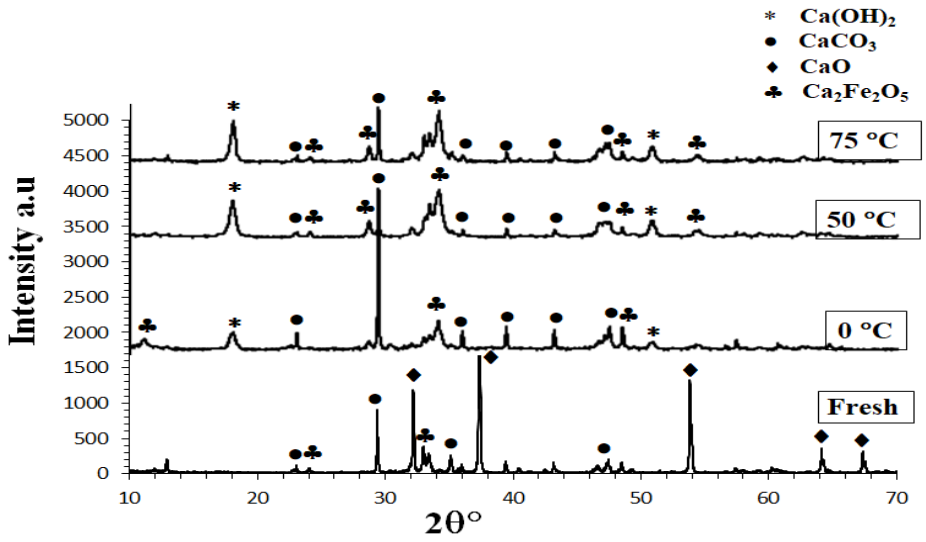

Figure 5.4-8: The XRD diffractogram of $0.05Fe_2O_3$:CaO, fresh sample and after the measurements of the sample exposed to air at different temperatures

Table 5.4.4: The average value of maximum mass ratio of saturated mass and initial mass for $0.05Fe_2O_3$:CaO samples

Temperatures ºC	Initial mass	Saturated mass	average value of maximum mass ratio- m(final)/m(initial)
0	1.06	1.58	1.49
25	1	1.57	1.57
50	1.03	1.28	1.24
75	1.08	1.29	1.19
100	1.04	1.24	1.2
200	0.97	1.07	1.10

Table 5.4.5 shows the BET analysis of pure CaO sample, low doped CaO (0.1CoO:CaO, 0.1NiO:CaO and $0.05Fe_2O_3$:CaO). In the table, the specific surface areas of the fresh samples and the samples after the measurement of capturing process at room temperatures are mentioned. Pure CaO fresh sample has a specific surface area of 4.34 m^2g^{-1}. After the measurement of capturing process at room temperature in air for 3 weeks, the specific surface area increased to 6.05 m^2g^{-1}. This is due to the absorption of CO_2 by CaO nanoparticles and by the transformation of the latter into $CaCO_3$. The average pore diameters exchanged from 11 nm for fresh CaO to 17 nm after the measurement of capturing process at room temperature.

0.1CoO:CaO, 0.1NiO:CaO and 0.05Fe_2O_3:CaO fresh samples have the specific surface area of 6.02 m^2g^{-1}, 7.8 $m^2g^{-1}$and 6.74 m^2g^{-1} respectively. After measurements of the same samples at 25 ºC in air for 3-6 weeks, the specific surface area of the samples exchanged to 12.2 m^2g^{-1}, 7.16 $m^2g^{-1}$and 9.4 m^2g^{-1}respectively. Moreover, the average pore diameters of the fresh samples to measured samples exchange from 14 nm to 23 nm for 0.1CoO:CaO, 24 nm to 28 nm for 0.1NiO:CaO and 24 nm to 26 nm for 0.05Fe_2O_3:CaO.

Table 5.4.5: The specific surface area of pure CaO and low-doped CaO, fresh samples and after capturing for 3-6 weeks at room temperature

Samples	Specific surface area (BET) m^2g^{-1}	Surface area of the pore (BJH)		Cumulative pore volume of the pore (BJH)		Absorption average pore diameter	
		Absorption m^2g^{-1}	Desorption m^2g^{-1}	Absorption $cm^3\ g^{-1}$	Desorption $cm^3\ g^{-1}$	(BET) nm	BJH nm
CaO (fresh) (Air)	4.34	3.05	3.2	0.016	0.016	11	21
CaO (captured)	6.05	5.06	5.28	0.031	0.031	16	24
0.1Co:CaO (Fresh)	6.02	4.65	4.74	0.016	0.016	9	14
0.1Co:CaO (captured)	12.2	10.6	2.98	0.062	0.041	17	23
0.1Ni:CaO (Fresh)	7.8	6.43	6.78	0.038	0.038	17	24
0.1Ni:CaO (captured)	7.16	5.92	7.6	0.041	0.041	20	28
0.05Fe:CaO (Fresh)	6.74	5.41	5.58	0.032	0.032	15	24
0.05Fe:CaO (captured)	9.4	6.97	7.55	0.047	0.047	17	26

5.4.2 Absorption capacity and specific surface areas of highly doped CaO

In this section, the measurements of the absorption process for three different metal oxides (CoO, NiO and Fe_2O_3) doped CaO are described. Each doping sample was prepared based on the ratio 0.5: 1 of MCl_x to $CaCl_2$ during the reactions. All the samples were calcined

from the dry precipitates at 650 °C for one hour in air using the furnace with a heating rate of 15 °C/min. The sample preparations and the measurements of the absorption capacity are typically the same processes of the low doping amount of metal oxides of CaO. The samples were exposed to air at different temperatures 0, 25, 50, 75, 100 and 200 °C until the samples became saturated about 3-6 weeks.

5.4.2.1 Absorption capacity of 0.5CoO:CaO

Figure 5.4-9 shows the time dependences of the mass increase for each 0.5CoO:CaO sample at different temperatures. At 0 ºC, the mass increasing of the samples rises gradually until 3 weeks, as seen in the figure. The mass ratio of the samples measured at 50 - 200 ºC has a much lower value than the samples measured at 0 ºC. Figure 5.4-10 shows the XRD diffractogram of the samples in which phases changed from the freshly produced sample and the samples after the measurement at different temperatures. In the measured sample, only new peaks of $CaCO_3$ and $Ca(OH)_2$ appeared. There is no formation of carbonated or hydrated CoO. Table 5.4.6 shows the average value of the maximum mass ratio of saturated mass and initial mass of 0.5CoO:CaO samples at different temperatures.

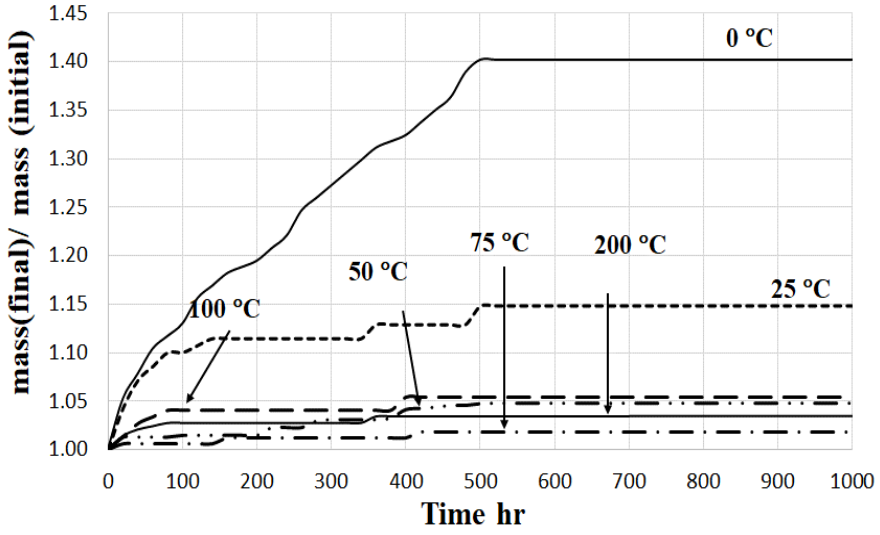

Figure 5.4-9: The time dependence of the relative mass change of 0.5CoO:CaO samples exposed to air at different temperatures

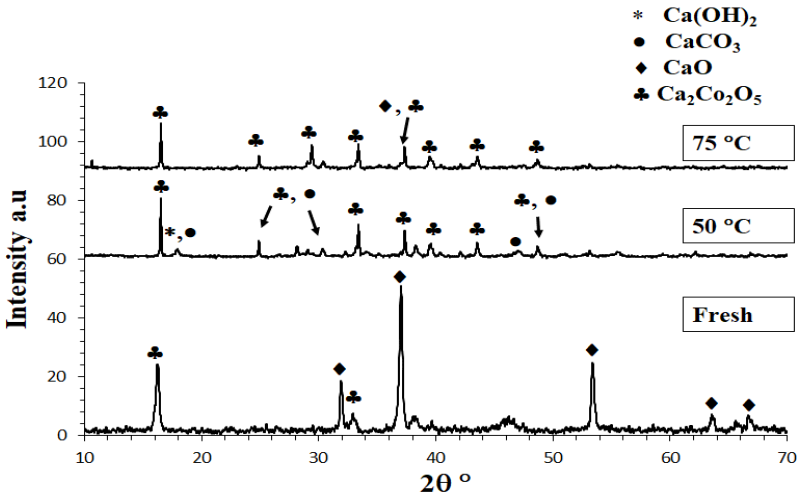

Figure 5.4-10: The XRD diffractogram of 0.5CoO:CaO, fresh sample and after the measurements of the sample exposed to air at different temperatures

Table 5.4.6: The average value of the maximum mass ratio of saturated mass and initial mass of 0.5CoO:CaO samples

Temperatures ºC	Initial mass	Saturated mass	average value of maximum mass ratio- m(final)/m(initial)
0	0.78	1.08	1.38
25	0.70	0.8	1.24
50	0.78	0.8	1.03
75	0.8	0.82	1.03
100	0.74	0.78	1.05
200	0.73	0.76	1.04

5.4.2.2 Absorption capacity of 0.5NiO:CaO

The time dependences of the mass increase of 0.5NiO:CaO samples are shown in Figure 5.4-11. At 0 ºC, the duration of capturing process of the sample is up to 6 weeks while the mass increases gradually. Only at that temperature the value of the mass ratio is much higher than the other samples measured at other different temperatures. Figure 5.4-12 shows XRD pattern of the freshly produced sample and after the measurement was done at the measured temperatures. There are new peaks formation of $CaCO_3$ and $Ca(OH)_2$ in the measured samples as 0.5NiO:CaO. There is no formation of carbonated or hydrated NiO. That has a similar situation as 0.5CoO:CaO. The average value of the maximum mass ratio of saturated mass and initial mass of 0.5NiO:CaO samples is shown in Table 5.4.7.

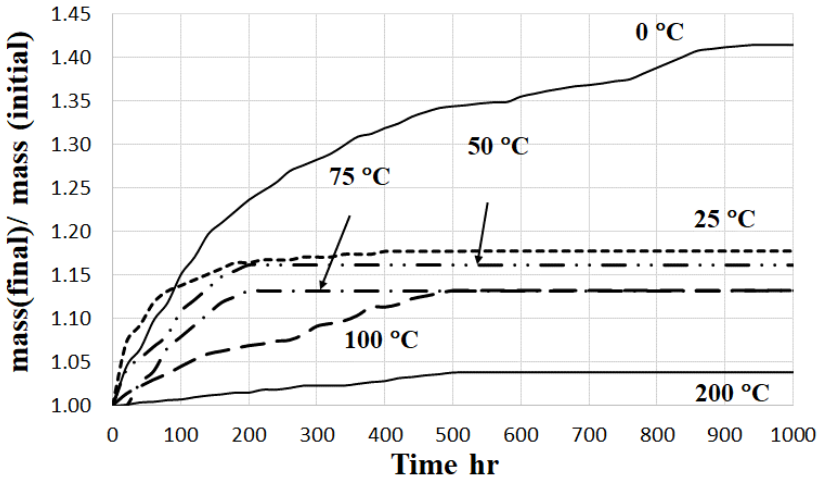

Figure 5.4-11: The time dependence of the relative mass change of 0.5NiO:CaO samples exposed to air at different temperatures

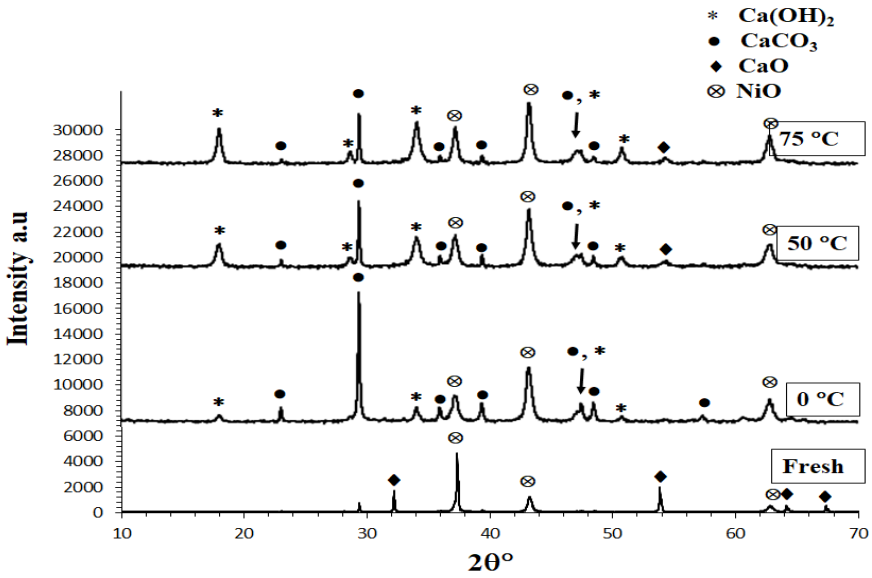

Figure 5.4-12: The XRD diffractogram of 0.5NiO:CaO, fresh sample and after the measurements of the sample exposed to air at different temperatures

Table 5.4.7: The average value of maximum mass ratio of saturated mass and initial mass of 0.5NiO:CaO samples

Temperatures ºC	Initial mass	Saturated mass	average value of maximum mass ratio- m(final)/m(initial)
0	0.76	1.08	1.42
25	1.52	1.79	1.18
50	0.74	0.86	1.16
75	0.76	0.86	1.13
100	0.77	0.88	1.14
200	0.74	0.77	1.04

5.4.2.3 Absorption capacity of $0.25Fe_2O_3$:CaO

Figure 5.4-13 shows the $0.25Fe_2O_3$:CaO nanoparticles that were measured for the absorption process in air at different temperatures 0 - 200 ºC for 3-6 weeks. At 0 and 25 ºC, the saturated mass of the samples is higher than the samples measured at higher temperatures. XRD diffractograms of the freshly produced sample and the samples after the measurements at different temperatures. In the measured samples, those have only a new peak of $CaCO_3$. There is no peak of carbonated or hydrated iron oxide as same as 0.5CoO:CaO and 0.5NiO:CaO samples, as seen in Figure 5.4-14. The average value of the maximum mass ratio of saturated mass and initial mass of $0.25Fe_2O_3$:CaO samples is shown in Table 5.4.8.

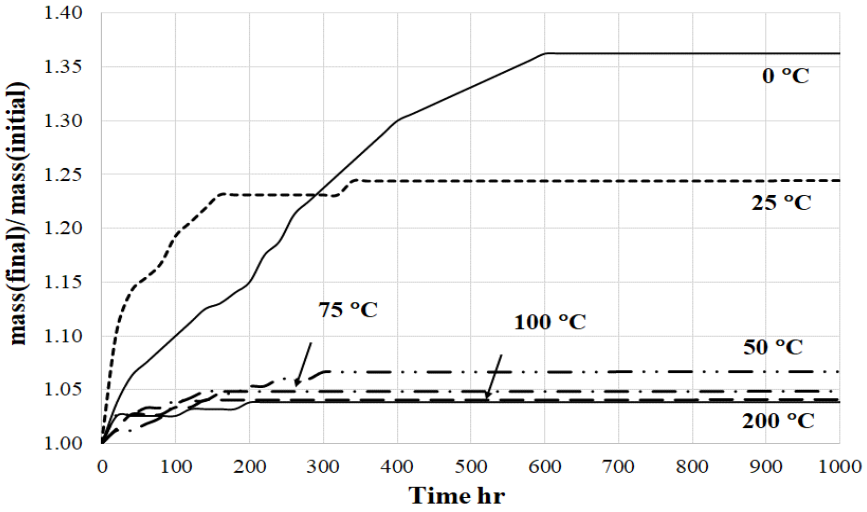

Figure 5.4-13: The time dependence of the relative mass change of $0.25Fe_2O_3$:CaO samples exposed to air at different temperatures

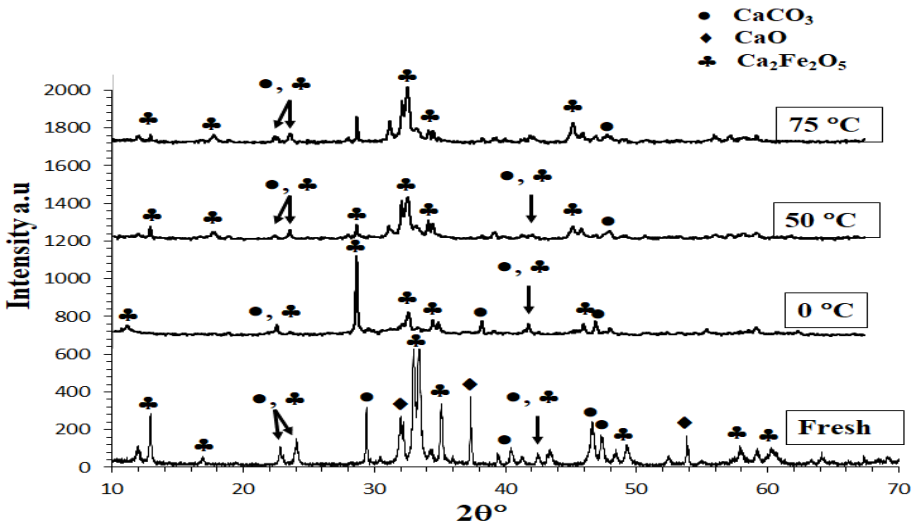

Figure 5.4-14: The XRD diffractogram of $0.25Fe_2O_3$:CaO, fresh sample and after the measurements of the sample exposed to air at different temperatures

Table 5.4.8: The average value of maximum mass ratio of saturated mass and initial mass of $0.25Fe_2O_3$:CaO samples

Temperatures ºC	Initial mass	Saturated mass	average value of maximum mass ratio- m(final)/m(initial)
0	0.8	1.09	1.36
25	0.78	0.97	1.24
75	0.75	0.8	1.07
75	0.82	0.86	1.05
100	0.74	0.77	1.04
200	0.79	0.82	1.04

Table 5.4.9 shows the BET analysis of the samples 0.5CoO:CaO, 0.5NiO:CaO and $0.25Fe_2O_3$:CaO. This table shows the results of fresh samples and the samples measured at 25 ºC after 3-6 weeks.

0.5CoO:CaO, 0.5NiO:CaO and $0.25Fe_2O_3$:CaO fresh samples have found the specific surface area of 3.56 m^2g^{-1}, 7.79 m^2g^{-1} and 13.39 m^2g^{-1}. After keeping the same samples at 25 ºC in air for 3-6 weeks, the specific surface area of the samples exchanged to 13.12 m^2g^{-1}, 19.34 m^2g^{-1} and 15.94 m^2g^{-1}, respectively. Moreover, the average pore diameters of the fresh samples to measured samples exchange from 22 nm to 21 nm for 0.5CoO:CaO, 31 nm to 24 nm for 0.5NiO:CaO and 24 nm to 22 nm for $0.25Fe_2O_3$:CaO.

Table 5.4.9: The specific surface area of highly low doped CaO, fresh samples and after capturing for 3-6 weeks at room temperature

Samples	Specific surface area (BET) m^2g^{-1}	Surface area of pore (BJH)		Cumulative pore volume of pore (BJH)		Absorption average pore diameter	
		Absorption m^2g^{-1}	Desorption m^2g^{-1}	Absorption $cm^3\ g^{-1}$	Desorption $cm^3\ g^{-1}$	(BET) nm	BJH nm
0.5Co:CaO (Fresh)	3.56	2.91	2.97	0.0152	0.0152	15	21
0.5Co:CaO (captured)	13.12	11.35	12.15	0.063	0.064	17	22
0.5Ni:CaO (Fresh)	7.79	7.16	7.7	0.054	0.055	26	31
0.5Ni:CaO (captured)	19.34	18.16	20.7	0.11	0.11	21	24
$0.25Fe_2O_3$:CaO (Fresh)	13.39	12.37	13.1	0.075	0.076	20	24
$0.25Fe_2O_3$:CaO (captured)	15.94	12.03	13.52	0.065	0.066	14	22

5.4.3 The summary of capturing efficiency of pure CaO and metal oxides doped CaO nanoparticles

The expected primary reaction of the air components with CaO nanoparticles is the capture of carbon dioxide from air: $CaO_{(s)} + CO_{2(g)} = CaCO_{3(s)}$

This reaction is accompanied by the following standard Gibbs energy changes in kilojoules per mole (at different temperatures given in °C): -133.98(0), −129.9 (25), -125.96(50), -121.93(75), −117.8 (100), and − 101.6 (200) kJ/mol. Indeed, when CaO was kept at 25 °C, it was fully transformed into the calcite form of $CaCO_3$ (also seen in Fig. 5.4-2). The theoretical ratio of the molar masses of $CaCO_3$ to CaO is as below:

$$\frac{\mathrm{m(final)}}{\mathrm{m(initial)}} = \frac{\mathrm{M(CaCO3)}}{\mathrm{M(CaO)}} = \frac{100.15}{56.07} = 1.786 \qquad \text{Eq 5.4.3-1}$$

This ratio is practically the same as found at the end of the experiment performed at 25 °C, as seen in Figure 5.4-2. Further confirming that at room temperature, CaO nanoparticles are able to capture carbon dioxide from air and the full capacity measured for this process within 3 weeks. Note that although the 3 weeks seems a long time, this process does not need industrial conditions. The CaO nano-particles deposited on the field will slowly but surely absorb CO_2 from surrounding air at low temperatures 0 and 25 °C.

Pure CaO transformed to $CaCO_3$ at room temperature, which means CaO fully absorbed CO_2 100%. For 0.1CoO:CaO, the existence of CaO and $Ca_2Co_2O_5$ were found, while in the 0.5CoO:CaO sample, CaO, $Ca_{0.75}Co_{25}O$ and CoO phases exist. In 0.1NiO:CaO and 0.5NiO:CaO samples, there are only the existence of CaO and NiO. For 0.05Fe_2O_3:CaO, the existence of CaO, $Ca_2Fe_2O_5$ and Fe_2O_3 was found. But in the 0.25Fe_2O_3:CaO, only CaO and Fe_2O_3 exist. Among those different compositions, only CaO transformed to $CaCO_3$ or $Ca(OH)_2$ and $CaCO_3$. There is no carbonation or hydration of doping metal oxides and compounds due to the diluting effect.

As proof, XRD diffractograms of fresh samples and measured samples were described in section 5.4. Therefore, low and highly-doped CaO samples in which CaO can be considered for the carbonation. The molar mass of doped CaO (X_{CaO}) is calculated by the following equation as an example in equation 5.4.3.2. The molar mass of other sample X_{CaO} is described in Table 5.4.10. As an example, the molar mass of 0.1CoO:CaO, X_{CaO};

$$0.1\mathrm{CoO{:}CaO} = \frac{\mathrm{M(CaO)}}{\mathrm{M(0.1CoO+CaO)}} = \frac{56.08}{0.1(74.93)+56.08} = 0.88 \qquad \text{Eq 5.4.3-2}$$

The theoretical mass ratio of $CaCO_3$ to X_{CaO} is as below:

$$\frac{m(final)}{m(initial)} = 1 + (0.78 \bullet X_{CaO}) \qquad \text{Eq 5.4.3-3}$$

The capturing efficiency of pure CaO (%) for each sample is calculated by the following equation.

$$\text{Capturing efficiency (\%) of CaO} = 100 \bullet \left[\frac{\left(\frac{m(final)}{m(initial)}(measured) - 1\right)}{1.786(theo) - 1} \right] \qquad \text{Eq 5.4.3-4}$$

The capturing efficiency of doped CaO (X_{CaO}) (%) for each sample is calculated by the following equation.

$$\text{Capturing efficiency (\%) of } X_{CaO} = 100 \bullet \left[\frac{\left(\frac{m(final)}{m(initial)}(measured) - 1\right)}{0.78 + X_{CaO}} \right] \qquad \text{Eq 5.4.3-5}$$

Table 5.4.10 describes the maximum mass ratio of pure CaO and metal oxides doped CaO while the mass increasing becomes saturated. The maximum mass ratios were shown in percentage at different measured temperatures. The measurements at low temperatures, 0 °C and 25 °C, CaO samples have the highest absorption capacity of CO_2 capturing. As a proof, the comparison of XRD diffractograms for fresh samples and the samples measured at different temperatures have been described in section 5.3. At higher temperatures, the sample captured not only CO_2 but also moisture. But the capturing of moisture H_2O is much higher while a few amounts of CO_2 capturing occurred. Therefore, capturing CO_2 using doped CaO is recommended at 0 °C and 25 °C.

Table 5.4.10: The maximum mass ratio in percentage of each sample as a function of different temperatures

Samples	Molar mass of X_{CaO}	Theoretical maximum mass ratio	Capturing efficiency (%) at each different temperature °C					
			0	25	50	75	100	200
CaO	-	1.78	79	100	41	40	38	29
0.1CoO:CaO	0.88	1.69	54	39	35	36	33	26
0.5CoO:CaO	0.6	1.47	81	51	6	5	11	9
0.1NiO:CaO	0.88	1.69	65	41	38	35	36	8
0.5NiO:CaO	0.6	1.47	90	38	34	28	30	9
0.05Fe_2O_3:CaO	0.88	1.68	72	83	35	28	29	15
0.25Fe_2O_3:CaO	0.58	1.46	100	53	15	11	9	9

Figure 5.4-15 shows the maximum capturing capacity of pure CaO and low-doped CaO nanoparticles as a function of different temperatures. Regarding the graphs, CaO has 100 % capturing capacity at 25 °C. By doping of different metal oxides to CaO enhance the stability of the absorption capacity at different higher temperatures. The temperatures at 0 °C and 25 °C, in the order of high to low capturing efficiency, are pure CaO, 0.05Fe_2O_3:CaO, 0.1NiO:CaO and 0.1CoO:CaO. At the measured temperatures 50, 75 and 100 °C, the absorption capacity of metal oxide doped to CaO has a similar result in the range of 30- 40 %.

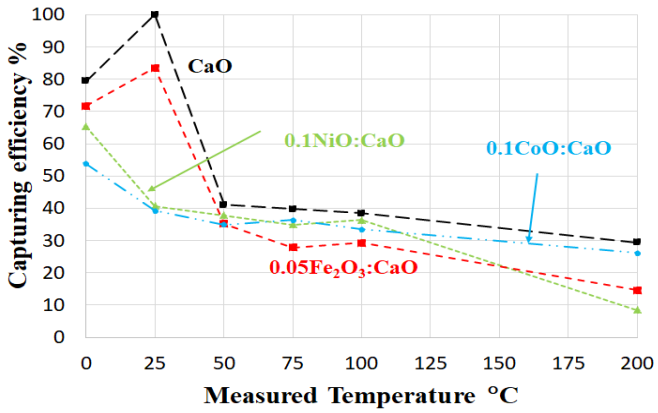

Figure 5.4-15: The maximum capturing capacity % of pure CaO and 0.1CoO:CaO, 0.1NiO:CaO and 0.05Fe_2O_3:CaO at different measured temperatures

Figure 5.4-16 shows the maximum capturing capacity of pure CaO and highly doped CaO nanoparticles as a function of different temperatures. At the temperature 0 °C, the capturing efficiency exchange in the order of high to low i.e; CaO, 0.5CoO:CaO, 0.25Fe_2O_3:CaO and 0.5NiO:CaO. At temperatures 25, 50, 75 and 100 °C, the capturing efficiency of metal oxide doped to CaO has a similar result, while the capturing capacity is much lower than pure CaO sample.

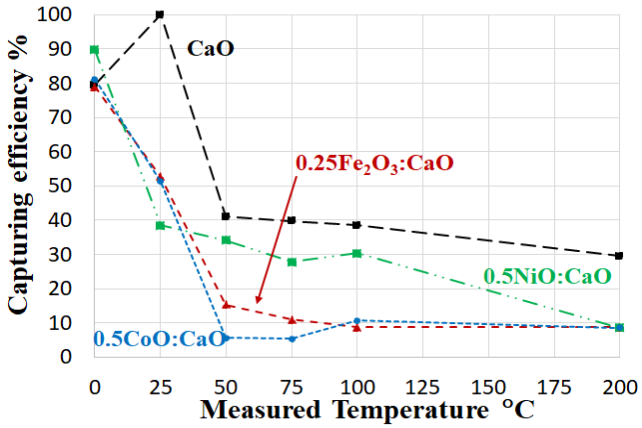

Figure 5.4-16: The maximum capturing capacity (%) of pure CaO and 0.5CoO:CaO, 0.5NiO:CaO and 0.25Fe_2O_3:CaO at different measured temperatures

5.5 Conclusions

-The selection of metal oxide nanoparticles through precipitation -calcination method from metal chloride and NaOH aqueous solutions by the theoretical approach has been studied. According to Chapter 2, 13 metal oxides (Al_2O_3, BeO, CdO, CaO, CoO/Co_3O_4, CuO, FeO, Fe_2O_3, MgO, MnO, NiO, SnO and ZnO) could be produced by using precipitation-calcination method from metal chloride and NaOH aqueous solutions.

- Additionally, CaO, MnO, CdO and Co_3O_4 could be used for carbonation in air. FeO, MgO, ZnO and NiO are found as possible candidates for partial carbon dioxide capture, but they cannot lower the current carbon dioxide content in air (420 ppm) to the target value of 42 ppm.

- In this research, CaO has been produced in different environments (under vacuum and in air) during calcination. CaO samples, which calcined in air, lead to the formation of 100 % pure CaO powder and smaller crystallite sizes.

-The analysis of the crystallite sizes and compositions of (CoO, NiO and Fe_2O_3) doped CaO nanoparticles; low-doped and highly doped CaO has been investigated. Low-doped CaO; 0.1NiO:CaO has two phases with the crystallite sizes of CaO (42 nm) and NiO (12 nm). 0.1CoO:CaO has two phases with the crystallite sizes of CaO (105 nm) and $Ca_2Co_2O_5$ (50 nm). For 0.05Fe_2O_3:CaO sample has three phases with the crystallite sizes of CaO (165 nm), Fe_2O_3 (810 nm) and $Ca_2Fe_2O_5$ (14 nm). Highly doped CaO; 0.5NiO:CaO has two phases with the crystallite sizes of CaO (200 nm) and NiO (20 nm). For 0.5CoO:CaO sample has two phases with the crystallite sizes of CaO (120 nm) and $Ca_2Co_2O_5$ (40 nm). In the 0.25Fe_2O_3:CaO sample, there are two phases with the crystallite sizes of CaO (820 nm) and $Ca_2Fe_2O_5$ (30 nm), respectively.

-The analysis of the absorption capacity of CO_2 for pure CaO and metal oxides doped CaO in air at low temperatures (0,25,50,75,100 and 200) °C have been studied. The absorption capacity of CaO at 25 °C has 100% efficiency.

6. Claims

In this work, aqueous solutions of different metal chlorides (for example, calcium chloride) were mixed with an aqueous solution of NaOH at 80 °C. As a result, usually solid crystalline metal hydroxide (for example, calcium hydroxide) precipitates from the solution and the side product NaCl remains dissolved in it. The precipitates were collected by filtering and washed by water to decrease their NaCl contamination. Then, the samples were dried overnight and calcined to obtain metal oxide particles (for example, calcium oxide). These metal oxide particles appeared to be nano-sized, or at least sub-micron sized. These metal oxide samples were kept in normal air at different temperatures for several weeks to measure their mass increase, indicating capture of some carbon dioxide from air by the formation of metal carbonate (for example, calcium carbonate). In this work, the structure and phase composition of the synthesized nano-metal-oxide samples are measured before and after carbonization as a function of synthesis conditions and conditions of carbon dioxide capture. Additionally, a model is made to understand and predict the processes better.

Claim 1: Theoretical results

1.1. Selection of useful metal chloride to prepare nano-metal-oxides. All existing stable solid metal chlorides were analyzed using mostly thermodynamic data from literature to select those metals, whose nano-metal-oxides can be produced from their metal chlorides with reasonable efficiency by the method described above. The criteria considered are as follows: (i) sufficient solubility of the given metal chloride in water, (ii) sufficient ability of the given metal chloride to convert into metal hydroxide by 1 M NaOH, (iii) low enough solubility of the given metal hydroxide in water to ensure its fast precipitation, (iv) reasonably low calcination temperature at which the given metal hydroxide can be converted into the desired metal oxide ensuring its nano-structure. It is claimed here that the following 13 nano-metal-oxides can be produced by the above-described method: Al_2O_3, BeO, CdO, CaO, CoO/Co_3O_4, CuO, FeO, Fe_2O_3, MgO, MnO, NiO, SnO and ZnO (note: CoO is primarily produced but if calcination is performed in air, then CoO is oxidized to Co_3O_4). These theoretical results are confirmed by literature data on experimental findings.

1.2. Selection of nano-metal-oxides from the above list that can capture carbon dioxide from air reducing its content 10-fold. The 13 metal oxides listed in Claim 1.1 are theoretically tested for their ability to capture carbon dioxide from air under standard temperature lowering the partial pressure of carbon dioxide from its present average value in our environment of 420 ppm to the target value of 42 ppm. The result is (in order of their decreasing ability to capture carbon dioxide): CaO, MnO, CdO, Co_3O_4. Additionally, FeO, MgO, ZnO and NiO are found as possible candidates for partial carbon dioxide capture, but they cannot lower the current carbon dioxide content in air 420 ppm to the target value of 42 ppm.

Claim 2. Effect of calcination environment (vacuum or air) on CaO nano-particles

CaO nanoparticles were prepared from wet $Ca(OH)_2$ precipitates by calcination during 1 hour between 25 and 650 °C in two different environments: vacuum and air (vacuum is a usual method in the literature, air is the novel and simple method).

2.1. Transformation temperature. It is shown that the temperature of full transformation of $Ca(OH)_2$ into CaO is lower when calcination is performed in vacuum 600 °C, as seen in Figure C1 compared when it is transformed in air 650 °C, as seen in Figure C1 b. This is due to the high entropy of the gaseous reaction product H_2O that drives the dissociation reaction in vacuum further and faster compared to the case when calcination is performed in air.

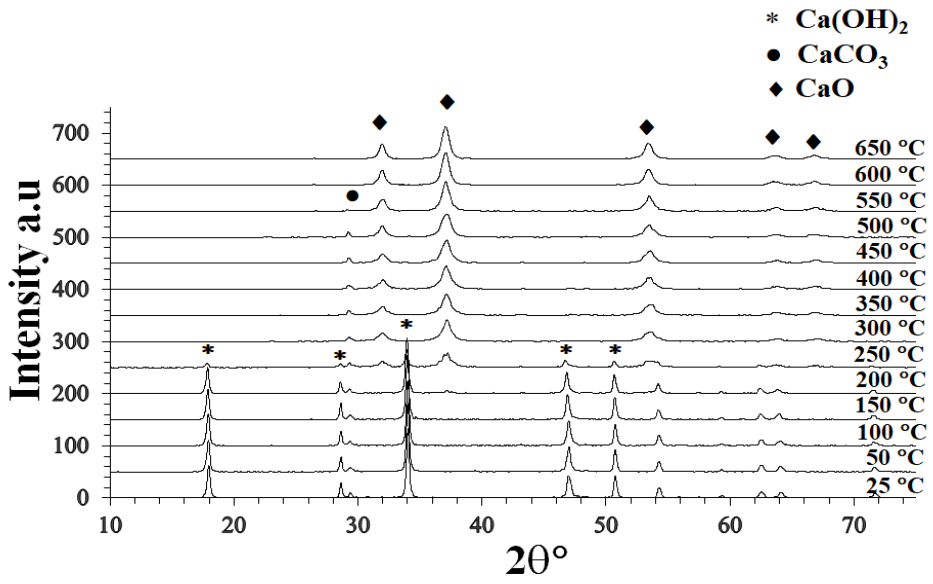

(a)

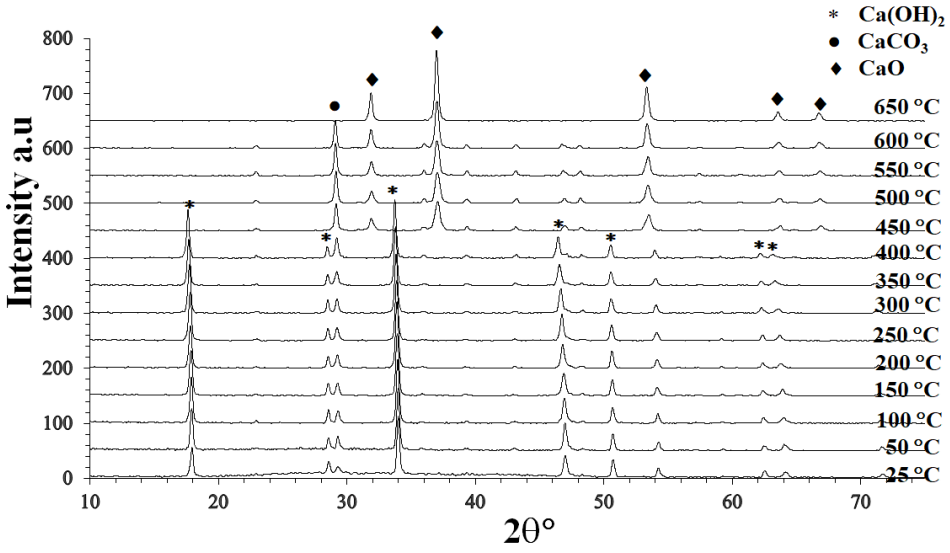

(b)

Figure C1: XRD diffractograms of CaO during its calcination steps in the temperature range of 25 - 650 ºC(a) calcination under vacuum (b) calcination in air

2.2. Recrystallization upon calcination. The crystallite sizes of CaO nano-particles calcined under vacuum go through a maximum at 550 °C due to their recrystallization to eliminate lattice defects and dislocations, as seen in Figure C2a. However, this maximum is not present for the case when CaO was obtained by calcination in air, as in this case, CaO is not re-crystallized, as seen in Figure C2.b.

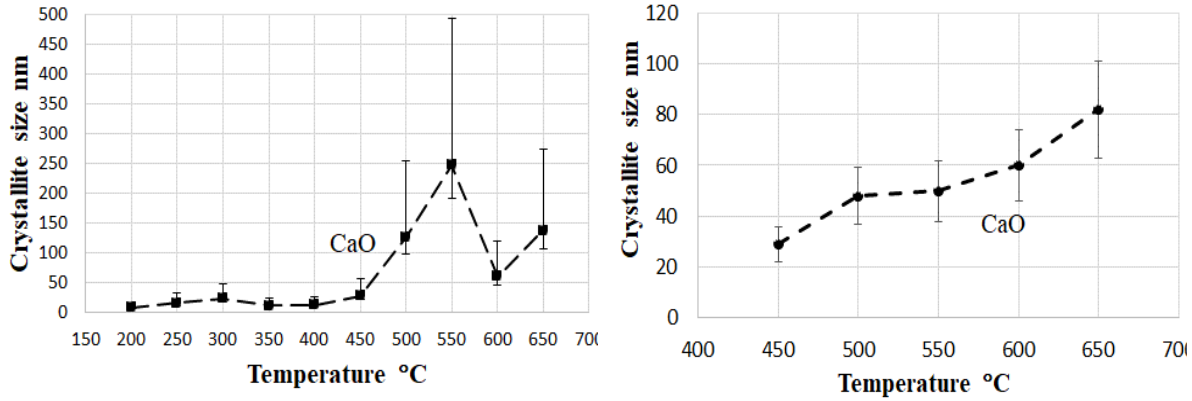

Figure C2: The crystallite sizes of CaO as a function of temperatures in the range of 50 - 650 °C (a) calcination under vacuum (b) calcination in air

2.3. Final sizes after calcination at 650 °C. The final crystallite sizes of CaO nano-particles obtained after calcination at 650 °C were found to be in the range of 60-100 nm. The final crystallite sizes of CaO nano-particles obtained after calcination at 650 °C were found to be in the range of 110-170 nm as seen in Figure C2. The crystallite size of CaO calcination in air leads to the smaller crystallite sizes to compare calcination under vacuum.

Claim 3. Synthesis of metal oxides nanoparticles by calcination in air

3.1. Synthesis of further pure metal oxide nano-particles. To confirm claim 1.1 further, in addition to CaO nano-particles reported in Claim 2, three further types of nano-metal-oxide-particles were successfully synthesized from the list of the 13 possible nano- metal-oxide-particles of Claim 1.1 using the above-described technology and calcination in air (with their average crystallite sizes measured by XRD): Co_3O_4 (18 nm), Fe_2O_3 (16 nm) and NiO (20 nm). TEM micrographs are in good agreement with the crystallite sizes obtained by XRD. The formation of pure and single phases was also confirmed by XRD, as seen in Figure C3.

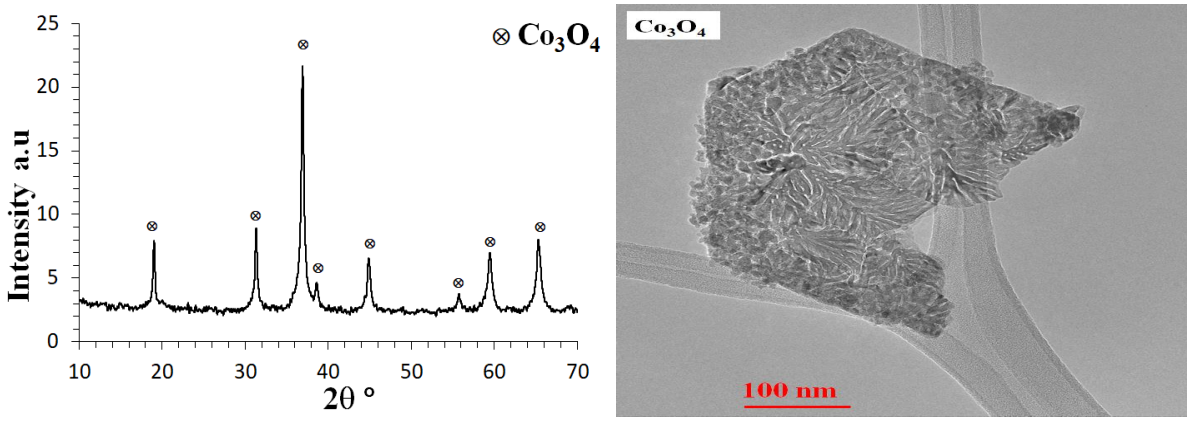

(a)

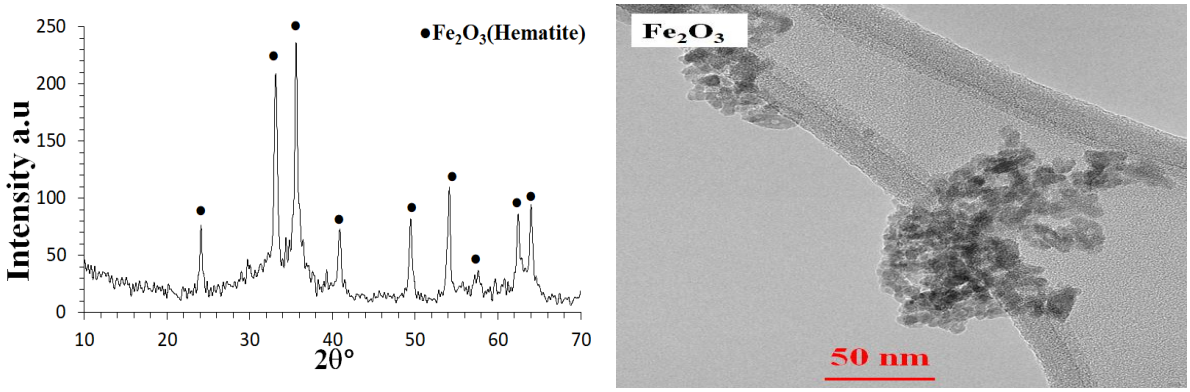

(b)

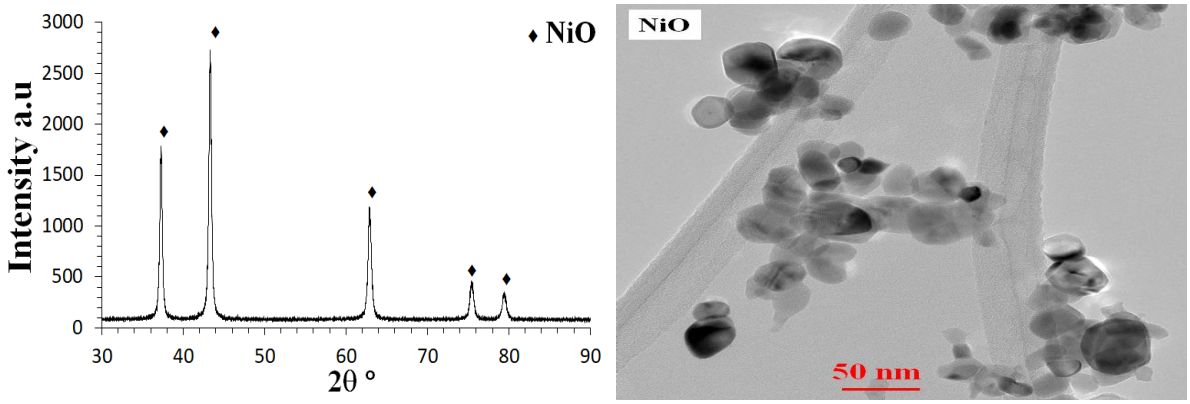

(c)

Figure C3: The XRD diffractograms and TEM micrographs of the pure metal oxides (a) Co_3O_4 (b) Fe_2O_3 (c) NiO

3.2. Synthesis of low-doped CaO. Applying 0.1:1 molar ratio of $NiCl_2$, $CoCl_2$ and $FeCl_3$ to calcium chloride in the initial aqueous solution, low-doped CaO nano-particles were obtained by calcination in air at 650 °C as follows, with their average crystallite sizes: (i) in the 0.1NiO:CaO sample only CaO (42 nm) and NiO (12 nm) phases were detected; (ii) in the 0.1CoO:CaO sample CaO (105 nm) and $Ca_2Co_2O_5$ (50 nm) phases were detected, the latter due

to further oxidation of CoO in air and its complex formation with CaO; (iii) in the $0.05Fe_2O_3$:CaO sample CaO (165 nm), Fe_2O_3 (810 nm) and $Ca_2Fe_2O_5$ (14 nm) phases were detected, the latter due to the complex formation of Fe_2O_3 with CaO as seen in Figure C4.

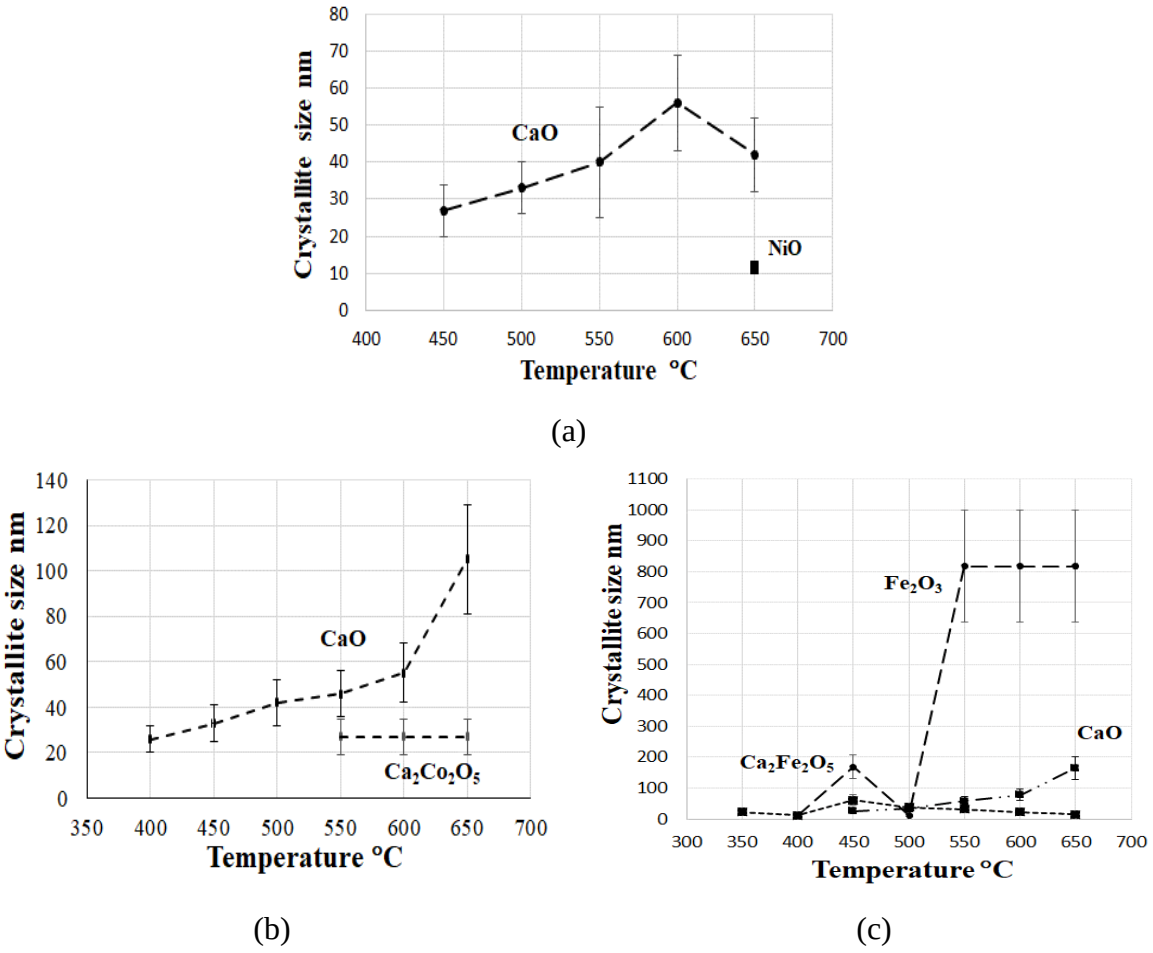

Figure C4: The crystallite sizes of low-doped CaO as a function of temperatures in the range of 50 - 650 °C (a) 0.1NiO:CaO (b) 0.1CoO:CaO (c) $0.05Fe_2O_3$:CaO

3.3. Synthesis of highly-doped CaO. Applying 0.5:1 molar ratio of $NiCl_2$, $CoCl_2$ and $FeCl_3$ to calcium chloride in the initial aqueous solution, highly doped CaO nanoparticles were obtained by calcination in air at 650 °C as follows, with the average crystallite sizes: (i) in the 0.5NiO:CaO sample only CaO (200 nm) and NiO (20 nm) phases were detected; (ii) in the 0.5CoO:CaO sample CaO (120 nm) and $Ca_2Co_2O_5$ (40 nm) are the major phases; (iii) in the $0.25Fe_2O_3$:CaO sample CaO (820 nm) and $Ca_2Fe_2O_5$ (30 nm) phases were detected as seen in Figure C5.

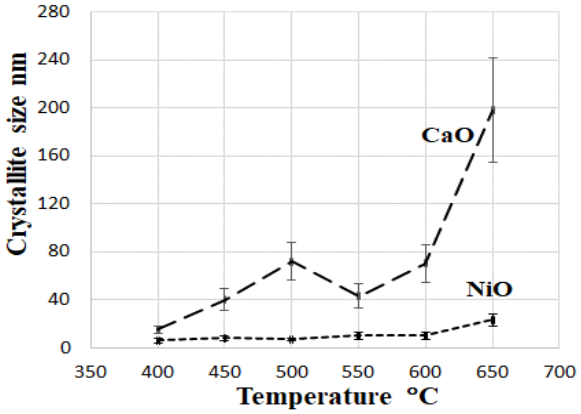

(a)

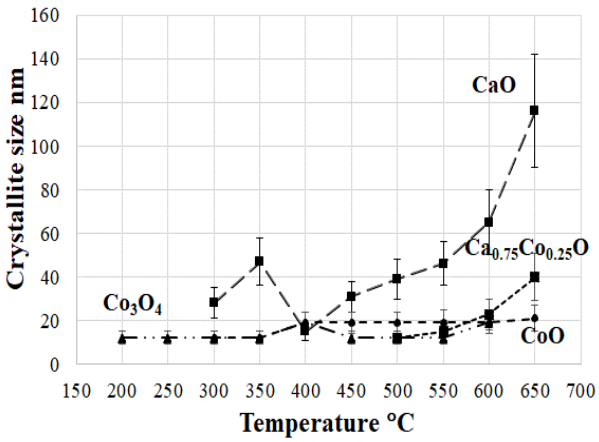

(b)

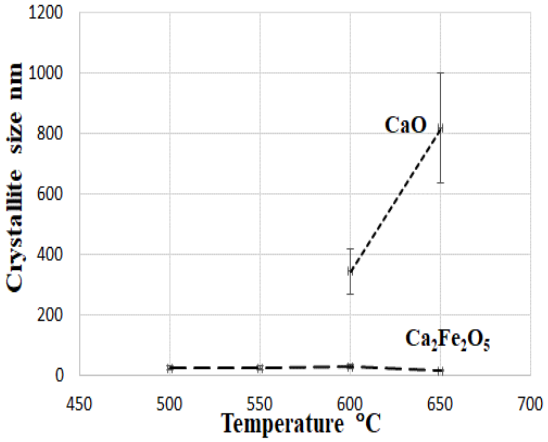

(c)

Figure C5: The crystallite sizes of low-doped CaO as a function of temperatures in the range of 50 - 650 °C (a) 0.5NiO:CaO (b) 0.5CoO:CaO (c) $0.25Fe_2O_3$:CaO

Claim 4. Carbonation capacity of metal oxide nanoparticles kept in air

4.1. Carbonation capacity of pure CaO nano-particles at room temperature. Pure CaO nano-particles are able to absorb carbon dioxide from normal air at room temperature 25 °C to their full capacity within 450 hours; in this process, the initial pure CaO is fully transformed into $CaCO_3$ and its initial mass is increased to its theoretical maximum by 78 %. Similar (but somewhat lower) results were obtained at 0 °C, as seen in Figure C6.

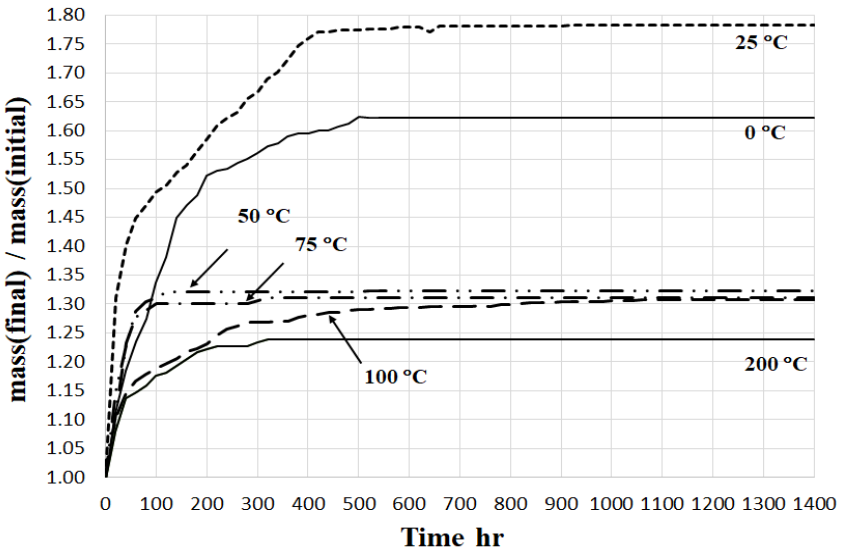

Figure C6: The time dependence of the relative mass change of pure CaO samples exposed to air at different temperatures

4.2. Carbonation capacity of pure CaO nano-particles at higher temperatures. Pure CaO nano-particles at 50 – 75 – 100 – 200 °C were found to absorb much less of carbon dioxide from air compared to room temperature absorption experiments. This was due to the co-absorption of water vapor with the co-formation of $Ca(OH)_2$, blocking the pores in the CaO nano-structure.

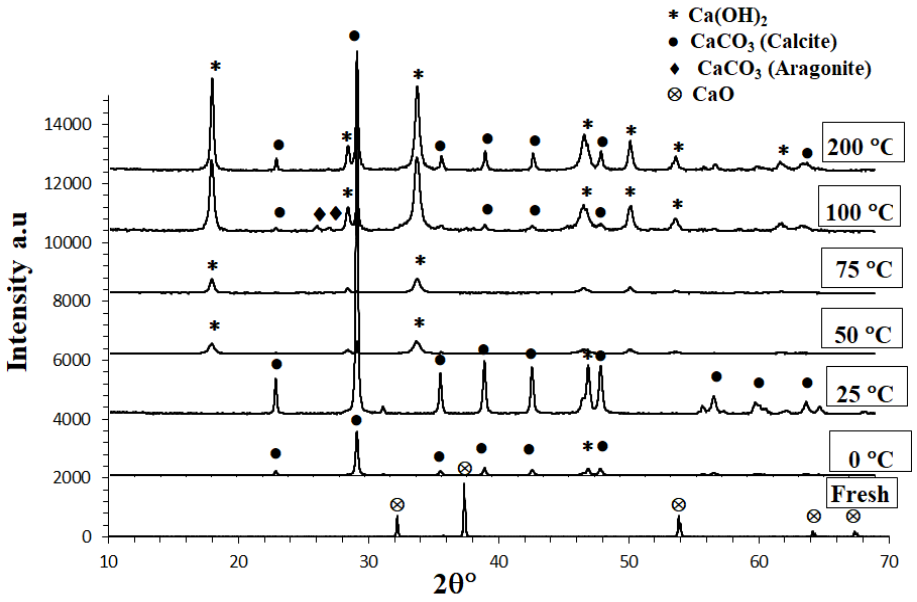

Figure C7: The XRD diffractograms of pure CaO, fresh sample and after the measurements of the sample exposed to air at different temperatures

4.3. The role of doping oxides in carbonation. All doping oxides (NiO, Fe_2O_3 and Co_3O_4) in both low-doped and highly-doped states with CaO were found inactive towards capturing CO_2 or H_2O from normal air in the temperature range of 0 … 200 °C. This was proven by the absence of any peaks for carbonates or hydrates of Ni, Co and Fe in doped CaO samples after they were kept in normal air for hundreds of hours as seen in Figures C8 and C9. In these samples, the same $CaCO_3$ was detected at 0 … 25 °C and additionally, some $Ca(OH)_2$ was found at 50 … 200 °C, as shown above for pure CaO samples. As a result, the carbonation capacity of doped CaO samples was lower compared to pure CaO samples, as the doping oxides had only some diluting effect.

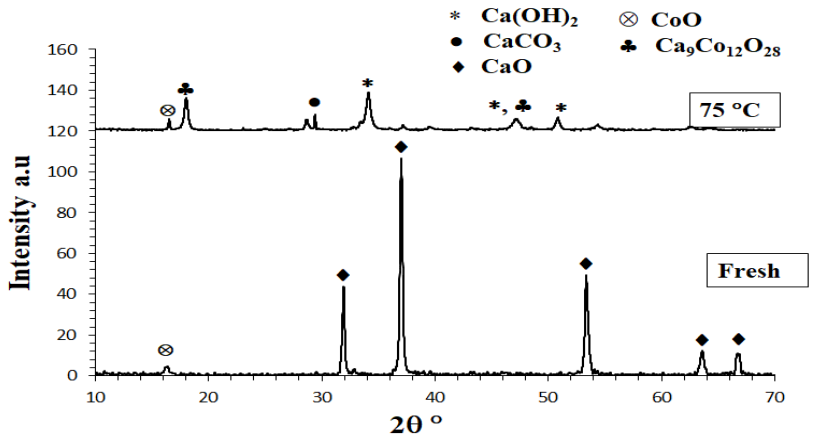

(a)

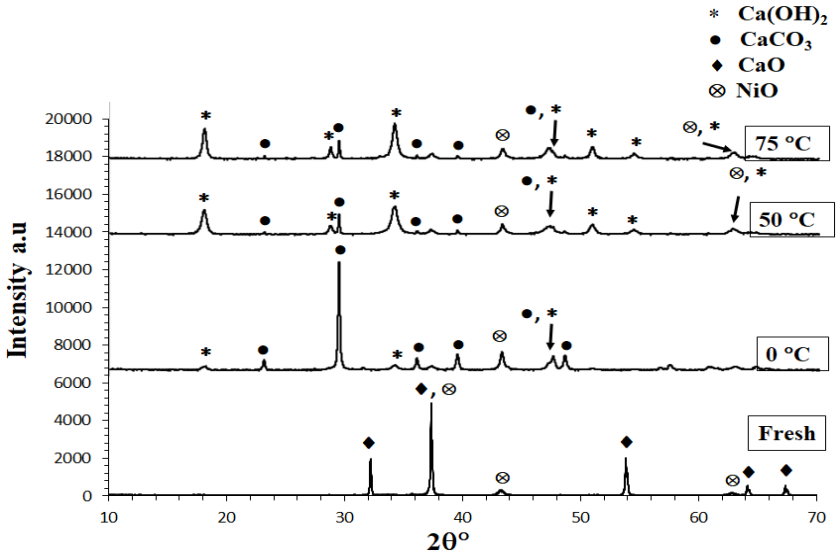

(b)

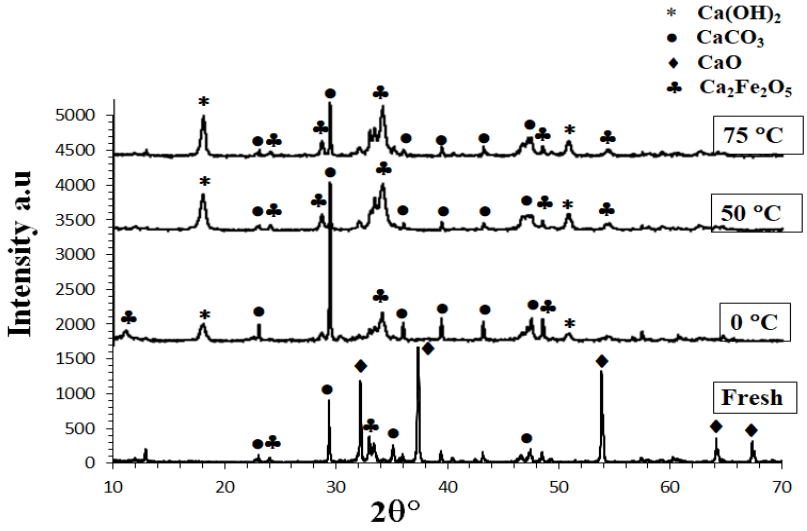

(c)

Figure C8: The XRD diffractograms of low-doped CaO fresh sample and after the measurements of the samples exposed to air at different temperatures (a) 0.1CoO:CaO (b) 0.1NiO:CaO and (c) 0.05Fe_2O_3:CaO

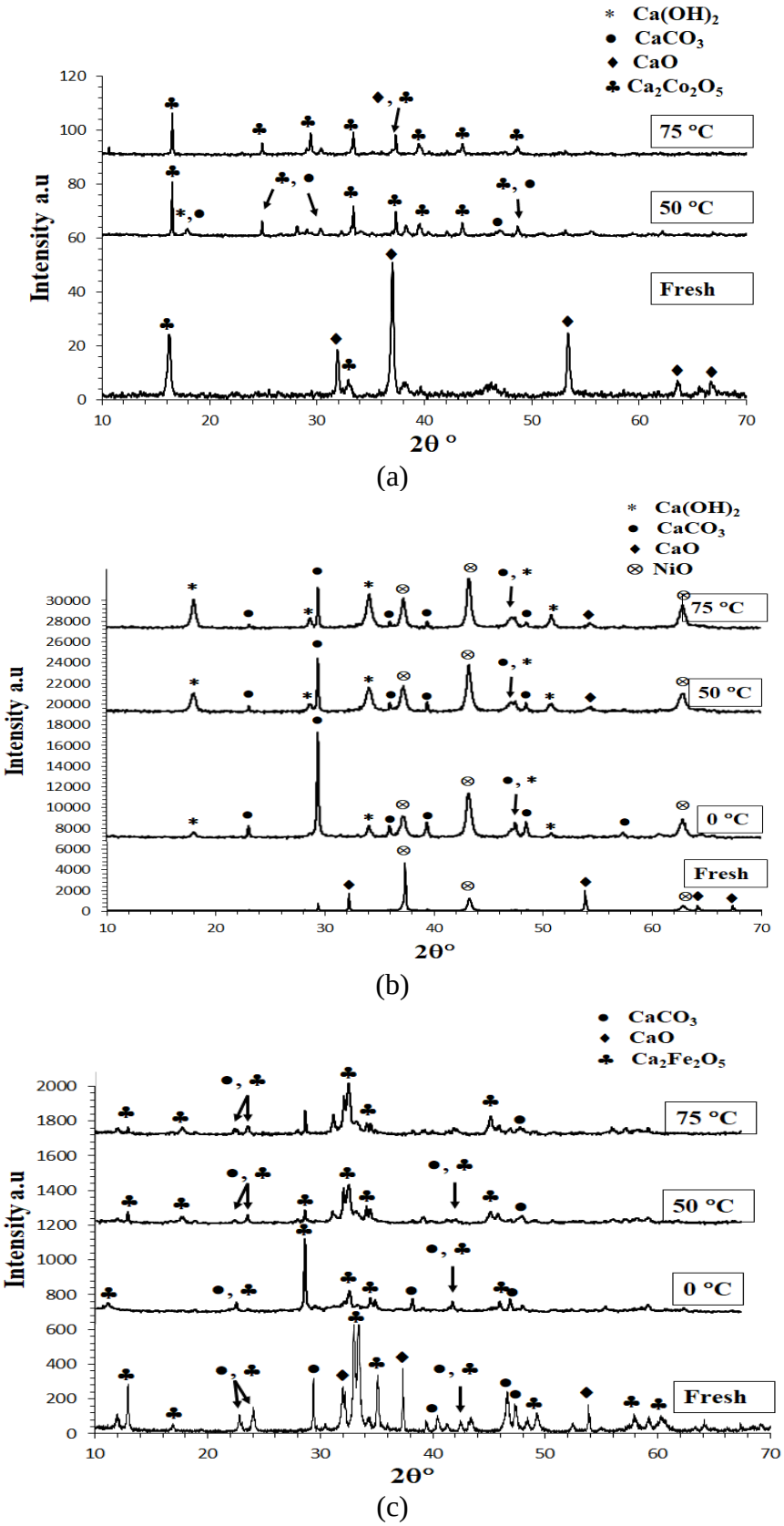

Figure C9: The XRD diffractograms of highly-doped CaO fresh sample and after the measurements of the samples exposed to air at different temperatures (a) 0.5CoO:CaO (b) 0.5NiO:CaO and (c) 0.25Fe_2O_3:CaO

4.4. Final absorbent selection for carbon dioxide capture. Among all nano-metal oxide synthesized and all capturing temperatures studied, pure CaO at 25 °C in air showed the maximum carbon dioxide capturing capacity. Although it takes a longer time (around 450 hours) to fully carbonate pure CaO at 25 °C, it does not require special industrial conditions; capturing of carbon dioxide from normal air will take place slowly but surely by CaO disposed to open fields at a temperature around room temperature.

Future Perspectives

- It would be interesting from a theoretical point of view to predict the numbers of the possible candidates that can be used to produce metal oxide nanoparticles through precipitation-calcination methods using other precursors such as metal nitrate, metal sulfate and NaOH or KOH.

- The reaction conditions for the synthesis of metal oxides nanoparticle via the precipitation calcination method, such as speed of magnetic stirring, duration of the chemical reaction and calcination temperature, could be optimized to produce metal oxide nanoparticles with better characteristics.

- The capturing process should be investigated in CO_2 environment at low temperatures to analyze the capturing efficiency of the metal oxides and metal oxides doped CaO nanoparticles.

- Based on the results from this research, the produced CaO and metal oxides doped CaO could be used in various industrial production as CO_2 absorbers.

Acknowledgement

I would like to express my sincere gratitude and appreciation to all these respectful persons. Without them, my PhD journey will not be straightforward to complete. First of all, I would like to express my sincere and deepest appreciation to my supervisors Prof. Dr. George Kaptay and Prof. Dr. Peter Baumli. Their guidance, giving the lectures to fulfil the knowledge and support for my research direction and experimentation made my study journey more academically structured.

Moreover, I would like to thank Dr. Ference Kristaly for his assistance with XRD investigations, giving us lectures on XRD subjects, and especially huge support and suggestions for both my publications and my experimental work. I would like to thank Dr. Andrea Simon, who reviewed my work. I am always thankful to Dr. Anna Sycheva and

Dr. Daniel Koncs-Horvath for SEM investigations, Mr. Gabor Karacs for TEM investigations, Mr. Tibor Ferenczi for BET investigations, Dr. Veres Zsolt for helping me to use the furnace.

I would like to express my sincere gratitude to Ms. Agnes Solczi not only for being our faculty coordinator and handling all the administrative work with responsibility but also for her encouragement and support of any inconvenient issues during my entire stay in Hungary. I would like to thank Mrs. Aniko Zoltanne Markus and Mrs. Napsugar Bodnarne Nyari for helping during my experimental work more convenient.

I would like to express my appreciation to Tempus Public Foundation and Stipendium Hungaricum Scholarship Programme for giving me the opportunity to study and providing financial support for my entire stay in Hungary. I would like to extend my gratitude to the Institute of Physical Metallurgy, Metal Forming and Nanotechnology and Antal Kerpely Doctoral School of Materials Science and Technology (Faculty of Material Science and Engineering) at the University of Miskolc. This research work was financed by GINOP2.3.2-15-2016-0027 “Sustainable operation of the workshop of excellence for the research and development of crystalline and amorphous nanostructured materials” project implemented in the framework of Szechenyi 2020 program. The realization of this work was supported by the European Union. I would like to thank the Head of the doctoral school, Professor Dr. Valeria Mertinger, for providing me with the necessary equipment and giving us the lectures for the XRD subject.

I would like to thank both Hungarian and International students for helping and supporting my research work. I would like to thank my close colleagues Jamal Eldin Fadoul Mohammed Ibrahim as well as my seniors Dr. Kanokon Nuilek and Dr. Patcharapon Somedee, who recently graduated, for their encouragement, understanding, and support throughout my PhD journey.

Finally, I am grateful to my parents and my siblings for their continuous support and motivation throughout my entire life.

References

[1] A. Nazari, S. Riahi, S. Riahi, S. Fatemeh Shamekhi, and A. Khademno, "Mechanical properties of cement mortar with Al_2O_3 nanoparticles," J. Am. Sci., vol. 6, no. 4, pp. 94–97, 2009.

[2] S. Stankic, S. Suman, F. Haque, and J. Vidic, "Pure and multi metal oxide nanoparticles: Synthesis, antibacterial and cytotoxic properties," J. Nanobiotechnology, vol. 14, no. 1, pp. 1–20, 2016, doi: 10.1186/s12951-016-0225-6.

[3] L. Habte, N. Shiferaw, D. Mulatu, T. Thenepalli, R. Chilakala, and J. W. Ahn, "Synthesis of nano-calcium oxide fromwaste eggshell by sol-gel method," Sustain., vol. 11, no. 11, pp. 1–10, 2019, doi: 10.3390/su11113196.

[4] M. A. Aseel, F. H. Itab, and F. M. Ahmed, "Producing High Purity of Metal Oxide Nano Structural Using Simple Chemical Method," J. Phys. Conf. Ser., vol. 1032, no. 1, 2018, doi: 10.1088/1742-6596/1032/1/012036.

[5] S. Jha, R. Singh, A. Pandey, and S. Tripathi, "Bacterial Toxicological Assay of Calcium Oxide Nanoparticles against some Plant Growth Promoting Rhizobacteria," International J for res in applied sci and eng tech(IJRASET),ISSN 2321-9653, vol. 6, no. 11, 2018.

[6] R. Mohadi, K. Anggraini, F. Riyanti, and A. Lesbani, "Preparation Calcium Oxide From Chicken Eggshells," Sriwij. J. Environ., vol. 1, no. 2, pp. 32–35, 2016, doi: 10.22135/sje.2016.1.2.32-35.

[7] Z. X. Tang, D. Claveau, R. Corcuff, K. Belkacemi, and J. Arul, "Preparation of nano-CaO using thermal-decomposition method," Mater. Lett., vol. 62, no. 14, pp. 2096–2098, 2008, doi: 10.1016/j.matlet.2007.11.053.

[8] P. Jamrunroj, S. Wongsakulphasatch, A. Maneedaeng, C. K. Cheng, and S. Assabumrungrat, "Surfactant assisted CaO-based sorbent synthesis and their application to high-temperature CO_2 capture," Powder Technol., vol. 344, pp. 208–221, 2019, doi: 10.1016/j.powtec.2018.12.011.

[9] M. Sadeghi and M. H. Husseini, "A Novel Method for the Synthesis of CaO Nanoparticle for the Decomposition of Sulfurous Pollutant," J. Appl. Chem. Res., vol. 7, no. 4, pp. 39–49, 2013.

[10] A. J. Szalai, N. Manivannan, and G. Kaptay, "Super-paramagnetic magnetite nanoparticles obtained by different synthesis and separation methods stabilized by biocompatible coatings," Colloids Surfaces A Physicochem. Eng. Asp., vol. 568, pp. 113–122, 2019, doi: 10.1016/j.colsurfa.2019.02.006.

[11] J. Gupta and M. Agarwal, "Preparation and characterizaton of CaO nanoparticle for biodiesel production," AIP Conf. Proc., vol. 1724, 2016, doi: 10.1063/1.4945186.

[12] A. Roy and J. Bhattacharya, "Microwave assisted synthesis of CaO nanoparticles and use in waste water treatment " NSTI-Nanotech 2011, vol. 3, no. 1, pp. 565–568, 2011.

[13] Z. X. Tang, Z. Yu, Z. L. Zhang, X. Y. Zhang, Q. Q. Pan, and L. E. Shi, "Sonication-assisted preparation of CaO nanoparticles for antibacterial agents," Quim. Nova, vol. 36, no. 7, pp. 933–936, 2013, doi: 10.1590/S0100-40422013000700002.

[14] S. A. Salaudeen, B. Acharya, and A. Dutta, "CaO-based CO_2 sorbents: A review on screening, enhancement, cyclic stability, regeneration and kinetics modelling," J. CO_2 Util., vol. 23, pp. 179–199, 2018, doi: 10.1016/j.jcou.2017.11.012.

[15] H. Sun, C. Wu, B. Shen, X. Zhang, Y. Zhang, and J. Huang, "Progress in the development and application of CaO-based adsorbents for CO_2 capture—a review," Mater. Today Sustain., vol. 1–2, pp. 1–27, 2018, doi: 10.1016/j.mtsust.2018.08.001.

[16] P. Bharti, B. Singh, and R. K. Dey, “Process optimization of biodiesel production catalyzed by CaO nanocatalyst using response surface methodology,” J. Nanostructure Chem., vol. 9, no. 4, pp. 269–280, 2019, doi: 10.1007/s40097-019-00317-w.
[17] I. B. Banković-Ilić, M. R. Miladinović, O. S. Stamenković, and V. B. Veljković, “Application of nano CaO–based catalysts in biodiesel synthesis,” Renew. Sustain. Energy Rev., vol. 72, pp. 746–760, 2017, doi: 10.1016/j.rser.2017.01.076.
[18] K. Colombo, L. Ender, and A. A. C. Barros, “The study of biodiesel production using CaO as a heterogeneous catalytic reaction,” Egypt. J. Pet., vol. 26, no. 2, pp. 341–349, 2017, doi: 10.1016/j.ejpe.2016.05.006.
[19] Y. Zhang, X. Gong, X. Chen, L. Yin, J. Zhang, and W. Liu, “Performance of synthetic CaO-based sorbent pellets for CO_2 capture and kinetic analysis,” Fuel, vol. 232, pp. 205–214, 2018, doi: 10.1016/j.fuel.2018.05.143.
[20] J. Sun et al., “Stabilized CO_2 capture performance of extruded-spheronized CaO-based pellets by microalgae templating,” Proc. Combust. Inst., vol. 36, no. 3, pp. 3977–3984, 2017, doi: 10.1016/j.proci.2016.09.001.
[21] E. Arul, K. Raja, S. Krishnan, K. Sivaji, and S. J. Das, “Bio-Directed Synthesis of Calcium Oxide (CaO) Nanoparticles Extracted from Limestone Using Honey,” J. Nanosci. Nanotechnol., vol. 18, no. 8, pp. 5790–5793, 2018, doi: 10.1166/jnn.2018.15386.
[22] A. Benedetti, J. Ilavsky, C. Segre, and M. Strumendo, “Analysis of textural properties of CaO-based CO_2 sorbents by ex situ USAXS,” Chem. Eng. J., vol. 355, pp. 760–776, 2019, doi: 10.1016/j.cej.2018.07.164.
[23] X. Ma, Y. Li, X. Yan, W. Zhang, J. Zhao, and Z. Wang, “Preparation of a morph-genetic CaO-based sorbent using paper fibre as a biotemplate for enhanced CO_2 capture,” Chem. Eng. J., vol. 361, no. October 2018, pp. 235–244, 2019, doi: 10.1016/j.cej.2018.12.061.
[24] B. Zhao, L. Ma, H. Shi, K. Liu, and J. Zhang, “Calcium precursor from stirring processes at room temperature for controllable preparation of nano-structure CaO sorbents for high-temperature CO_2 adsorption,” J. CO_2 Util., vol. 25, pp. 315–322, 2018, doi: 10.1016/ j.jcou.2018.04.012.
[25] A. Granados-Pichardo, F. Granados-Correa, V. Sánchez-Mendieta, and H. Hernández-Mendoza, “New CaO-based adsorbents prepared by solution combustion and high-energy ball-milling processes for CO_2 adsorption: Textural and structural influences,” Arab. J. Chem., vol. 13, no. 1, pp. 171–183, 2020, doi: 10.1016/j.arabjc.2017.03.005.
[26] F. Donat and C. R. Müller, “A critical assessment of the testing conditions of CaO-based CO_2 sorbents,” Chem. Eng. J., vol. 336, pp. 544–549, 2018. doi: 10.1016/j.cej.2017.12.050.
[27] B. Azimi, M. Tahmasebpoor, P. E. Sanchez-Jimenez, A. Perejon, and J. M. Valverde, “Multicycle CO_2 capture activity and fluidizability of Al-based synthesized CaO sorbents,” Chem. Eng. J., vol. 358, pp. 679–690, 2019, doi: 10.1016/j.cej.2018.10.061.
[28] W. Liu et al., “Performance enhancement of calcium oxide sorbents for cyclic CO_2 capture-a review,” Energy and Fuels, vol. 26, no. 5, pp. 2751–2767, 2012, doi: 10.1021/ef300220x.
[29] D. Kulkarni and I. E. Wachs, “Isopropanol oxidation by pure metal oxide catalysts: Number of active surface sites and turnover frequencies,” Appl. Catal. A Gen., vol. 237, no. 1–2, pp. 121–137, 2002, doi: 10.1016/S0926-860X(02)00325-3.
[30] A. R. Butt, S. Ejaz, J. C. Baron, M. Ikram, and S. Ali, “CaO nanoparticles as a potential drug delivery agent for biomedical applications,” Dig. J. Nanomater. Biostructures, vol. 10, no. 3, pp. 799–809, 2015.

[31] H. Chen, N. Khalili, and J. Li, “Development of stabilized Ca-based CO_2 sorbents supported by fly ash,” Chem. Eng. J., vol. 345, pp. 312–319, 2018, doi: 10.1016/j.cej.2018.03.162.
[32] A. Z. Ziva, Y. K. Suryana, Y. S. Kurniadianti, A. Bayu, D. Nandiyanto, and T. Kurniawan, “Recent Progress on the Production of Aluminum Oxide (Al_2O_3) Nanoparticles : A Review,” Mechanical Engineering for Society and Industry, vol. 1, no. 2, pp. 54–77, 2021.
[33] H. Zhang et al., “Solvent-free hydrothermal synthesis of gamma-aluminum oxide nanoparticles with selective adsorption of Congo red,” J. Colloid Interface Sci., vol. 536, pp. 180–188, 2019, doi: 10.1016/j.jcis.2018.10.054.
[34] T. Miyazaki et al., “Interaction of the surface of BeO with water: In connection with the two-dimensional condensation of water,” J. Colloid Interface Sci., vol. 106, no. 1, pp. 154–160, 1985, doi: 10.1016/0021-9797(85)90391-1.
[35] V. Selvaraj, B. Morri, L. M. Nair, and H. Krishnan, “Experimental investigation on the thermophysical properties of beryllium oxide-based nanofluid and nano-enhanced phase change material,” J. Therm. Anal. Calorim., vol. 137, no. 5, pp. 1527–1536, 2019. doi: 10.1007/ s10973-019-08042-w.
[36] E. S. Funston, W. J. Kirkpatrick, and P. P. Turner, “Preparation of high purity BeO powder,” J. Nucl. Mater., vol. 11, no. 3, pp. 310–319, 1964, doi: 10.1016/0022-3115(64)90022-4.
[37] X. F. Wang, R. C. Wang, C. Q. Peng, T. T. Li, and B. Liu, “Synthesis and sintering of beryllium oxide nanoparticles,” Prog. Nat. Sci. Mater. Int., vol. 20, no. 1, pp. 81–86, 2010, doi: 10.1016/s1002-0071(12)60011-2.
[38] Quirk, J. F., N. B. Mosley, and W. H. Duckworth. "Characterization of sinterable oxide powders: I, BeO." Journal of the American Ceramic Society, vol. 40, no. 12, pp 416-419, 1957. https://doi.org/10.1111/j.1151-2916.1957.tb12565.x
[39] M. Ghiasi and A. Malekzadeh, “Synthesis of $CaCO_3$ nanoparticles via citrate method and sequential preparation of CaO and $Ca(OH)_2$ nanoparticles,” Cryst. Res. Technol., vol. 47, no. 4, pp. 471–478, 2012, doi: 10.1002/crat.201100240.
[40] N. N. Hlaing et al., “Sol-gel hydrothermal synthesis of microstructured CaO-based adsorbents for CO_2 capture,” RSC Adv., vol. 5, no. 8, pp. 6051–6060, 2015. doi: 10.1039/c4ra14355h.
[41] G. Patel, U. Pal, and S. Menon, “Removal of fluoride from aqueous solution by CaO nanoparticles,” Sep. Sci. Technol., vol. 44, no. 12, pp. 2806–2826, 2009. doi: 10.1080/01496390903014425.
[42] S. Cheraghi, M. A. Taher, and H. Karimi-Maleh, “A Novel Strategy for Determination of Paracetamol in the Presence of Morphine Using a Carbon Paste Electrode Modified with CdO Nanoparticles and Ionic Liquids,” Electroanalysis, vol. 28, no. 2, pp. 366–371, 2016, doi: 10.1002/elan.201500357.
[43] S. Balamurugan et al., “Synthesis of CdO nanopowders by a simple soft chemical method and evaluation of their antimicrobial activities,” Pacific Sci. Rev. A Nat. Sci. Eng., vol. 18, no. 3, pp. 228–232, 2016, doi: 10.1016/j.psra.2016.10.003.
[44] R. Ranjithkumar, A. Albert Irudayaraj, G. Jayakumar, A. Dhayal Raj, S. Karthick, and R. Vinayagamoorthy, “Synthesis and Properties of CdO and Fe doped CdO Nanoparticles,” Mater. Today Proc., vol. 3, no. 6, pp. 1378–1382, 2016, doi: 10.1016/j.matpr.2016.04.018.
[45] S. Kaveh, B. Norouzi, N. Nami, and A. Mirabi, “Phytochemical synthesis of CdO nanoparticles: fabrication of electrochemical sensor for quantification of cefixime,” J. Mater. Sci. Mater. Electron., vol. 32, no. 7, pp. 8932–8943, 2021, doi: 10.1007/s10854-021-05564-8.

[46] T. Athar, S. S. M. Shafi, and A. A. Khan, “Soft Chemical Process for Synthesis of CdO Nanoparticles,” Mater. Focus, vol. 3, no. 5, pp. 397–400, 2014, doi: 10.1166/ mat.2014.1194.
[47] N. Thovhogi, E. Park, E. Manikandan, M. Maaza, and A. Gurib-Fakim, “Physical properties of CdO nanoparticles synthesized by green chemistry via Hibiscus Sabdariffa flower extract,” J. Alloys Compd., vol. 655, pp. 314–320, 2016, doi: 10.1016/ j.jallcom. 2015.09.063.
[48] G. Somasundaram, J. Rajan, P. Sangaiya, and R. Dilip, “Hydrothermal synthesis of CdO nanoparticles for photocatalytic and antimicrobial activities,” Results Mater., vol. 4, p. 100044, 2019, doi: 10.1016/j.rinma.2019.100044.
[49] K. Sinkó, G. Szabó, and M. Zrínyi, “Liquid-phase synthesis of cobalt oxide nanoparticles,” J. Nanosci. Nanotechnol., vol. 11, no. 5, pp. 4127–4135, 2011. doi: 10.1166/jnn.2011.3875.
[50] M. S. Samuel et al., “Green synthesis of cobalt-oxide nanoparticle using jumbo Muscadine (Vitis rotundifolia): Characterization and photo-catalytic activity of acid Blue-74,” J. Photochem. Photobiol. B Biol., vol. 211, p. 112011, 2020. doi: 10.1016/j.jphotobiol. 2020.112011.
[51] S.J. Mammadyarova, “Synthesis and Characterization of Cobalt Oxide Nanostructures A Brief Review,” Azerbaijan Chem. J., vol. 1841, pp. 80–93, 2021, doi: doi.org/ 10.32737/0005-2531-2021-2-80-93.
[52] F. Buckley and G. Hope, “Electroless deposition of Ag thin films,” Proc. 2006 Int. Conf. Nanosci. Nanotechnology, ICONN, pp. 528–531, 2006, doi: 10.1109/ICONN. 2006.340670.
[53] A. Benchettara and A. Benchettara, “Electrochemical Sensor Based on Nanoparticles of Cobalt Oxides for Determination of Glucose,” Mater. Today Proc., vol. 2, no. 8, pp. 4212–4216, 2015, doi: 10.1016/j.matpr.2015.09.005.
[54] R. Shende, S. Subramanian, S. Hasan, S. Apperson, and R. Thiruvengadathan, “Nanoenergetic Composites of CuO Nanorods , Nanowires , and Al-nanoparticles” Propellants, Explosives, Pyrotechnics: An International Journal Dealing with Scientific and Technological Aspects of Energetic Material, vol. 2, no. 2, pp. 122–130, 2008, doi: 10.1002/prep.200800212.
[55] Wang, W., Liu, Z., Liu, Y., Xu, C., Zheng, C., & Wang, G, “A simple wet-chemical synthesis and characterization of CuO nanorods. Applied Physics A, vol.7, no. 3, p-417-420, 2003. doi: 10.1007/s00339-002-1514-5.
[56] S. K. Das, J. Khandaker, and F. Ahmed, “Hydrothermal Synthesis of CuO Nanoparticles and A Study on Property Hydrothermal Synthesis Of CuO Nanoparticles And A Study On Property,” Journal of Applied and Fundamental Sciences, vol. 6, no. 2, p- 52. 2020.
[57] L. Armelao, D. Barreca, M. Bertapelle, G. Bottaro, and C. Sada, “A sol – gel approach to nanophasic copper oxide thin films,” Thin solid films, vol. 442, no. 03, pp. 48–52, 2003, doi: 10.1016/S0040-6090(03)00940-4.
[58] Y. Aparna, K. V. E. Rao, and P. S. Subbarao, “Synthesis and Characterization of CuO Nano Particles by Novel Sol-Gel Method,” In Proceedings of the 2nd International Conference on Environment Science and Biotechnology, vol. 48, pp. 156-160, 2012, doi: 10.7763/IPCBEE.
[59] Y. Al-douri, N. Amrane, and M. Rafie, “Annealing temperature effect on structural and optical investigations of Fe_2O_3 nanostructure,” Integr. Med. Res., vol. 8, no. 2, pp. 2164–2169, 2019, doi: 10.1016/j.jmrt.2019.02.004.
[60] S. Hu, L. Jiang, B. Wang, and Y. Ma, “Enhanced electrocatalytic methanol oxidation properties by photo-assisted Fe_2O_3 nanoplates,” Int. J. Hydrogen Energy, vol. 44, no. 26, pp. 13214–13220, 2019, doi: 10.1016/j.ijhydene.2019.03.178.

[61] J. Hong, F. Yang, and Z. Sun, “Hexagonal bi-pyramid α- Fe_2O_3 microcrystals_ Unusual formation, characterization and application for gas sensing,” J. Alloys Compd., vol. 889, p. 161515, 2021, doi: 10.1016/j.jallcom.2021.161515.
[62] S. Cao, Y. Zhu, M. Ma, L. Li, and L. Zhang, “Hierarchically Nanostructured Magnetic Hollow Spheres of Fe_3O_4 and γ - Fe_2O_3 : Preparation and Potential Application in Drug Delivery,” The Journal of Physical Chemistry C, vol.112, no. 6, pp. 1851–1856, 2008. doi.org/10.1021/jp077468+
[63] Ali, A., Zafar, H., Zia, M., ul Haq, I., Phull, A.R., Ali, J.S. and Hussain, A., "Synthesis, characterization, applications, and challenges of iron oxide nanoparticles" Nanotechnology, science and applications, 9, p.49. pp. 49–67, 2016. doi: 10.2147/NSA.S99986
[64] Fouad, D.E., Zhang, C., El-Didamony, H., Yingnan, L., Mekuria, T.D. and Shah, A.H., “Improved size , morphology and crystallinity of hematite (α - Fe_2O_3) nanoparticles synthesized via the precipitation route using ferric sulfate precursor,” Results Phys., vol. 12, pp. 1253–1261, 2019, doi: 10.1016/j.rinp.2019.01.005.
[65] S. Abinaya, H. P. Kavitha, M. Prakash, and A. Muthukrishnaraj, “Green synthesis of magnesium oxide nanoparticles and its applications : A review,” Sustain. Chem. Pharm., vol. 19, p. 100368, 2021, doi: 10.1016/j.scp.2020.100368.
[66] M. Action et al., “Rhizopus oryzae -Mediated Green Synthesis of Magnesium Oxide Nanoparticles (MgO-NPs): A Promising Tool for Effluent Treatment,” Journal of Fungi, vol. 7, no.5, p.372, 2021. doi.org/10.3390/jof7050372
[67] D. F. Kondakov and V. P. Danilov, “Manufacturing of Magnesium Hydroxide from Natural Magnesium Chloride Sources,” Theoretical Foundations of Chemical Engineering, vol. 41, no. 5, pp. 572–576, 2007, doi: 10.1134/S0040579507050193.
[68] C. Y. Tai, C. Tai, M. Chang, and H. Liu, “Synthesis of Magnesium Hydroxide and Oxide Nanoparticles Using a Spinning Disk Reactor,” Industrial & engineering chemistry research, vol. 46, no. 17, pp. 5536–5541, 2007. doi.org/10.1021/ie060869b
[69] H. Mirzaei and A. Davoodnia, “Microwave Assisted Sol-Gel Synthesis of MgO Nanoparticles and Their Catalytic Activity in the Synthesis of Hantzsch,” Chinese J. Catal., vol. 33, no. 9–10, pp. 1502–1507, 2012, doi: 10.1016/S1872-2067(11)60431-2.
[70] M. M. Imani and M. Safaei, “Optimized Synthesis of Magnesium Oxide Nanoparticles as Bactericidal Agents,” Journal of Nanotechnology ,vol. 2019 , ID 6063832, 2019. doi.org/ 10.1155/2019/6063832
[71] R. Wahab, S. G. Ansari, M. A. Dar, Y. S. Kim, and H. S. Shin, “Synthesis of Magnesium Oxide Nanoparticles by Sol-Gel Process” In Materials Science Forum, vol. 558, pp. 983-986.2007, doi: 10.4028/www.scientific.net/MSF.558-559.983.
[72] K. R. Nemade and S. A. Waghuley, “Synthesis of MgO Nanoparticles by Solvent Mixed Spray Pyrolysis Technique for Optical Investigation,” International Journal of Metals, vol. 2014, ID 389416, p- 4, 2014. doi.org/10.1155/2014/389416
[73] X. Liu, C. Chen, Y. Zhao, and B. Jia, “A Review on the Synthesis of Manganese Oxide Nanomaterials and Their Applications on Lithium-Ion Batteries,” Journal of Nanomaterials vol. 2013, ID 736375 , 2013.https://doi.org/10.1155/2013/736375
[74] M. Ghosh, K. Biswas, A. Sundaresan, and C. N. R. Rao, “MnO and NiO nanoparticles : synthesis and magnetic properties,” Journal of Materials Chemistry, vol. 16, no. 1, pp. 106–111, 2006, doi: 10.1039/b511920k.
[75] T. Ould-ely et al., “Manganese (II) Oxide Nanohexapods : Insight into Controlling the Form of Nanocrystals,” Chemistry of materials 18, no. 7 pp. 1821–1829, 2006. doi.org/10.1021/cm052492q

[76] Z. Liang, Y. Zhu, and X. Hu, “β-Nickel Hydroxide Nanosheets and Their Thermal Decomposition to Nickel Oxide Nanosheets,” The Journal of Physical Chemistry B, vol.108, no. 11, pp. 3488–3491, 2004. doi.org/10.1021/jp037513n
[77] A. A. Mariam et al., “Bio-Synthesis of NiO And Ni Nanoparticles And Their Characterization” Digest Journal of Nanomaterials and Biostructures, vol. 9, no. 3, pp. 1007–1019, 2014.
[78] V. Helan et al., “Neem leaves mediated preparation of NiO nanoparticles and its magnetization, coercivity and antibacterial analysis,” Results Phys., vol. 6, pp. 712–718, 2016, doi: 10.1016/j.rinp.2016.10.005.
[79] Y. Du et al., “Preparation of NiO nanoparticles in microemulsion and its gas sensing performance,” Materials Letters, vol. 68, pp. 168–170, 2012, doi: 10.1016/j.matlet. 2011.10.039.
[80] L. H. Dall, A. Dayse, and I. Santos, “Deposition and photo-induced electrical resistivity of dip-coated NiO thin films from a precipitation process,” Journal of Materials Science: Materials in Electronics, vol. 24, no. 6, pp. 1823–1831, 2013, doi: 10.1007/s10854-012-1019-8.
[81] P. Bera, M. Rajamathi, and M. S. Hegde, “Thermal behaviour of hydroxides , hydroxysalts and hydrotalcites,” Bulletin of Materials Science, vol. 23, no. 2, pp. 141–145, 2000.
[82] M. Salavati-niasari, F. Mohandes, F. Davar, and M. Mazaheri, “Preparation of NiO nanoparticles from metal-organic frameworks via a solid-state decomposition route,” Inorganica Chim. Acta, vol. 362, no. 10, pp. 3691–3697, 2009, doi: 10.1016/ j.ica. 2009.04.025.
[83] Al-Sehemi, Abdullah G., Ayed S. Al-Shihri, Abul Kalam, Gaohui Du, and Tokeer Ahmad. "Microwave synthesis, optical properties and surface area studies of NiO nanoparticles." Journal of Molecular Structure, vol.1058, p-56-61, 2014. doi.org/ 10.1016/ j.molstruc.2013.10.065
[84] M. C. Gao, “Isothermal Decomposition Kinetics of Nickel (II) Hydroxide Powder,” Journal of Alloys and Compounds, vol. 644, pp. 968–974, 2015, doi: 10.1016/ j.jallcom. 2015.03.256.
[85] J. Zhao and Q. Zhang, “Synthesis of $Ni(OH)_2$ Nano flakes Through a Novel Ion Diffusion Method Controlled by Ion Exchange Membrane and Electrochemical Supercapacitive Properties,” Electrochim. Acta, vol. 184, pp. 47–57, 2015, doi: 10.1016/ j.electacta. 2015. 10.029.
[86] B. Cheng, Y. Le, W. Cai, and J. Yu, “Synthesis of hierarchical $Ni(OH)_2$ and NiO nanosheets and their adsorption kinetics and isotherms to Congo red in water,” J. Hazard. Mater., vol. 185, no. 2–3, pp. 889–897, 2011. doi: 10.1016/j.jhazmat. 2010.09.104.
[87] P. Jeevanandam, Y. Koltypin, A. Gedanken, and B. U. V, “Synthesis of Nanosized α-Nickel Hydroxide by a Sonochemical Method,” Nano Letters, vol. 1, no. 5, p-263-266 2001. doi.org/10.1021/nl010003p
[88] H. Zheng and C. G. X. Wang, “Fast synthesis and optical property of SnO nanoparticles from choline chloride-based ionic liquid,” Journal of nanoparticle research, vol. 16, no. 2, p- 1-9, 2014, doi: 10.1007/s11051-014-2288-3.
[89] Jaśkaniec, Sonia, et al. "Solvent engineered synthesis of layered SnO for high-performance anodes." npj 2D Materials and Applications, vol.5, no.1, p-1-9, 2021. doi: 10.1038/s41699-021-00208-1.
[90] P. Boroojerdian, “Structural and Optical Study of SnO Nanoparticles Synthesized Using Microwave – Assisted Hydrothermal Route,” International Journal of Nanoscience and Nanotechnology, vol. 9, no. 2, pp. 95–100, 2013.

[91] J. S. Dias, F. R. M. Batista, R. Bacani, and E. R. Triboni, “Structural characterization of SnO nanoparticles synthesized by the hydrothermal and microwave routes,” Sci. Rep., vol.1, no. 11, pp. 1–11, 2020, doi: 10.1038/s41598-020-66043-4.
[92] H. Youssef and N. M. Ahmed, “Synthesis and Characterization of Nano- / Micro-Crystalline SnO using Microwave and Hydrothermal Techniques,” Journal of Ceramic Science and Technology, vol.5, no. 3, pp. 217–222, 2014, doi: 10.4416/JCST2014-00010.
[93] P. D. Prasad, S. P. Reddy, and A. Deepthi, “Synthesis , Characterization of Tin Oxide (SnO) Nanoparticles via Autoclave synthesis protocol for H_2 sensing,” Int. J. Nanotechnol. App, vol. 11, no. 3, pp. 265–276, 2017.
[94] K. Choi, T. Kang, and S. Oh, “Preparation of disk shaped ZnO particles using surfactant and their PL properties,” Mater. Lett., vol. 75, pp. 240–243, 2012, doi: 10.1016/ j.matlet.2012.02.031.
[95] T. Jesionowski, “Zinc Oxide — From Synthesis to Application: A Review,” Materials 7, no. 4, pp. 2833–2881, 2014, doi: 10.3390/ma7042833.
[96] S. A. H.-T. Taheri-Nassaj, “Economical synthesis of Al_2O_3 nanopowder using a precipitation method,” Mater. Lett., vol. 63, no. 27, pp. 2274–2276, 2009, doi: 10.1016/ j.matlet.2009.07.035.
[97] S. Ali, “Synthesis of γ-alumina (Al_2O_3) nanoparticles and their potential for use as an adsorbent in the removal of methylene blue dye from industrial wastewater." Nanoscale Advances, vol. 1, no. 1, pp. 213–218, 2019, doi: 10.1039/c8na00014j.
[98] S. Wang, X. Li, S. Wang, Y. Li, and Y. Zhai, “Synthesis of γ -alumina via precipitation in ethanol,” Materials Letters, vol. 62, no. 20, pp. 3552–3554, 2008, doi: 10.1016/ j.matlet. 2008.03.048.
[99] V. Altunal, V. Guckan, A. Ozdemir, and Z. Yegingil, “A calcination study on BeO ceramics for radiation dosimetry,” Mater. Res. Bull., vol. 130, p. 110921, 2020, doi: 10.1016/ j.materresbull.2020.110921.
[100] S. Abraham and V. P. Sarathy, “Biomedical Applications of Calcium Oxide Nanoparticles - A Spectroscopic Study,” Int. J. Pharm. Sci. Res., vol. 49, no. 1, pp. 121–125, 2018.
[101] S. M. El-Dafrawy, H. M. Youssef, W. O. Toamah, and M. M. El-Defrawy, “Synthesis of nano-CaO particles and its application for the removal of copper (II), Lead (II), cadmium (II) and iron (III) from aqueous solutions,” Egypt. J. Chem., vol. 58, no. 6, pp. 579–589, 2015, doi: 10.21608/ejchem.2015.1007.
[102] A. T. Ravichandran, A. Robert Xavier, K. Pushpanathan, B. M. Nagabhushana, and R. Chandramohan, “Structural and optical properties of Zn doped CdO nanoparticles synthesized by chemical precipitation method,” J. Mater. Sci. Mater. Electron., vol. 27, no. 3, pp. 2693–2700, 2016, doi: 10.1007/s10854-015-4079-8.
[103] M. Shukla, S. Kumari, S. Shukla, and R. K. Shukla, “Potent antibacterial activity of nano CdO synthesized via microemulsion scheme,” J. Mater. Environ. Sci, vol. 3, no. 4, pp. 678–685, 2012.
[104] A. Das, “Removal of defects in CdO nanoparticle and rapid synthesis of CdO nanoflake using novel microwave technique to improve semiconductor device performance,” Indian J. Sci. Technol., vol. 14, no. 10, pp. 858–868, 2021. doi: 10.17485/ijst/v14i10.1965.
[105] M. M. Durano, A. H. Tamboli, and H. Kim, “Cobalt oxide synthesized using urea precipitation method as catalyst for the hydrolysis of sodium borohydride,” Colloids Surfaces A Physicochem. Eng. Asp., vol. 520, pp. 355–360, 2017, doi: 10.1016 /j.colsurfa. 2017.02.005.

[106] M. R. S. A. Janjua, "Synthesis of Co_3O_4 Nano Aggregates by Co-precipitation Method and its Catalytic and Fuel Additive Applications," Open Chem., vol. 17, no. 1, pp. 865–873, 2019, doi: 10.1515/chem-2019-0100.
[107] K. Phiwdang, S. Suphankij, W. Mekprasart, and W. Pecharapa, "Synthesis of CuO nanoparticles by precipitation method using different precursors," Energy Procedia, vol. 34, pp. 740–745, 2013, doi: 10.1016/j.egypro.2013.06.808.
[108] D. Dozier, S. Palchoudhury, and Y. Bao, "Synthesis of iron oxide nanoparticles with biological coatings," J. Sci. Heal. …, vol.7, pp. 16–18, 2010.
[109] A. Hassanjani-Roshan, M. R. Vaezi, A. Shokuhfar, and Z. Rajabali, "Synthesis of iron oxide nanoparticles via sonochemical method and their characterization," Particuology, vol. 9, no. 1, pp. 95–99, 2011, doi: 10.1016/j.partic.2010.05.013.
[110] Y. Qi, H. Qi, J. Li, and C. Lu, "Synthesis, microstructures and UV-vis absorption properties of β-$Ni(OH)_2$ nanoplates and NiO nanostructures," J. Cryst. Growth, vol. 310, no. 18, pp. 4221–4225, 2008, doi: 10.1016/j.jcrysgro.2008.06.047.
[111] D. Bin Kuang, B. X. Lei, Y. P. Pan, X. Y. Yu, and C. Y. Su, "Fabrication of novel hierarchical β-$Ni(OH)_2$ and NiO microspheres via an easy hydrothermal process," J. Phys. Chem. C, vol. 113, no. 14, pp. 5508–5513, 2009, doi: 10.1021/jp809013g.
[112] A. Huda, C. T. Handoko, M. D. Bustan, B. Yudono, and F. Gulo, "New route in the synthesis of Tin(II) oxide micro-sheets and its thermal transformation," Mater. Lett., vol. 211, pp. 293–295, 2018, doi: 10.1016/j.matlet.2017.10.029.
[113] Rao, U. S., Srinivas, G., & Rao, T. P. "Influence of precursors on morphology and spectroscopic properties of ZnO nanoparticles," Procedia Materials Science, vol. 10, pp- 90-96, 2015. https://doi.org/10.1016/j.mspro.2015.06.029
[114] A. Aimable, M. T. Buscaglia, V. Buscaglia, and P. Bowen, "Polymer-assisted precipitation of ZnO nanoparticles with narrow particle size distribution," J. Eur. Ceram. Soc., vol. 30, no. 2, pp. 591–598, 2010, doi: 10.1016/j.jeurceramsoc.2009.06.010.
[115] Y. Y. Lee, H. S. Jung, J. M. Kim, and Y. T. Kang, "Photocatalytic CO_2 conversion on highly ordered mesoporous materials: Comparisons of metal oxides and compound semiconductors," Appl. Catal. B Environ., vol. 224, pp. 594–601, 2018, doi: 10.1016/ j.apcatb. 2017.10.068.
[116] D. Gong, Z. Zhang, and T. Zhao, "Decay on Cyclic CO_2 Capture Performance of Calcium-Based Sorbents Derived from Wasted Precursors in Multicycles," Energies, vol. 15, no. 9, pp. 1–15, 2022, doi: 10.3390/en15093335.
[117] F. Güleç, W. Meredith, C. G. Sun, and C. E. Snape, "A novel approach to CO_2 capture in Fluid Catalytic Cracking—Chemical Looping Combustion," Fuel, vol. 244, pp. 140–150, 2019. doi: 10.1016/j.fuel.2019.01.168.
[118] A. Antzara, E. Heracleous, and A. A. Lemonidou, "Development of CaO-based mixed oxides as stable sorbents for post-combustion CO_2 capture via carbonate looping," Energy Procedia, vol. 63, pp. 2160–2169, 2014, doi: 10.1016/j.egypro.2014.11.235.
[119] H. Sun et al., "Fundamental studies of carbon capture using CaO-based materials," J. Mater. Chem. A, vol. 7, no. 16, pp. 9977–9987, 2019, doi: 10.1039/c8ta10472g.
[120] A. Hakim et al., "Studies on CO_2 Adsorption and Desorption Properties from Various Types of Iron Oxides (FeO, Fe_2O_3, and Fe_3O_4)," Ind. Eng. Chem. Res., vol. 55, no. 29, pp. 7888–7897, 2016, doi: 10.1021/acs.iecr.5b04091.
[121] J. B. Holquist and D. M. Klaus, "Characterization of potassium superoxide and a novel packed bed configuration for closed environment air revitalization." 44th International Conference on Environmental Systems 2014. http://hdl.handle.net/2346/59647
[122] A. A. Peyghan and S. Yourdkhani, "Capture of carbon dioxide by a nanosized tube of BeO: A DFT study," Struct. Chem., vol. 25, no. 2, pp. 419–426, 2014, doi: 10.1007/ s11224-013-0307-0.

[123] Y. Duan, D. C. Sorescu, and D. Luebke, “Efficient theoretical screening of solid sorbents for CO_2 capture applications,” International Journal of Clean Coal and Energy, vol.1, no. NETL-PUB-318, pp. 661–677, 2011. doi.org/10.4236/ijcce.2012.11001
[124] H. A. Mosqueda, C. Vazquez, P. Bosch, and H. Pfeiffer, “Chemical sorption of carbon dioxide (CO_2) on lithium oxide (Li_2O),” Chem. Mater., vol. 18, no. 9, pp. 2307–2310, 2006, doi: 10.1021/cm060122b.
[125] J. Ortiz-Landeros, T. L. Ávalos-Rendón, C. Gómez-Yáñez, and H. Pfeiffer, “Analysis and perspectives concerning CO_2 chemisorption on lithium ceramics using thermal analysis,” ournal of thermal analysis and calorimetry, vol. 108, no. 2, pp. 647–655, 2012, doi: 10.1007/ s10973-011-2063-y.
[126] W. N. R. Wan Isahak, Z. A. C. Ramli, M. W. Mohamed Hisham, and M. A. Yarmo, “Magnesium oxide nanoparticles on green activated carbon as efficient CO_2 adsorbent,” AIP Conf. Proc., vol. 1571, no. 1, pp. 882–889, 2013,2013. doi: 10.1063/1.4858766.
[127] Y. Duan and D. C. Sorescu, “CO_2 capture properties of alkaline earth metal oxides and hydroxides: A combined density functional theory and lattice phonon dynamics study,” J. Chem. Phys., vol. 133, no. 7, 2010, doi: 10.1063/1.3473043.
[128] X. Yang, “Magnesium Oxide-Based Absorbents for CO_2 Capture at Medium Temperature,” Current Pollution Reports, vol. 4, no. 1, pp. 13–22, 2018.
[129] Y. Duan, B. Zhang, D. C. Sorescu, and J. K. Johnson, “CO_2 capture properties of MCOH (M=Li, Na, K) systems: A combined density functional theory and lattice phonon dynamics study,” J. Solid State Chem., vol. 184, no. 2, pp. 304–311, 2011, doi: 10.1016/ j.jssc. 2010.12.005.
[130] Y. D. Ding, G. Song, X. Zhu, R. Chen, and Q. Liao, “Synthesizing MgO with a high specific surface for carbon dioxide adsorption,” RSC Adv., vol. 5, no. 39, pp. 30929–30935, 2015, doi: 10.1039/c4ra15127e.
[131] M. Bhagiyalakshmi, J. Y. Lee, and H. T. Jang, “Synthesis of mesoporous magnesium oxide: Its application to CO_2 chemisorption,” Int. J. Greenh. Gas Control, vol. 4, no. 1, pp. 51–56, 2010. doi: 10.1016/j.ijggc.2009.08.001.
[132] T. S. Marliza, M. A. Yarmo, A. Hakim, M. N. A. Tahari, M. W. M. Hisham, and Y. H. Taufiq-Yap, “CO_2 capture on NiO supported imidazolium-based ionic liquid,” AIP Conf. Proc., vol. 1838, no. 1, p. 020008, 2017, doi: 10.1063/1.4982180.
[133] I. Yanase, S. Konno, and H. Kobayashi, “Reversible CO_2capture by ZnO slurry leading to formation of fine ZnO particles,” Adv. Powder Technol., vol. 29, no. 5, pp. 1239–1245, 2018. doi: 10.1016/j.apt.2018.02.016.
[134] S. Kumar, “The effect of elevated pressure, temperature and particles morphology on the carbon dioxide capture using zinc oxide,” J. CO_2 Util., vol. 8, pp. 60–66, 2014, doi: 10.1016/j.jcou.2014.07.002.
[135] P. S. Pinto, G. D. Lanza, J. D. Ardisson, and R. M. Lago, “Controlled dehydration of $Fe(OH)_3$ to Fe_2O_3: Developing mesopores with complexing iron species for the adsorption of β-lactam antibiotics,” J. Braz. Chem. Soc., vol. 30, no. 2, pp. 310–317, 2019. doi: 10.21577/0103-5053.20180179.
[136] V. Chaudhary, Y. Zhong, H. Parmar, V. Sharma, X. Tan, and R. V. Ramanujan, “Mechanochemical Synthesis of Iron and Cobalt Magnetic Metal Nanoparticles and Iron/Calcium Oxide and Cobalt/Calcium Oxide Nanocomposites,” ChemistryOpen, vol. 7, no. 8, pp. 590–598, 2018, doi: 10.1002/open.201800091.
[137] K. Egizbek et al., “Application of Fe_2O_3/CeO_2 nanocomposites for the purification of aqueous media,” Appl. Phys. A Mater. Sci. Process., vol. 126, no. 6, pp. 1–12, 2020, doi: 10.1007/s00339-020-03665-5.

[138] S. Shivakumara, T. R. Penki, and N. Munichandraiah, “Synthesis and characterization of porous flowerlike Fe_2O nanostructures for supercapacitor application,” ECS Electrochem. Lett., vol. 2, no. 7, pp. 2013–2015, 2013, doi: 10.1149/2.002307eel.
[139] Z. Mirghiasi, F. Bakhtiari, E. Darezereshki, and E. Esmaeilzadeh, “Preparation and characterization of CaO nanoparticles from $Ca(OH)_2$ by direct thermal decomposition method,” J. Ind. Eng. Chem., vol. 20, no. 1, pp. 113–117, 2014, doi: 10.1016/ j.jiec. 2013.04.018.
[140] Y. Zhu, S. Wu, and X. Wang, “Nano CaO grain characteristics and growth model under calcination,” Chem. Eng. J., vol. 175, no. 1, pp. 512–518, 2011, doi: 10.1016/ j.cej. 2011.09.084.
[141] T. Nimmas et al., “Influence of CaO precursor on CO_2 capture performance and sorption-enhanced steam ethanol reforming,” Int. J. Hydrogen Energy, vol. 44, no. 37, pp. 20649–20662, 2019, doi: 10.1016/j.ijhydene.2018.07.095.
[142] D. Karami and N. Mahinpey, “Highly active CaO-based sorbents for CO_2 capture using the precipitation method: Preparation and characterization of the sorbent powder,” Ind. Eng. Chem. Res., vol. 51, no. 12, pp. 4567–4572, 2012. doi: 10.1021/ie2024257.
[143] J. Safaei-Ghomi, M. A. Ghasemzadeh, and M. Mehrabi, “Calcium oxide nanoparticles catalyzed one-step multicomponent synthesis of highly substituted pyridines in aqueous ethanol media,” Sci. Iran., vol. 20, no. 3, pp. 549–554, 2013, doi: 10.1016/j.scient. 2012.12.037.
[144] Criado, Y. A., Alonso, M., & Abanades, J. C. “Kinetics of the $CaO/Ca(OH)_2$ hydration/ dehydration reaction for thermochemical energy storage applications,” Industrial & Engineering Chemistry Research, vol. 53. no.32, pp-12594-12601, 2014. https://doi.org/ 10.1021/ ie404246p
[145] J. Yang, L. Ma, H. Liu, Y. Wei, B. Keomounlath, and Q. Dai, “Thermodynamics and kinetics analysis of Ca-looping for CO_2 capture: Application of carbide slag,” Fuel, vol. 242, pp. 1–11, 2019, doi: 10.1016/j.fuel.2019.01.018.
[146] A. Imtiaz, M. A. Farrukh, M. Khaleeq-Ur-Rahman, and R. Adnan, “Micelle-assisted synthesis of Almiddot;CaO nanocatalyst: Optical properties and their applications in photodegradation of 2,4,6-trinitrophenol,” Sci. World J., vol. 2013, ID 641420, p-11, 2013, doi: 10.1155/2013/641420.
[147] Khine, E. E., Bauml, P., & Kaptay, G. “Preparation of Calcium Oxide by A Precipitation Method” Materials Science and Engineering, vol. 45, no. 1, pp. 182–190, 2020. doi: 10.32974.mse.2020.018
[148] J. Wang et al., “Recent advances in solid sorbents for CO_2 capture and new development trends,” Energy Environ. Sci., vol. 7, no. 11, pp. 3478–3518, 2014, doi: 10.1039/ c4ee01647e.
[149] M. A. Alavi and A. Morsali, “Ultrasonic-assisted synthesis of $Ca(OH)_2$ and CaO nanostructures,” J. Exp. Nanosci., vol. 5, no. 2, pp. 93–105, 2010, doi: 10.1080 /17458080903305616.
[150] Z. Mirghiasi, F. Bakhtiari, E. Darezereshki, and E. Esmaeilzadeh, “Preparation and characterization of CaO nanoparticles from $Ca(OH)_2$ by direct thermal decomposition method,” J. Ind. Eng. Chem., vol. 20, no. 1, pp. 113–117, 2014, doi: 10.1016/ j.jiec.2013.04.018.
[151] A. Anantharaman and M. George, “Green Synthesis of Calcium Oxide Nanoparticles and Its Applications,” J. Eng. Res. Appl. , vol. 6, no. 10, pp. 27–31, 2016.
[152] P. Zhao et al., “Synthesis of Efficient CaO Sorbents for CO_2 Capture Using a Simple Organometallic Calcium-Based Carbon Template Route,” Energy and Fuels, vol. 30, no. 9, pp. 7543–7550, 2016, doi: 10.1021/acs.energyfuels.6b01223.

[153] H. Guo, S. Yan, Y. Zhao, X. Ma, and S. Wang, “Influence of water vapor on cyclic CO_2 capture performance in both carbonation and decarbonation stages for Ca-Al mixed oxide,” Chem. Eng. J., vol. 359, pp. 542–551, 2019, doi: 10.1016/j.cej.2018.11.173.
[154] H. J. Yoon and K. B. Lee, “Introduction of chemically bonded zirconium oxide in CaO-based high-temperature CO_2 sorbents for enhanced cyclic sorption,” Chem. Eng. J., vol. 355, pp. 850–857, 2019, doi: 10.1016/j.cej.2018.08.148.
[155] K. S. Lackner, “A guide to CO_2 sequestration,” Science (80), vol. 300, no. 5626, pp. 1677–1678, 2003, doi: 10.1126/science.1079033.
[156] R. Koirala, K. R. Gunugunuri, and P. Smirniotis, “Effect of zirconia doping on the structure and stability of CaO-based sorbents for CO_2 capture during extended operating cycles,” The Journal of Physical Chemistry C, vol. 115, no. 50, pp- 24804-24812,2011. doi.org/ 10.1021/jp207625c
[157] D. Kumar and A. Ali, “Nanocrystalline K-CaO for the transesterification of a variety of feedstocks: Structure, kinetics and catalytic properties,” Biomass and Bioenergy, vol. 46, pp. 459–468, 2012, doi: 10.1016/j.biombioe.2012.06.040.
[158] H. Lu, A. Khan, S. E. Pratsinis, P. G. Smirniotis, and C.- Zu, “Flame-Made Durable Doped-CaO Nanosorbents for CO_2 Capture,” Energy & Fuels, vol. 23, no. 2, pp- 1093-1100, 2009. doi.org/10.1021/ef8007882
[159] L. A. Fedunik-Hofman, A. Bayon, W. Lipinski, and S. W. Donne, “Investigation of novel hydroxyapatite-doped CaO material for calcination-carbonation thermochemical energy storage,” AIP Conf. Proc., vol. 2033, no. 1, p- 100004,2018, doi: 10.1063/ 1.5067125.
[160] C. H. Lee et al., “Na_2CO_3-doped CaO-based high-temperature CO_2 sorbent and its sorption kinetics,” Chem. Eng. J., vol. 352, pp. 103–109, 2018, doi: 10.1016/ j.cej.2018.06.141.
[161] D. Kumar, K. Abida, and A. Ali, “Aminolysis of Triglycerides using Nanocrystalline Nickel Doped CaO as an Efficient Solid Catalyst,” RSC Adv., vol. 6, no. 71, pp. 66822–66832, 2016, doi: 10.1039/c6ra12114d.
[162] S. Wang, S. Fan, L. Fan, Y. Zhao, and X. Ma, “Effect of cerium oxide doping on the performance of CaO-based sorbents during calcium looping cycles,” Environ. Sci. Technol., vol. 49, no. 8, pp. 5021–5027, 2015, doi: 10.1021/es5052843.
[163] A. N. Bezbaruah, S. Krajangpan, B. J. Chisholm, E. Khan, and J. J. Elorza Bermudez, “Entrapment of iron nanoparticles in calcium alginate beads for groundwater remediation applications,” J. Hazard. Mater., vol. 166, no. 2–3, pp. 1339–1343, 2009. doi: 10.1016/j.jhazmat.2008.12.054.
[164] P. Singh, S. K. Singh, J. Bajpai, A. K. Bajpai, and R. B. Shrivastava, “Iron crosslinked alginate as novel nanosorbents for removal of arsenic ions and bacteriological contamination from water,” J. Mater. Res. Technol., vol. 3, no. 3, pp. 195–202, 2014, doi: 10.1016/j.jmrt.2014.03.005.
[165] J. Trinkunaite-Felsen, A. Prichodko, M. Semasko, R. Skaudzius, A. Beganskiene, and A. Kareiva, “Synthesis and characterization of iron-doped/substituted calcium hydroxyapatite from seashells Macoma balthica (L.),” Adv. Powder Technol., vol. 26, no. 5, pp. 1287–1293, 2015, doi: 10.1016/j.apt.2015.07.002.
[166] S. Y. H. Wu, C. L. Tseng, and F. H. Lin, “A newly developed Fe-doped calcium sulfide nanoparticles with magnetic property for cancer hyperthermia,” J. Nanoparticle Res., vol. 12, no. 4, pp. 1173–1185, 2010, doi: 10.1007/s11051-009-9734-7.
[167] Qiu, Jin, et al. "Preparation and characterization of porous ultrafine Fe_2O_3 particles." Materials Research Bulletin, vol .40, no.11, pp -1968-1975, 2005. doi:10.1016/ j.materresbull.2005.05.025

[168] F. He, H. Wang, and Y. Dai, “Application of Fe_2O_3/ Al_2O_3 Composite Particles as Oxygen Carrier of Chemical Looping Combustion,” J. Nat. Gas Chem., vol. 16, no. 2, pp. 155–161, 2007, doi: 10.1016/S1003-9953(07)60041-3.
[169] P. Wang and I. M. C. Lo, “Synthesis of mesoporous magnetic γ-Fe_2O_3 and its application to Cr(VI) removal from contaminated water,” Water Res., vol. 43, no. 15, pp. 3727–3734, 2009, doi: 10.1016/j.watres.2009.05.041.
[170] S. W. Cao, Y. J. Zhu, M. Y. Ma, A. Li, and L. Zhang, “Hierarchically nanostructured magnetic hollow spheres of Fe_3O_4 and γ-Fe_2O_3: Preparation and potential application in drug delivery,” J. Phys. Chem. C, vol. 112, no. 6, pp. 1851–1856, 2008, doi: 10.1021/ jp077468.
[171] L. Di Felice, C. Courson, P. U. Foscolo, and A. Kiennemann, “Iron And Nickel Doped Alkaline-Earth Catalysts For Biomass Gasification With Simultaneous Tar Reformation And CO_2 Capture,” Int. J. Hydrogen Energy, vol. 36, no. 9, pp. 5296–5310, 2011, doi: 10.1016/ j.ijhydene.2011.02.008.
[172] S. Ghasemi-Kahrizsangi, A. Nemati, A. Shahraki, and M. Farooghi, “Densification and Properties of Fe2O3 Nanoparticles added CaO Refractories,” Ceram. Int., vol. 42, no. 10, pp. 12270–12275, 2016, doi: 10.1016/j.ceramint.2016.04.173.
[173] Mishra, Maneesha, and Doo-Man Chun. "α-Fe_2O_3 as a photocatalytic material: A review." Applied Catalysis A: General, vol. 498, pp-126-141,2015. doi.org/10.1016/ j.apcata.2015.03.023
[174] D. Ramimoghadam, S. Bagheri, and S. B. A. Hamid, “Progress in electrochemical synthesis of magnetic iron oxide nanoparticles,” J. Magn. Magn. Mater., vol. 368, pp. 207–229, 2014, doi: 10.1016/j.jmmm.2014.05.015.
[175] Y. H. Taufiq-Yap, S. Sivasangar, and A. Salmiaton, “Enhancement of hydrogen production by secondary metal oxide dopants on NiO/CaO material for catalytic gasification of empty palm fruit bunches,” Energy, vol. 47, no. 1, pp. 158–165, 2012, doi: 10.1016/ j.energy. 2012.09.026.
[176] L. Song and S. Zhang, “A simple mechanical mixing method for preparation of visible-light-sensitive NiO-CaO composite photocatalysts with high photocatalytic activity,” J. Hazard. Mater., vol. 174, no. 1–3, pp. 563–566, 2010. doi: 10.1016/j.jhazmat. 2009.09.088.
[177] A. Tang, X. Li, Z. Zhou, O. Jing, and H. Yang, “Mechanochemical synthesis of $Ni(OH)_2$ and the decomposition to NiO nanoparticles: Thermodynamic and optical spectra,” J. Alloys Compd., vol. 600, pp. 204–209, 2014. doi: 10.1016/j.jallcom.2014.02.120.
[178] L. A. Fedunik-Hofman, A. Bayon, W. Lipinski, and S. W. Donne, “Investigation of novel hydroxyapatite-doped CaO material for calcination-carbonation thermochemical energy storage,” AIP Conf. Proc., vol. 2033, 2018. doi: 10.1063/1.5067125.
[179] S. Lin, M. Harada, Y. Suzuki, and H. Hatano, “Hydrogen production from coal by separating carbon dioxide during gasification,” Fuel, vol. 81, no. 16, pp. 2079–2085, 2002. doi: 10.1016/S0016-2361(02)00187-4.
[180] J. Wang and E. J. Anthony, “On the decay behavior of the CO_2 absorption capacity of CaO-based sorbents,” Ind. Eng. Chem. Res., vol. 44, no. 3, pp. 627–629, 2005, doi: 10.1021/ ie0493154.
[181] D. P. Harrison, “Sorption-enhanced hydrogen production: A review,” Ind. Eng. Chem. Res., vol. 47, no. 17, pp. 6486–6501, 2008. doi: 10.1021/ie800298z.
[182] Y. Li, C. Zhao, H. Chen, L. Duan, and X. Chen, “CO_2 capture behavior of shell during calcination/carbonation cycles,” Chem. Eng. Technol., vol. 32, no. 8, pp. 1176–1182, 2009. doi: 10.1002/ceat.200900008.

[183] H. Gupta and L. S. Fan, “Carbonation-calcination cycle using high reactivity calcium oxide for carbon dioxide separation from flue gas,” Ind. Eng. Chem. Res., vol. 41, no. 16, pp. 4035–4042, 2002. doi: 10.1021/ie010867l.
[184] Y. Li, C. S. Zhao, C. Qu, L. Duan, Q. Li, and C. Liang, “CO_2 capture using CaO modified with ethanol/water solution during cyclic calcination/carbonation,” Chem. Eng. Technol., vol. 31, no. 2, pp. 237–244, 2008, doi: 10.1002/ceat.200700371.
[185] Y. Li, C. S. Zhao, H. Chen, and Y. Liu, “Enhancement of Ca-based sorbent multicyclic behavior in Ca looping process for CO_2 separation,” Chem. Eng. Technol., vol. 32, no. 4, pp. 548–555, 2009, doi: 10.1002/ceat.200800525.
[186] Y. Li, C. Zhao, H. Chen, L. Duan, and X. Chen, “Cyclic CO_2 capture behavior of $KMnO_4$-doped CaO-based sorbent,” Fuel, vol. 89, no. 3, pp. 642–649, 2010. doi: 10.1016/ j.fuel.2009.08.041.
[187] H. Lu, E. P. Reddy, and P. G. Smirniotis, “Calcium oxide based sorbents for capture of carbon dioxide at high temperatures,” Ind. Eng. Chem. Res., vol. 45, no. 11, pp. 3944–3949, 2006, doi: 10.1021/ie051325x.
[188] Y. Li, C. Zhao, H. Chen, C. Liang, L. Duan, and W. Zhou, “Modified CaO-based sorbent looping cycle for CO_2 mitigation,” Fuel, vol. 88, no. 4, pp. 697–704, 2009, doi: 10.1016/ j.fuel.2008.09.018.
[189] J. M. López, G. Grasa, and R. Murillo, “Evaluation of the effect of inert support on the carbonation reaction of synthetic CaO-based CO_2 sorbents,” Chem. Eng. J., vol. 350, no. May, pp. 559–572, 2018, doi: 10.1016/j.cej.2018.05.014.
[190] M. E. Diego, B. Arias, and J. C. Abanades, “Evolution of the CO_2 carrying capacity of CaO particles in a large calcium looping pilot plant,” Int. J. Greenh. Gas Control, vol. 62, pp. 69–75, 2017, doi: 10.1016/j.ijggc.2017.04.005.
[191] J. Cai, S. Wang, and C. Kuang, “Modeling of carbonation reaction for CaO-based limestone with CO_2 in multitudinous calcination-carbonation cycles,” Int. J. Hydrogen Energy, vol. 42, no. 31, pp. 19744–19754, 2017. doi: 10.1016/j.ijhydene.2017.06.173.
[192] W. Liu et al., “Structural evolution in synthetic, Ca-based sorbents for carbon capture,” Chem. Eng. Sci., vol. 139, pp. 15–26, 2016. doi: 10.1016/j.ces.2015.09.016.
[193] G. S. Grasa and J. C. Abanades, “CO_2 capture capacity of CaO in long series of carbonation/calcination cycles,” Ind. Eng. Chem. Res., vol. 45, no. 26, pp. 8846–8851, 2006. doi: 10.1021/ie0606946.
[194] S. E. B. Edwards and V. Materić, “Calcium looping in solar power generation plants,” Sol. Energy, vol. 86, no. 9, pp. 2494–2503, 2012. doi: 10.1016/j.solener.2012.05.019.
[195] Li, Zhen-shan, et al. "Synthesis, experimental studies, and analysis of a new calcium-based carbon dioxide absorbent." Energy & Fuels, vol.19, no.4, pp-1447-1452,2005. doi.org/10.1021/ef0496799
[196] C. M. Krohn and C. G. Krohn, “Development of porous solid reactant for thermal-energy storage and temperature upgrade using carbonation/decarbonation reaction,” Appl. Energy, vol. 69, no. 3, pp. 225–238, 2001. doi: 10.1016/S0306-2619(00)00072-6.
[197] A. M. Kierzkowska, R. Pacciani, and C. R. Müller, “CaO-based CO_2 sorbents: From fundamentals to the development of new, highly effective materials,” Chem Sus Chem, vol. 6, no. 7, pp. 1130–1148, 2013. doi: 10.1002/cssc.201300178.
[198] M. Zhao et al., “Durability of CaO-$CaZrO_3$ sorbents for high-temperature CO_2 capture prepared by a wet chemical method,” Energy and Fuels, vol. 28, no. 2, pp. 1275–1283, 2014. doi: 10.1021/ef4020845.
[199] M. Broda and C. R. Müller, “Synthesis of highly efficient, Ca-based, Al_2O_3-stabilized, carbon gel-templated CO_2 sorbents,” Adv. Mater., vol. 24, no. 22, pp. 3059–3064, 2012. doi: 10.1002/adma.201104787.

[200] M. Zhang, Y. Peng, Y. Sun, P. Li, and J. Yu, “Preparation of CaO-Al_2O_3 sorbent and CO_2 capture performance at high temperature,” Fuel, vol. 111, pp. 636–642, 2013. doi: 10.1016/j.fuel.2013.03.078.
[201] C. Luo, Y. Zheng, N. Ding, Q. Wu, G. Bian, and C. Zheng, “Development and performance of CaO/La_2O_3 sorbents during calcium looping cycles for CO_2 capture,” Ind. Eng. Chem. Res., vol. 49, no. 22, pp. 11778–11784, 2010. doi: 10.1021/ie1012745.
[202] R. Filitz, A. M. Kierzkowska, M. Broda, and C. R. Müller, “Highly efficient CO_2 sorbents: Development of synthetic, calcium-rich dolomites,” Environ. Sci. Technol., vol. 46, no. 1, pp. 559–565, 2012. doi: 10.1021/es2034697.
[203] X. Zhang, Z. Li, Y. Peng, W. Su, X. Sun, and J. Li, “Investigation on a novel CaO-Y_2O_3 sorbent for efficient CO_2 mitigation,” Chem. Eng. J., vol. 243, pp. 297–304, 2014. doi: 10.1016/j.cej.2014.01.017.
[204] R. Koirala, G. K. Reddy, J. Y. Lee, and P. G. Smirniotis, “Influence of Foreign Metal Dopants on the Durability and Performance of Zr/Ca Sorbents during High Temperature CO_2 Capture,” Sep. Sci. Technol., vol. 49, no. 1, pp. 47–54, 2014. doi: 10.1080/ 01496395.2013.836672.
[205] H. Lu and P. G. Smirniotis, “Calcium oxide doped sorbents for CO_2 uptake in the presence of SO_2 at high temperatures,” Ind. Eng. Chem. Res., vol. 48, no. 11, pp. 5454–5459, 2009. doi: 10.1021/ie900162k.
[206] E. David R. Lide, “CRC Handbook of Chemistry and Physics,” Second edi. CRC Press, Boca Raton, FL, 2005. doi: 10.1201/b17118-9.
[207] I. Barin, "ThermochemicalDataofPureSubstances." Second edi. Weinheim, New York: VCH Weinheim, VCH, New York, 1993.
[208] Bhandage, G. T., Tareen, J. A., & Basavalingu, B. , “Retrieval of thermodynamic properties of $M(OH)_2$ (M= Mn, Ni and Cd) phases from hydrothermal phase equilibria of MO-H_2O systems,” Journal of thermal analysis, vol.32, no. 6, pp. 1823-1831, 1987.
[209] Zotov, A. V., Shikina, N. D., & Akinfiev, N. N., “Thermodynamic properties of the Sb (III) hydroxide complex $Sb(OH)_3(aq)$ at hydrothermal conditions,” Geochimica et Cosmochimica Acta, vol. 67, no. 10, pp. 1821-1836, 2003.
[210] Barbara L, <icheal O, Han W, <Mikazu Y,”Thermodynamic Date for Spceciation and Solubility of Pd, Pb, Sn, Sb, Nb and Bi in Aqueous solution,” Japan Nuclear Cycle Dvelopment Insitude, JNC TN 8400, pp 99-011, 1999.
[211] Dean, John A. , “Lange’s Handbook of Chemistry,” 12th ed.; McGraw-Hill: New York, New York, p 94994, 1979.
[212] Bogdan S.V, Gheorghe .D, et. al “Thermal Activated $Al(OH)_3$-Effect of Different Thermal Treatments,” Ind. Text., vol. 1273, no. 2, pp. 55–58, 1996. doi: 10.1201/ 9781498710466-7.
[213] A. Savel’eva, T. Bugrova, A. Petrov, V. Dutov, and G. Mamontov, “Thermally-Activated $Al(OH)_3$: Phase transformations and porosity,” Key Eng. Mater., vol. 670, pp. 133–138, 2015, doi: 10.4028/www.scientific.net/KEM.670.133.
[214] H. Zhang et al., “Solvent-free hydrothermal synthesis of gamma-aluminum oxide nanoparticles with selective adsorption of Congo red,” J. Colloid Interface Sci., vol. 536, pp. 180–188, 2019, doi: 10.1016/j.jcis.2018.10.054.
[215] J. A. Morales, “Synthesis of Hematite α-Fe_2O_3 Nano Powders by the precipitaiton method,” Cienc. en Desarro., vol. 8, no. 1, pp. 99–107, 2017, doi: ISSN 0121-7488 –.
[216] S. P. Jiang, W. R. Ashton, and A. C. C. Tseung, “An observation of homogeneous and heterogeneous catalysis processes in the decomposition of H_2O_2 over MnO_2 and $Mn(OH)_2$,” J. Catal., vol. 131, no. 1, pp. 88–93, 1991. doi: 10.1016/0021-9517(91) 90325-X.

[217] R. S. Sahib and J. A. Naser, "Preparation , Characterization and Surface Area Properties of Manganese Oxide Nanoparticles," Ann. R.S.C.B, vol. 25, no. 5, pp. 2962–2969, 2021.
[218] Y. Oaki and H. Imai, "One-pot synthesis of manganese oxide nanosheets in aqueous solution: Chelation-mediated parallel control of reaction and morphology," Angew. Chemie - Int. Ed., vol. 46, no. 26, pp. 4951–4955, 2007, doi: 10.1002/anie.200700244.
[219] A. V. Zotov, N. D. Shikina, and N. N. Akinfiev, "Thermodynamic properties of the Sb(III) hydroxide complex $Sb(OH)_{3(aq)}$ at hydrothermal conditions," Geochim. Cosmochim. Acta, vol. 67, no. 10, pp. 1821–1836, 2003, doi: 10.1016/S0016-7037(00)01281-4.

Publications related to this research work

Journal papers

1. E. E. Khine et al., "Preparation of calcium oxide by a precipitation method," Material Science and Engineering, vol. 45, no. 1, pp. 182–190, 2020. DOI: 10.32974.mse.2020.018

2. E. E. Khine et al., "Synthesis and characterization of calcium oxide nanoparticles for CO_2 capture," J. Nanoparticle Res., vol. 24, no. 7, 2022, doi: 10.1007/s11051-022-05518-z. (Q2)

Proceeding papers

1. E. E. Khine et al., "Synthesis of new Fe_2O_3 doped CaO nanoparticles via precipitation method and their characterizations". Proceeding of the 1st International Congress on Modern Sciences Tashkent Chemical-Technologies Institute conference, May10-11,2022, Uzbekistan, ISBN: 978-625-7464-90-1.

2. E. E. Khine et al., "Pure CaO and Fe_2O_3 nanoparticles calcined under vacuum: preparations and characterizations". Proceedings of 6th International Asian Congress on Contemporary Science VI Conference, May27-29, 2022, Van, Turkey.

Oral and Poster Presentation

1. Ei Ei Khine, "Preparation and applications of CaO nanoparticles", conference for PhD students, oral presentation, Miskolc, Hungary,22.11.2018.

2. Ei Ei Khine, "Preparation of Calcium Oxide nanoparticles through thermal decomposition method", 18th Austria Chemistry Day conference, poster presentation, Linz, Austria, 24-27,09.2019.

3. Ei Ei Khine, "Preparation of Calcium Oxide nanoparticles by using precipitation method", 7th International Scientific Conference On Advances in Mechanical Engineering, oral presentation, Debrecen, Hungary, 7.10.2019.

4. Ei Ei Khine, "Synthesis and characterizations of Calcium Oxide nanoparticles", 13th DOSZ Spring Wind Conference, oral presentation, Budapest, Hungary, 7.10.2019.

5. Ei Ei Khine, “Preparation and characterizations of metal oxides doped CaO nanoparticles through precipitation method”, conference for PhD students, oral presentation, Miskolc, Hungary,8.11.2021.

6. Ei Ei Khine, “Preparation and characterizations of cobalt oxide doped CaO nanoparticles through precipitation method”, 9th Euroasia Congress on Scientific Research and Recent Trends Conference, oral presentation, Antalya, Turkey, 20.2.2022.

7. Ei Ei Khine, “Preparation and characterizations of Nickel Oxide doped CaO nanoparticles through precipitation method”, 4th Virtual Congress on Material Science and Engineering Conference, oral presentation, USA, 28.3.2022.

8. Ei Ei Khine, “Characterizations of Iron III Oxide doped Calcium Oxide nanoparticles by a precipitation method”, Latin American Scientific Research Conference, oral presentation, Columbia, 6.4.2022.

9. Ei Ei Khine, “Characterizations of metal oxide doped Calcium Oxide nanoparticles”, 8th International Conference on Innovative Scientific Research, oral presentation, Adana, Turkey, 17.4.2022.

10. Ei Ei Khine, “The metal oxides obtained through precipitation method”, 30th Anniversary of Baku Euroasia University, International Scientific Research Congress, oral presentation, Baku, Azerbijian, 30.4.2022.

11. Ei Ei Khine, “CoO doped CaO nanoparticles prepared under different reaction conditions”, 1st International Conference on Engineering and Applied Natural Sciences, oral presentation, Konya, Turkey, 10.5.2022.

12. Ei Ei Khine, “Synthesis of new Fe_2O_3 doped CaO nanoparticles via precipitation method and their characterizations”, TASHKENT 1st International Congress on Modern Science, oral presentation, Tashkent, Uzberkistan, 10.5.2022.

13. Ei Ei Khine, “Pure CaO and Fe_2O_3 nanoparticles calcined under vacuum: preparations and characterizations”, 6th International Asian Congress on Contemporary Science VI Conference, oral presentation, Van, Turkey,10-12.5.2022.